Cranfield UNIVERSITY

DINA ARZINA

VIBRATION ANALYSIS OF COMPRESSOR BLADE TIP-RUBBING

SCHOOL OF ENGINEERING

MSC BY RESEARCH

Cranfield UNIVERSITY

SCHOOL OF ENGINEERING

Crashworthiness, Impact & Structural Mechanics Group

MSC BY RESEARCH

Academic Year 2010 – 2011

DINA ARZINA

VIBRATION ANALYSIS OF COMPRESSOR BLADE TIP-RUBBING

PROJECT SUPERVISOR: DR. RADE VIGNJEVIC

Abstract

There has been a significant increase in air traffic volume, particularly over the past twenty years. In order to cope with this increase in demand, it has been necessary to increase the efficiency of aircraft engines. Over the years, this has been achieved by reducing the clearance between blade tips and the engine casing. As a consequence of the reduced clearance, tip-rubbing frequently occurs in the engine during operation.

The primary aim of this project is to address the vibrations involved in a tip-rubbing phenomenon when a blade of the Intermediate Pressure (IP) compressor in a Trent 900 engine interacts with the casing. Current trends towards blade optimisation tend to make the blade thinner and thus more flexible; therefore, it is very important to be able to successfully predict and prevent nonlinear response of a blade when tip-rubbing occurs. Current literature on the study of nonlinear vibration of a blade in a tip-rub event is limited; this project is understood to be the first to attempt an understanding of the issue.

In this thesis, analytical models are presented that predict the nonlinear responses of rotor-stator interactions. These are helpful in understanding nonlinear parameters that can have an effect on the system response. Simulations were started by determining the stresses in the blade due to centrifugal rotation. Resonant frequencies of the blade were determined by modal analysis. Finally, the tip-rubbing event was simulated. The results were used to output frequency response curves which were used to identify if the blades were behaving nonlinearly as a result of tip-rubbing.

The primary conclusion from this project is that tip-rubbing can excite nonlinear vibration in the compressor blades. However, the simulation results were affected adversely by hourglassing of the casing segments and should not be considered completely accurate.

Acknowledgements

First and foremost, I would like to thank my supervisor Dr. Rade Vignjevic and Dr. Tom de Vuyst for giving me this opportunity and subject of research. Without their support and encouragement, this thesis would not have been completed.

Thanks to my parents Muhammed Khairul Alam Bhuiyan and Rizia Khatoon for their countless sacrifices; their constant support and belief in me has made me who I am today. Also, a big heartfelt thank you goes to my siblings Ashraf, Jihan and Nabilah for supporting me with patience and understanding.

Thanks also to my friends at Cranfield University for making this year a memorable and enjoyable one.

Last but not least, I would like to express my sincerest gratitude to the Almighty, without Whom nothing is possible.

Contents

List of Figures

List of Tables

Glossary

Modal analysis – Technique used to determine natural frequencies and mode shapes of a structure under free vibration.

Shear locking – Overly stiff response of fully-integrated solid elements in finite element analysis. This occurs only in fully-integrated elements and is mostly triggered by elements with poor aspect ratios.

Aspect Ratio – Ratio of one spatial dimension to another. Elements are said to have poor aspect rations when one of the spatial dimensions is substantially larger than another e.g. $x \gg y$.

Hourglassing – Zero energy modes of deformation that produce zero strain and no stress. Hourglass modes occur only in under-integrated elements.

Blade Pass Frequency (BPF) – A potential vibration frequency on bladed turbomachinery. It is calculated as the number of fan blades times shaft rotating frequency.

Nomenclature

θ, ϕ	Angle
ω_0, ω_n	Natural frequency
g	Acceleration due to gravity
l	Length
t	Time
W_d	Energy dissipated due to viscous damping
c	Damping
m	Mass
x, y	Linear displacement
α	Angular acceleration
C_{eq}	Equivalent viscous damping
ζ	Damping ratio
k	Stiffness
E	Young's modulus of elasticity
I	Moment of inertia
α_i	Constant of the i^{th} mode of vibration of a cantilever beam
k_s	Stiffness of rotating shaft
k_b	Stiffness of rotor-stator contact
e	Rotor eccentricity
r_0	Clearance between rotor and stator
σ_0	Static yield stress
ε_0	Static yield strain
C, p	Experimentally-determined Cowper-Symonds parameters
$\dot{\varepsilon}$	Uniaxial strain rate
σ_{scaled}	Yield strength scaled by Cowper-Symonds model
E_{tan}	Gradient of bilinear stress-strain curve
σ_{fail}	Stress at failure
ε_{fail}	Strain at failure

ν	Poisson's ratio
ρ	Density
F	Centrifugal force
ω	Angular velocity
r	Radial distance
cv_{tol}	Convergence tolerance for dynamic relaxation
γ	Shear stress
μ_c	Frictional coefficient of contact
μ_s	Static coefficient of friction
μ_d	Dynamic coefficient of friction
v_{rel}	Relative velocity of surfaces in contact
k_c	Segment-based contact stiffness between blade and casing
Δt_c	Timestep size
G	Modulus of rigidity
l_e	Effective length

Chapter 1 – Introduction

1.1 Blade Tip-Rubbing Events

There has been a significant increase in air traffic volume, particularly over the past twenty years. In order to cope with the increase in demand, it has been necessary to increase the efficiency of aircraft engines. Over the years, this has been achieved by increasing the operating temperatures, making the aircraft more aerodynamic, utilising lightweight materials in construction of the aircraft, and by reducing the clearance between blade tips and the engine casing. As a consequence of the reduced clearance, tip-rubbing frequently occurs in the engine under normal operating conditions.

Tip-rubbing can also occur due to factors such as a fan blade-off event (FBO) where a blade gets detached from the shaft during engine operation, different thermal expansion rates of the rotor and the casing which can be due to the different amounts of material used in the rotor and the casing, or centrifugal forces acting on the blades; this reduces the already tight clearances and it is not uncommon for the blade to the rub against the casing in such a case.

Another reason for tip-rubbing is deformation of the casing due to heavy landing. This is the configuration which will be analysed in this project since Rolls-Royce are primarily interested in the tip-rubbing events due to casing deformation as a result of heavy landing. During the short time of a heavy landing, the force transmitted from the aircraft landing gear and tyres produce a deceleration on the aircraft. The resulting inertial forces applied to the engine casing causes distortion from an initial circular shape to an elliptical shape (Fig. 1.1). If the distortion is high enough during this short period, it is possible for the compressor blade tips to contact the casing, leading to complex vibration of the blades.

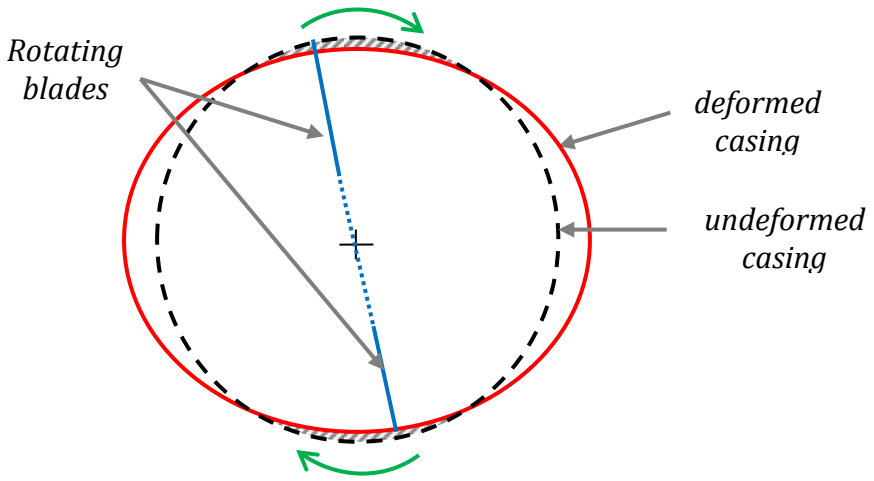

Fig. 1.1 – Distortion of casing due to heavy landing; shaded areas indicate regions where blade-casing interaction is likely to occur

Because of the high velocity of the compressor, a tip-rubbing event involves transformation of high amount of kinetic energy into other forms such as deformation energy and thermal energy. Consequently, the forces involved during such an event can be quite high and potentially cause severe damage. However, due to the extremely short duration during which tip-rubbing occurs, determination of the dynamics of the system has been a real challenge so far.

During engine operation, the rotor and the casing can experience three types of loading which have an effect on the blade tip clearances:

(i) Expansion in blade geometry as a result of centrifugal forces caused by changes in speed and pressure. This is usually greater for the rotor than for the casing.

(ii) Expansion of casing due to increase in temperature – this is usually lower than thermal expansion experienced by the rotor.

(iii) Expansion of blade due to increase in temperature – this experiences the fastest thermal expansion.

If blade tip-rubbing forces are too high, the blades can fracture, travelling downstream and fracturing the next set of blades, and so on. This total annihilation of blades is called blade de-cobbing and is very undesirable. Rubbing of rotating

blade tips against the stationary outer case is a highly nonlinear impact event. There are two distinct ways in which the event and its effects can be envisioned, namely:

(i) the determination of the global vibrations of the rotor-casing system, and

(ii) the nature of the local casing-rotor interactions.

This project will be looking at the second case, with particular focus given to nonlinearities as a result of the tip-rubbing event.

1.1.1 Time and Cost of Tip-Rubbing Events to Industry

Tip-rubbing has long been identified as a significant contributor to excessive maintenance and in general to engine failure. The contact event results in complicated vibration events within the engine. Tip-rubbing also leads to reduced engine performance, and reduces the lives of the blade and the casing. Repeated or extensive contact may lead to premature cracking in the blade tips which require suitable repair or replacement of the blades.

Between 1962 and 1975, 10.2% of 275 reported jet engine failures were attributed to rub-related phenomena [19]. The National Transportation Safety Board (NTSB) records a case in 1973 where one of the engine fan assemblies disintegrated during flight due to interaction between the fan blade tips and the fan casing (Fig. 1.2). The tip-rub condition was caused by the acceleration of the engine to an abnormally high fan speed which initiated a multiwave, nonlinear vibratory response within the fan section of the engine.

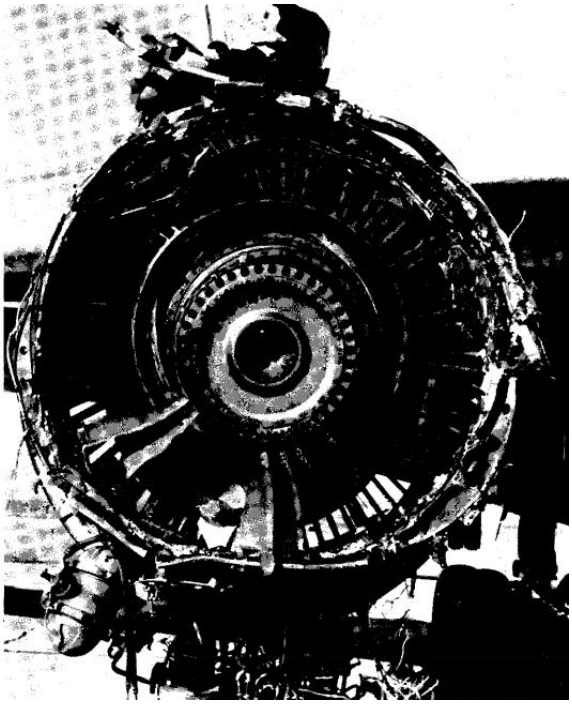

Fig. 1.2 – Catastrophic damage of engine due to tip-rubbing [2]

Another tip-rubbing event documented by the NTSB in 1993 involved dynamic multi-axis loading on the engine due to extreme turbulence [3]. This generated forces on the engine pylon which exceeded the ultimate lateral load-carrying capability of the pylon.

The Australian Transport Safety Bureau (ATSB) records an in-flight failure of a Rolls-Royce RB211-524G2-T on a Boeing 747-438 [9]. Investigation of the failed engine showed that tip-rubbing had occurred in the high pressure compressor (HPC) due to distortion of the casing. This resulted in stress cracking at the blade root which led to an FBO event. The release of the blade resulted in severe damage to the HPC section, causing massive vibration within the engine and necessitating an emergency shutdown. Tip-rubbing events between compressor blades and casing have previously been encountered in Rolls-Royce Trent 500 on Airbus A340-600 [7]. These issues have been sorted out in-service.

These are a few examples which highlight the catastrophic consequences of tip-rubbing events on engines, and the consequent high costs associated. Therefore, it is extremely important to have a proper understanding of this event.

Analytical techniques and finite element methods have frequently been used in the past to improve understanding of this problem. However, most methods to date have simplified the event by using a linear approximation. Research into the nonlinear vibratory response and amplitude growth due to the tip-rubbing event is limited.

1.1.2 Minimising Tip-Rubbing Events by Depletion of Abradable Layer

Although considerable effort has been made to understand the dynamics involved in a tip-rubbing event, the amount of success is limited as it is a difficult phenomenon to understand. One reason behind this might be that actual contact between the blade and the casing seldom occurs. Most modern turbofan engines contain a layer of abradable material lining the inner wall of the casing which prevents the blade tip from impacting against the casing in a blade tip-rubbing event. The purpose of the abradable layer is to absorb the kinetic energy from the blade by breaking up into fine debris. Because the debris particles are so small, they do not cause any damage to the engine.

The erosion of the abradable layer minimises the damage to the casing and the blade, consequently preventing damage to the engine in the long run. The abradable material needs to be replaced regularly. Coating, films, and combined use of both metals and ceramics play a major role in maintaining interference clearance in turbomachinery sealing and component life. Patents of abradable materials have been developed over the years which are made to minimise the damage to the system from a tip-rubbing event. Recent technology has developed abradable materials which are designed to withstand the different temperatures throughout the jet engine (Fig. 1.3).

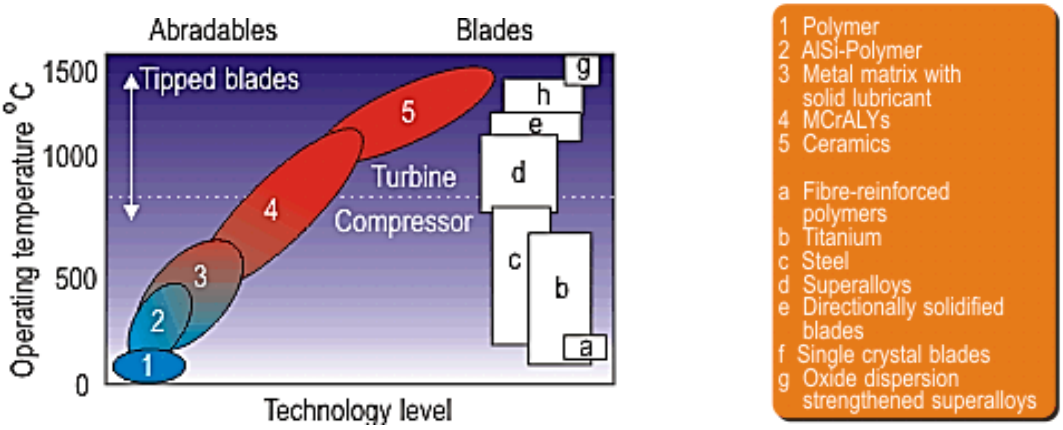

Fig. 1.3 – Different abradable coatings used for a typical turbofan engine [14]

1.2 The Rolls-Royce Trent 900

The engine of concern for this project is the Rolls-Royce Trent 900 (Fig. 1.4). In this section, a brief overview of the engine is given. The Trent 900 is the fourth member of the RB211 engines developed by Rolls-Royce that are currently being used on the Airbus A380.

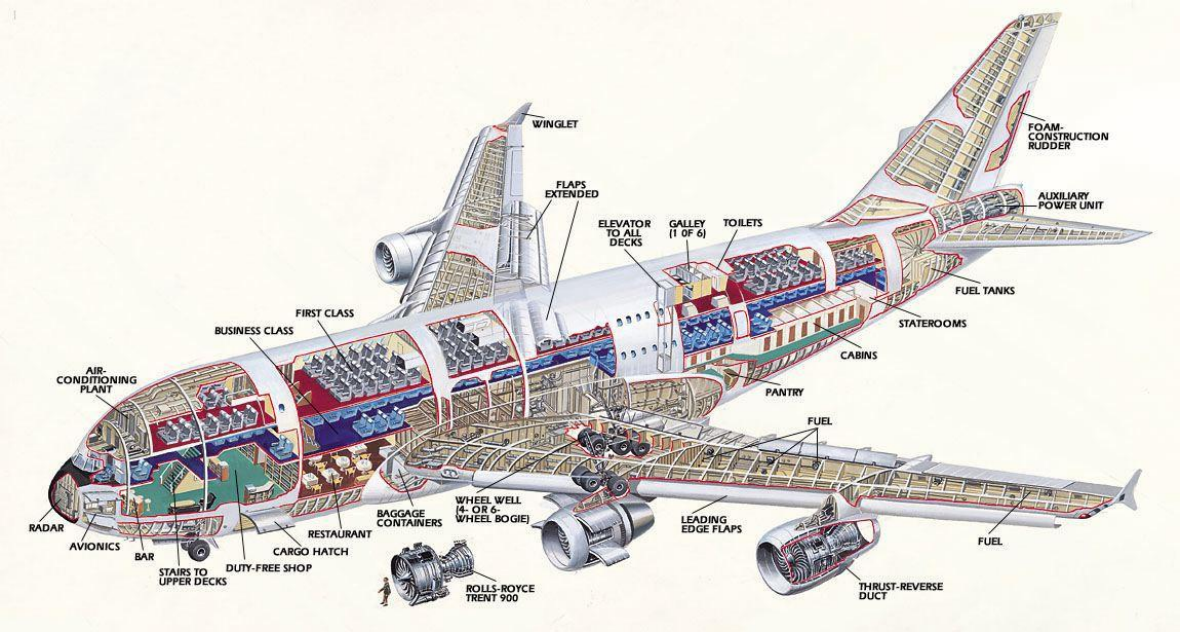

(a)

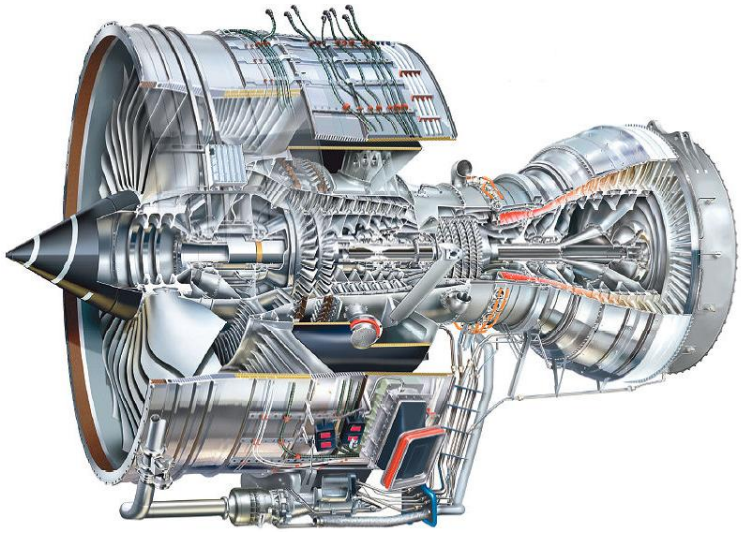

(b)

Fig. 1.4 – Rolls-Royce Trent 900; (a) On an Airbus A380 [12] (b) Cutaway view [25]

It is a three-shaft high bypass ratio turbofan engine, weighing around 6,436 kg [25]. In the three-shaft design the intermediate compressor is mounted separately and can rotate faster. Fewer compressor stages are therefore required, improving efficiency and reducing cost and engine length. This increases engine stiffness and reduces weight.

1.2.1 The Second-Stage Compressor and Casing

The compression system of a Trent 900 engine comprises the fan, eight intermediate pressure stages and six high pressure stages. The focus of this project is on the Intermediate Pressure (IP) compressor stage (Fig. 1.5). The primary purpose of the compressor is to increase the pressure of the air through the gas turbine core. The compressed air is then delivered to the combustion system.

The compressor discs are machined by turning and milling processes [24]. Inertia friction welding is frequently used to manufacture the disc and the drum while high-speed grinding processes are used to create the grooves in the disc for the blades. The compressor blade is manufactured by precision hot forging of an extruded billet, followed by machining the root features. In order to increase aerodynamic efficiency, the blade surface is polished to a smooth finish.

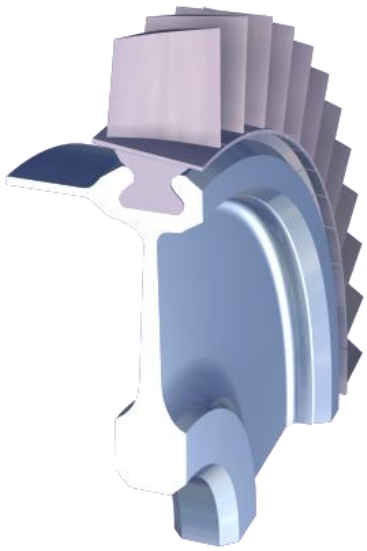

Fig. 1.5 – IP compressor disc and blades [32]

The Trent 900 compressor blades are made out of titanium Ti-6Al-4v. This is a very common titanium alloy used in the aerospace industry due to its low density, high strength, resistance to corrosion and ability to withstand operating temperatures in the range of 400˚C as seen in the IP compressor region (Fig. 1.6).

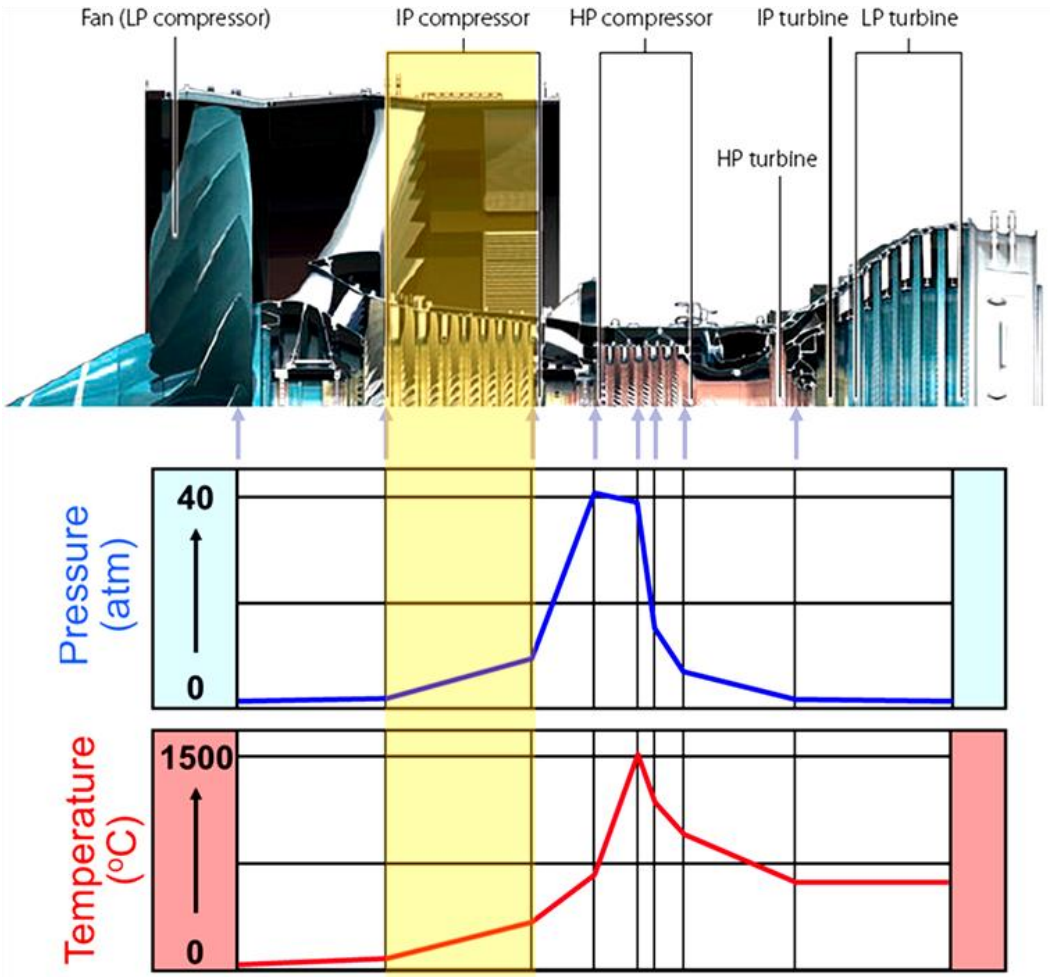

Fig. 1.6 – Temperature and pressure distribution in Trent 900; IP compressor stage highlighted [32]

The compressor blade is normally fitted to the disc using root fixing methods [24]. The main drawback of this method is the added mass to the blade, which increases centrifugal forces applied to the disc. The blades in the IP compressor are fixed to the disc using axial fixing, where grooves are machined onto the disc which allow placement of fir-tree or dovetail blade roots. Although axial fixings are expensive, they are generally more robust.

The compressor casing is used to secure the stator vanes. One of the design requirements is that the casing should be constructed from materials that closely match the thermal and centrifugal growth properties of the rotor to achieve

acceptable tip clearance under both steady state and transient conditions. Like the blade, the casing is also manufactured from titanium [12]. This further reduces the weight and size of the engine.

Ti-6Al-4v generally has poor surface wear properties and tends to seize when in sliding contact. This can be improved by applying various surface treatments to the interacting components. Although Rolls-Royce researched the development of fire-resistant titanium alloys to be used in compressor casings [24], it is unclear if this technology has been applied to the Trent 900. However, the importance of minimising tip to casing interactions cannot be overemphasised.

1.3 Primary Aims and Objectives

There is a vast amount of literature on the tip-rubbing phenomenon. However, current literature on nonlinear vibration of blade tip-rubbing is fairly limited.

The primary aim of this project is to gain an understanding of nonlinear vibration induced in the blade when the tip of one of the second-stage compressor blades of the Rolls-Royce Trent 900 comes into contact with the casing during operation.

The key objective will be to evaluate if tip-rubbing induces nonlinear vibrations in the blade. This can form the baseline model for further research into this topic.

1.4 Structure of Thesis

The thesis is structured as follows:

Chapter 1 – A brief introduction to the tip-rubbing event and related costs to industry, and how abradable materials are used to minimise the occurrence of tip-rubbing are mentioned. The Rolls-Royce Trent 900 engine and the second stage compressor section are described briefly. Aims and objectives of the project are also defined in this chapter.

Chapter 2 – Review of current literature on general rotor-stator interaction. The discussion then focus on literature on tip-rubbing events, and current research into nonlinearities involved during a tip-rubbing event.

Chapter 3 – This chapter contains analytical models of nonlinear rotor-stator interaction. Types of nonlinearities are also discussed.

Chapter 4 – This chapter discusses the software and techniques used for modelling the tip-rubbing event. Methodology for how the proposed aims and objectives will be met is also presented. The chapter also talks about modifications made to the blade-disc geometry.

Chapter 5 – Finite element analysis of stress initialisation on the model due to rotation is presented in this chapter. The results from this simulation are used as input for the prestressed modal analysis.

Chapter 6 – Modal analysis of the compressor blade is discussed in this chapter. A comparative study between the resonant frequencies of the unstressed and prestressed blade is outlined. This helps to gain an understanding of the possible modes that could be excited during tip-rubbing. A study into the effect of different element formulations is also presented.

Chapter 7 – Finite element modelling and analysis of the tip-rubbing event using a two-blade model is discussed. Frequency-amplitude plots from this analysis are used to identify if the blades are behaving linearly or nonlinearly. Discussion of results obtained and their implications are presented in this chapter.

Chapter 8 – Recommendations for future work which would help in further understanding and better modelling of the nonlinear dynamics involved in a tip-rubbing event are outlined in this concluding chapter.

Chapter 2 – Literature Review

In order to identify the primary aims and objectives of this project, it is imperative that a critical literature review be carried out. A summary of the current literature on the tip-rubbing phenomenon is also presented; this paves the way for further discussion of recent research that focus on nonlinear dynamics of a tip-rubbing event. The primary aim of this chapter will be to gain an understanding of literature which have contributed to an understanding of tip-rubbing.

2.1 Dynamics and Stability of Blade-Casing Interactions

When the compressor blade tip contacts with the nacelle, part of the high kinetic energy of the blade is transformed into other forms such as plastic deformation energy of blade and nacelle, and thermal energy due to friction between the two contacting surfaces; the contact event also causes a reduction in flexibility of the blade. This is a highly nonlinear event which results in complicated vibration events in the engine.

Existing literature on the tip-rubbing phenomenon has primarily focused on two aspects; namely, the localised interaction between blade and casing, and the global vibration of the rotor-casing as a result of tip-rubbing. Rubbing occurs in different ways based on such factors as the operating conditions and design parameters. Generally, the phenomenon of rubbing can be classified into two types:

(i) Partial rub – the blade interacts with part of the casing, and
(ii) Full annular rub – continuous interaction between blade and casing for one revolution.

The occurrence of tip-rubbing has been widely studied by many researchers; in particular, there is a vast amount of literature on linear dynamics of vibrating systems. However, nonlinear behaviour is not very well understood and difficult to

apply to systems. An understanding of nonlinear behaviour is essential since it is more universal and realistic.

In order to understand the dynamics of the tip rubbing event, the blade can initially be thought of as a cantilever beam subjected to an excitation force at the free end. If the displacement amplitude is sufficiently small and allowed to damp out before the next tip rubbing event, the dynamics of the system can be investigated as a linear problem. However, if the amplitude of vibration is large or if the excitation force applied feeds into the growth of the amplitude (possibly due to high excitation forcing frequency which does not allow sufficient time for the vibration to damp out), the dynamics are now better approximated as nonlinear behaviour.

Nonlinear vibration is a common occurrence in structures. This can sometimes have quite damaging effects on the dynamic behaviour of systems. In the aeronautical industry, more often than not, a system subjected to nonlinear vibration can be a threat to human life since nonlinear vibration of a system can have serious effects on the fatigue life of an engine. According to [28], the implications of nonlinear vibration on blade fatigue life could be quite serious. There is currently major concern in the aerospace industry regarding the possibility of large amplitude coherent nonlinear motions.

2.2 Review of Current Literature on Rotor-Stator Interactions

There has been a lot of research done on rotor-to-stator interactions; for a list of key research articles which have addressed this issue, the reader should refer to [30]. Although research into tip-rubbing phenomenon has taken place since the advent of jet engines, an expanded understanding of the subject was not fully explored until the 1980s. Primarily, analytical, numerical and experimental methods have been used to understand the dynamics involved. Turner *et. al* [27] state in their paper that early investigation primarily focused on the rotor dynamic response; less attention was paid to the blade and casing dynamics. This trend in

research was changed by Muszynska [22] who, in his literature review on rub-related vibrations, considered the local blade and casing dynamics as well.

After Muszynska's survey, there has been little experimental work in the field. Dai *et al.* [11] conducted analytical studies on the tip-rubbing phenomenon; experimental and analytical studies on the dynamics of full annular rub were conducted by Yu *et al.* [29] and Muszynska [22]. Isaksson [18] also studied the phenomena analytically.

According to Aidanpää and Lindkvist [8] the jump phenomenon is expected to occur during a full annular rub. The authors also discovered that jump phenomena tend to occur at frequencies above the system natural frequency. It can be brought on by the nonlinearities present within the system. Chu and Lu [10] discovered that rotor-stator rub increased the stiffness of the rotor, which can effectively reflect upon the severity of the event. The change in the trend of rotor stiffness can be used to evaluate the severity of the rub.

Most of the studies conducted on the tip-rubbing phenomenon simplify the analysis by taking a rotating cantilever beam as the baseline model. However, Aidanpää and Lindkvist [8] discovered that the dynamics of a real blade are quite different to a simplified model. The authors also discovered that analytical models produce quite different results to FEA models. This further reiterates the necessity of modelling tip-rubbing on FEA model of a real blade.

There are a few projects which have attempted an understanding of the nonlinear dynamics involved in a tip-rubbing event. Turner [27] mentions two projects in the Ohio State University; the first is a thesis written by Garza in which a full transient and nonlinear rub simulation of a blade is conducted using LS-DYNA. Also, Turner [27] published a thesis which describes the development of a simulation technique for predicting rub-induced blade dynamics. However, access to both of the theses is limited and therefore it has not been possible to gain knowledge of their results.

Another project conducted by Aidanpää and Lindkvist [8] consists of finite element analysis of a full annular rub between a turbine blade and the casing. In their report, the authors acknowledge that due to the complexity of the finite element models studied, they were only able to look at short durations of the tip-rubbing event and the effect of the dynamics on the system parameters were largely unknown.

From the literature review conducted in the preceding paragraphs, it can be seen that there is a need in current literature to understand nonlinearities involved in blade tip-rubbing.

Chapter 3 – Analytical Models of Rotor-Stator Interaction

In this chapter, analytical models of rotor-stator interaction are described. A review of nonlinearities present in mechanical systems and analytical derivation of amplitude jumps during resonance is also presented. The purpose of this chapter is to provide an insight into various factors which can give rise to nonlinear vibrations, and how they can be modelled analytically.

3.1 Nonlinearities in Structure Dynamics

Oscillatory systems can be distinguished as either linear or nonlinear. A system is said to be linear when the principle of superposition holds true; that is, when the system is additive. The principle of superposition states that whenever two or more waves meet, the instantaneous total displacement at any point is equal to the vector sum of the individual displacements at that point. This principle is a distinct characteristic of linear systems only, and hence is considered as a definition of linear systems.

Strictly speaking, all oscillatory systems are inherently nonlinear. Linear systems are actually a localised linear representation of a nonlinear system and can only approximate the nonlinear behaviour which occurs in most real systems. In some cases, linear approximation is acceptable; however, linear assumptions often vary significantly from reality and can provide misleading information.

Nonlinear systems display behaviour that are different from linear systems such as response at frequencies other than excitation frequencies, multiple steady-state solutions, jump phenomena, internal resonances and chaos. Nonlinear dynamics are more difficult to analyse due to the fact that the principle of superposition does not apply to nonlinear systems. This means that the system

response to any combination of dynamic loads, simultaneously applied, does not equal the sum of the individual responses to each of the loads acting separately.

Therefore, concepts which are purely linear cannot be directly applied to nonlinear systems. Examples of nonlinear systems are described in the following sections.

3.1.1 Geometric Nonlinearity

This type of nonlinearity is caused by large amplitudes of vibration; the following example gives an idea of geometric nonlinearity in an oscillating pendulum.

One of the simplest nonlinear oscillating systems is the simple pendulum. Consider a single degree-of-freedom harmonic oscillator excited by restoring elastic force (Fig. 3.1); the differential equation modelling the free undamped simple pendulum can be mathematically written as

$$\frac{d^2\theta}{dt^2} + {\omega_0}^2 \sin\theta = 0 \tag{3.1}$$

where θ is the angular displacement, t is the time and $\omega_0$is the natural frequency of the pendulum which is calculated as

$$\omega_0 = \sqrt{\frac{g}{l}} \tag{3.2}$$

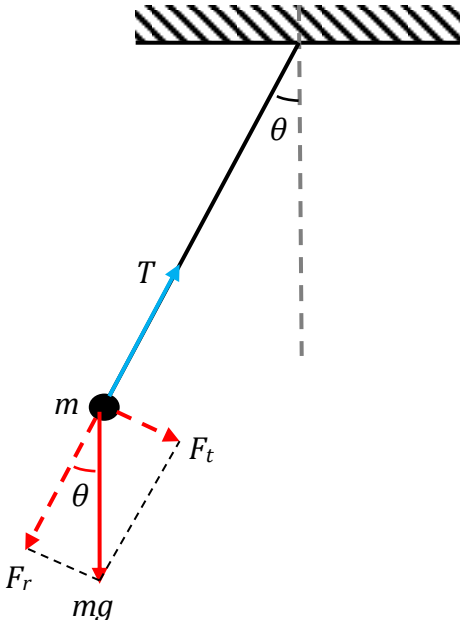

Fig. 3.1 – Simple harmonic motion of an oscillating pendulum

The presence of the trigonometric term $sin\,\theta$ makes equation (3.1) nonlinear. Using Taylor series, the sine function can be expanded to

$$sin\,\theta = \theta - \frac{1}{6}\theta^3 + \cdots \tag{3.3}$$

However, for most analytical solutions, equation (3.1) is linearised by the following approximation

$$sin\,\theta \approx \theta; \quad \theta < \frac{\pi}{6} \tag{3.4}$$

As long as the vibration amplitudes are kept small, this system can be approximated to be linear. With large amplitudes of vibration, the nonlinear terms become more significant and the pendulum behaviour is modelled more accurately by incorporating nonlinearity in the equations of motion. The Duffing equation is one such example which takes into account the effect of the trigonometric term in equation (3.1)

The Duffing equation (3.5) was developed to study the steady-state response of a nonlinear system subjected to periodic excitation. It models a forced nonlinear oscillator with linear damping (Fig. 3.2). This equation can be written as

$$m\ddot{x} + c\dot{x} + kx \pm k_3 x^3 = F\cos\omega t \tag{3.5}$$

In this equation, k_3 is the cubic stiffness coefficient. The $\pm$ term indicates either a hardening or a softening system. The cubic term x^3 in the equation is used to mimic the sinusoidal term in equation (3.1) and is dependent on the amplitude of the vibration.

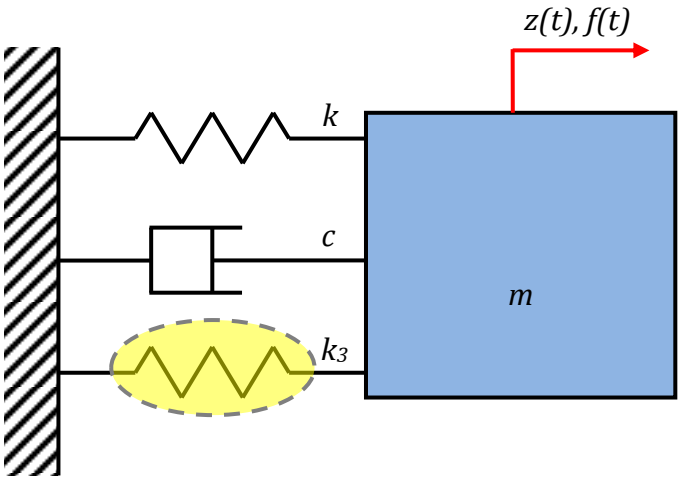

Fig. 3.2 – Nonlinear system described by the Duffing equation

Two different types of nonlinear behaviour can be expected (Fig. 3.3):

(i) Spring softening – in this case, the value of k_3 decreases with increase in frequency and results in the response peak of a typical frequency-amplitude curve becoming asymmetric and leaning to the left. The amplitude increases with decrease in frequency.

(ii) Spring hardening – the value of k_3 increases with rise in frequency, resulting in the response peak of a frequency-amplitude curve becoming asymmetric and leaning to the right. Hardening of a system indicates

that the amplitude response of the cantilever beam will increase with increase in frequency.

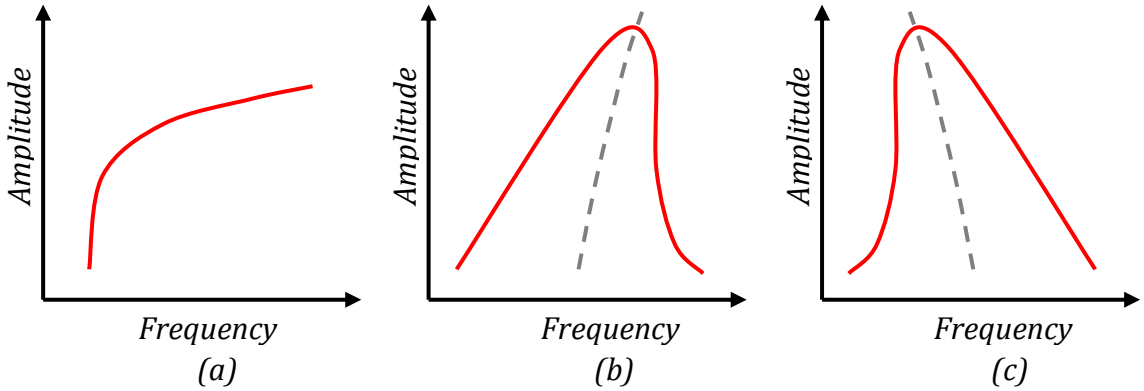

Fig. 3.3 – Frequency response curves for (a) theoretical (b) hardening and (c) softening spring systems

Theories which have attempted to predict hardening and softening behaviour often portray an infinite increase in amplitude with increase in excitation frequencies. This is illustrated in Fig. 3.3(a).

Nonlinearities present in a system leads to jumps in the frequency- and force-response curves. The nonlinear response curves are multivalued; that is, there are two amplitude responses at the same frequency. This leads to the jump phenomenon (Fig. 3.4) where at frequencies close to the resonant frequency, the vibration amplitude of the system can jump from value to another at the same frequency. This can be quite damaging to the system. Damping tends to reduce the size of unstable region.

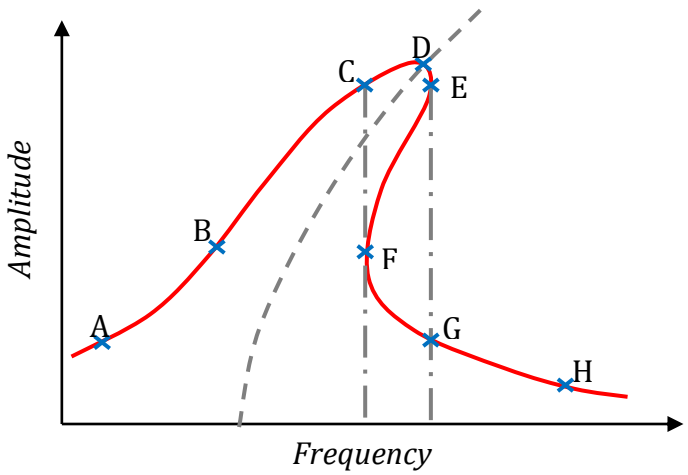

Fig. 3.4 – Jump phenomenon; ABCDE and FGH are stable regions. Segment FE corresponds to an unstable region

3.1.2 Material Nonlinearity

Nonlinear material behaviour is observed when the applied stress does not vary linearly with strain (Fig. 3.5).

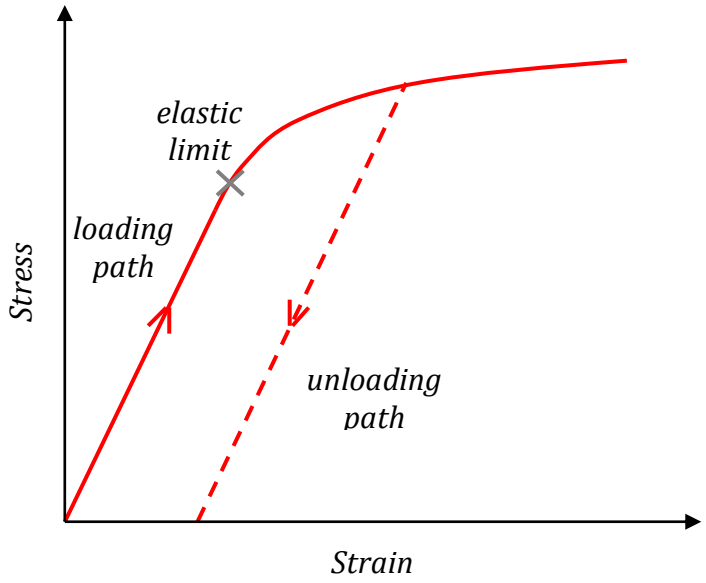

Fig. 3.5 – Stress-strain curve for nonlinear material behaviour

A linear relationship exists between stress and strain till the elastic limit. In the elastic region, the material can be loaded and unloaded repeatedly along the same loading path. However, once the applied stress exceeds the maximum yield strength, the material exhibits plastic behaviour and the unloading path is as

shown in Fig. 3.5. The deformation is not recovered once the applied loads are removed; therefore, creep and strain rate are not taken into account once the material deforms plastically.

3.1.3 Nonlinearities Due to Damping and Friction

Damping is inherently present in any vibrating structure. Viscous damping models are the most commonly used to model damping. Energy dissipation due to viscous damping is calculated by

$$W_d = \int c\dot{x}\ dx \tag{3.6}$$

$$W_d = \pi c\omega \dot{X}^2 \tag{3.7}$$

Various types of damping can have an effect on structural response; the two most relevant to this project – structural and Coulomb damping – are described below.

Structural damping is present due to inherent intermolecular friction. Energy dissipation due to structural damping is calculated by

$$W_d = \alpha X^2 \tag{3.8}$$

and the equivalent viscous damping is calculated by

$$C_{eq} = \frac{\alpha}{\pi\omega} \tag{3.9}$$

Many common structures exhibit nonlinear behaviour that is status dependent. When the status of the physical system changes, its stiffness shifts abruptly. The stiffness of a structure can often be used to identify if the system is linear or nonlinear. Stiffness can be affected by a number of factors such as the shape, material and support. When contact occurs between two surfaces, contact stresses can develop. Although the contact area is relatively small compared to the entire model, the stiffness of the contact zone tends to change during the analysis; therefore, nonlinear analysis can be used to model contact.

During sliding contact, friction exists between the two contacting surfaces. This is modelled by Coulomb friction. A system being acted upon by Coulomb damping is nonlinear because the frictional force always opposes the direction of motion of the system as stated earlier. Due to the presence of friction, the amplitude of the motion decreases with time (Fig. 3.Fig. 3.6). Under the influence of Coulomb damping, the amplitude decays linearly with a slope of $\pm 2\mu mg\omega_n / \pi k$ where ω_n is the natural frequency. The equations of motion for Coulomb damping are

$$m\ddot{x} + K(x \pm \Delta) = 0 \tag{3.10}$$

$$m\ddot{x} + Kx = \mp K\Delta \tag{3.11}$$

Taking into account boundary conditions of zero displacement and velocity at $t = 0$ gives

$$x = \mp\Delta + (x_0 \pm \Delta)\, cos\, pt \tag{3.12}$$

$$\dot{x} = -(x_0 \pm \Delta)\, p\, sin\, pt \tag{3.13}$$

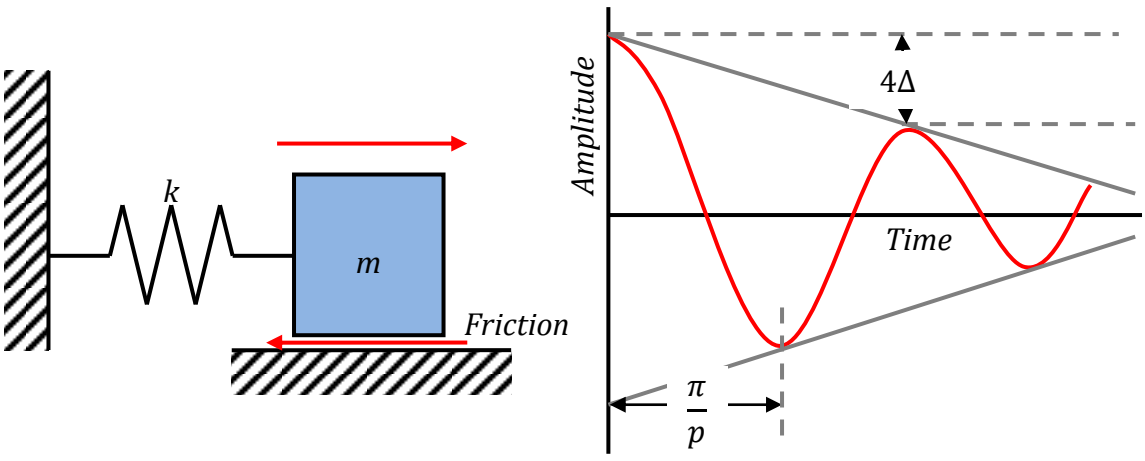

Fig. 3.6 – Coulomb damping system

Generally, damped harmonic oscillation can be represented by the second-order differential equation

$$\frac{d^2x}{dt^2} + 2\zeta\omega_0 \frac{dx}{dt} + {\omega_0}^2 x = 0 \tag{3.14}$$

where ω_0 is the natural frequency and ζ is the damping ratio. These are calculated by

$$\omega_0 = \sqrt{\frac{k}{m}} \tag{3.15}$$

$$\zeta = \frac{c}{2\sqrt{km}} \tag{3.16}$$

The value of the damping ratio ζ determines the behaviour of the system (Fig. 3.7). If ζ is less than 1, the system is said to be underdamped and the oscillations eventually decrease to zero; if ζ is greater than 1, the system does not oscillate at all and returns to equilibrium. The fastest return to equilibrium occurs when ζ equals one; the system is now said to be critically damped.

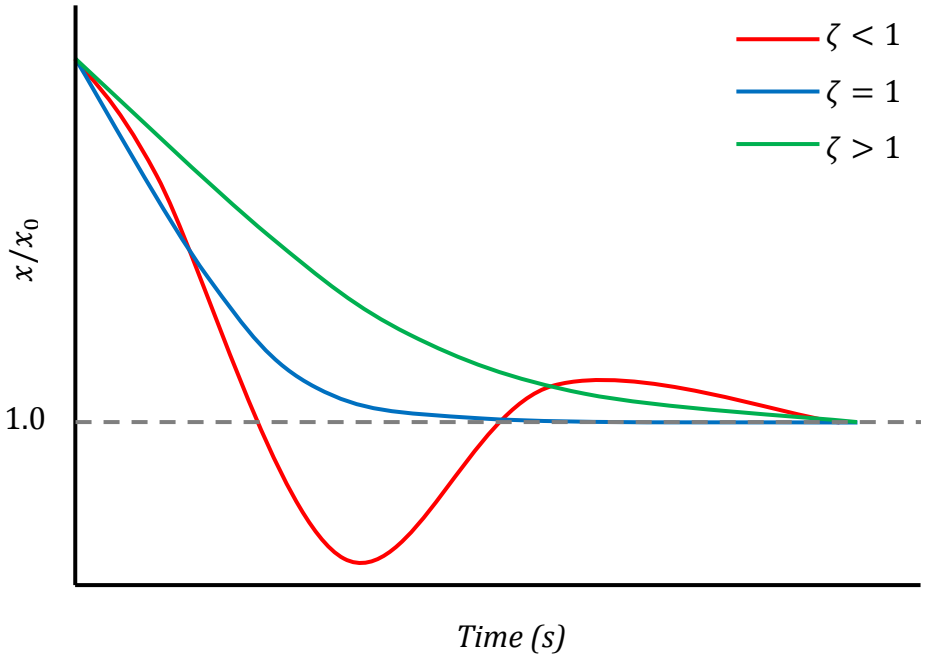

Fig. 3.7 – Effect of damping ratio on system behaviour

3.2 Analytical Modelling of Modified Jeffcott Rotor with Rub

Although a large amount of research has been carried out on tip-rubbing, papers on stability of blade motion after the event are relatively few. This could be attributed to the difficulty of stability analysis of nonlinear systems. In order to carry out a systematic parametric study, the stability of the full annular rub motion of a Jeffcott rotor with a symmetric clearance effect will be studied. The analytical model presented was developed in [30] and the reader should refer to the article for a more complete understanding of the dynamics involved.

The Jeffcott rotor was conceived in 1919 by Jeffcott. This consists of a rigid disc located on a flexible rotating shaft, mounted on bearings at each end [29]. A modified Jeffcott rotor, also known as a Laval rotor (Fig. 3.8), is considered for this section.

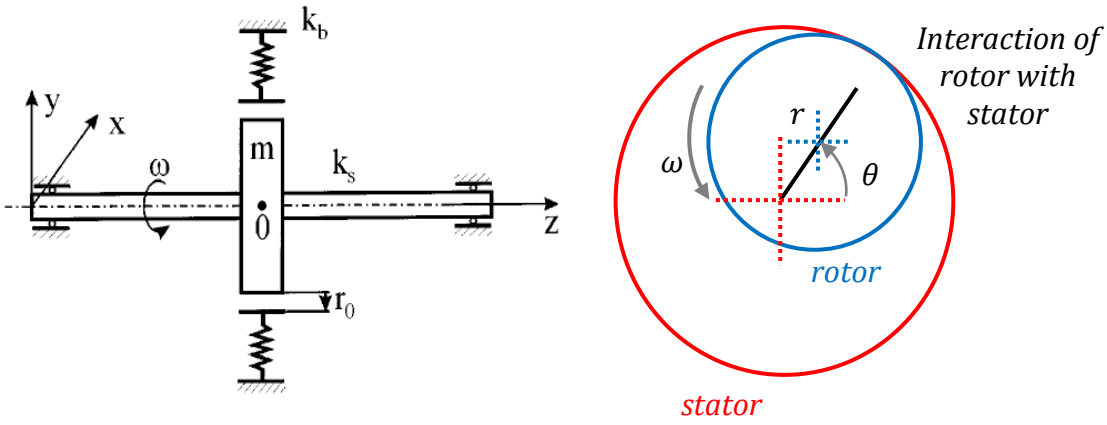

Fig. 3.8 – (a) Laval rotor [30] (b) With rubbing effect

The clearance between the rotor and the stator is denoted by r_0. The shaft is considered to be massless and to have stiffness of k_s; the mass of the disc is m. The stator is considered to be rigid, supported by springs of stiffness k_b.

When rotor eccentricity e is less than r_0, the equations of motion of this system can be expressed as

$$m\ddot{x} + c\dot{x} + k_s x = me\omega^2 \cos\ \omega t \tag{3.17a}$$

$$m\ddot{y} + c\dot{y} + k_s y = me\omega^2 \sin\ \omega t \tag{3.17b}$$

If e exceeds r_0 rotor-stator interaction occurs and the equations of motion (3.17) become nonlinear in nature and can be written as

$$m\ddot{x} + c\dot{x} + k_s x + k_b \left(1 - \frac{r_0}{r}\right)(x - \mu y) = me\omega^2 \cos\ \omega t \tag{3.18a}$$

$$m\ddot{y} + c\dot{y} + k_s y + \ k_b \left(1 - \frac{r_0}{r}\right)(\mu x - y) = me\omega^2 \sin\ \omega t \tag{3.18b}$$

where

r = displacement of shaft geometric centre (3.19)

μ = coefficient of friction (3.20)

$$r = \sqrt{x^2 + y^2} \tag{3.21}$$

In order for the assumption of nonlinearity to be correct, the vibration amplitude needs to be real and greater than the rotor clearance r_0. Equations (3.17) can be written non-dimensionally as:

$$\ddot{X} + 2\zeta\dot{X} + \beta X = \Omega^2 \cos\ \Omega\tau \tag{3.22a}$$

$$\ddot{Y} + 2\zeta\dot{Y} + \beta Y = \Omega^2 \sin\ \Omega\tau \tag{3.22b}$$

Similarly, equations (3.18) can be re-written non-dimensionally as:

$$\ddot{X} + 2\zeta\dot{X} + \beta X + \left(1 - \frac{R_0}{R}\right)(X - \mu Y) = \Omega^2 \cos\ \Omega\tau \tag{3.23a}$$

$$\ddot{Y} + 2\zeta\dot{Y} + \beta Y + \left(1 - \frac{R_0}{R}\right)(\mu X + Y) = \Omega^2 \sin\ \Omega\tau \tag{3.23b}$$

Where the non-dimensional variables are as follows:

$$X = \frac{x}{e}, \qquad Y = \frac{y}{e}, \qquad R = \frac{r}{e}, \qquad R_0 = \frac{r_0}{e}, \qquad \beta = \frac{k_s}{k_b} \tag{3.24}$$

$$R = \sqrt{X^2 + Y^2}, \quad {\omega_2}^2 = \frac{k_b}{m}, \quad \frac{c}{m} = 2\zeta\omega_2, \quad \Omega = \frac{\omega}{\omega_2}, \quad \tau = \omega_2 t$$

Both the linear equations (3.22) and nonlinear equations (3.23) have steady-state periodic solutions of the following form

$$X = A\cos\ (\Omega\tau + \psi) \tag{3.25a}$$

$$X = A\sin\ (\Omega\tau + \psi) \tag{3.25b}$$

The amplitude and phase angle of equations (3.22) is given by

$$A = \frac{\Omega^2}{\sqrt{(\beta - \Omega^2)^2 + 4\zeta^2\Omega^2}} \tag{3.26}$$

$$\psi = \frac{-2\zeta\Omega}{\beta - \Omega^2} \tag{3.27}$$

Equations (3.26) and (3.27) are only valid when the amplitude of vibration is less than the clearance R_0. This gives

$$\left({R_0}^2 - 1\right)\Omega^4 + {R_0}^2(\beta^2 - 2\beta + 4\zeta^2)\Omega^2 \leq 0 \tag{3.28}$$

Solving equation (3.28) gives two real roots for Ω; the steady-state periodic solution to equations (3.22) will only exist between these two roots. The first resonant frequency is considered by setting $\Omega^2 = 1 + \varepsilon\sigma$, where ε and σ are perturbation and detuning parameters respectively for approximating the resonant frequency. This gives the following solutions to equations (3.23):

$$A' = \frac{\varepsilon}{2}(\gamma A + E\sin\theta) \text{ for } R \leq 1 \tag{3.29a}$$

$$A' = \frac{\varepsilon}{2}(\gamma A - g\mu + g\mu A + E\sin\theta) \text{ for } R > 1 \tag{3.29b}$$

$$A\theta' = \frac{\varepsilon}{2}\left(-\frac{3}{4}A^3\beta + \sigma A + E\cos\theta\right) \text{ for } R \leq 1 \tag{3.30a}$$

$$A\theta' = \frac{\varepsilon}{2}\left(-\frac{3}{4}A^3\beta + \sigma A + E\cos\theta + g - gA\right) \text{ for } R > 1 \tag{3.30b}$$

By setting $A' = 0$ and $\theta' = 0$, the frequency-amplitude responses can be derived as

$$f_1 = 9\beta^2 A^6 - 24\beta A^4(\sigma + g) + 16A^2(\sigma^2 + \gamma^2) - 16E^2 = 0 \text{ for R } \leq 1 \quad (3.31)$$

$$\begin{aligned} f_2 = {} & 9\beta^2 A^6 - 24\beta A^4\sigma + 16A^2(\sigma^2 - 2g\sigma + 2\gamma g\mu + g^2 + \gamma^2 + g^2\mu^2) \\ & + 32gA(\sigma - g - g\mu^2 - \gamma\mu) + 16(g^2\mu^2 + E^2 + g^2) \\ & = 0 \text{ for R } \leq 1 \end{aligned} \quad (3.32)$$

Fig. 3.9 shows the amplitude-frequency curve of the full annular rub of the rotor system; it can be seen that the amplitude-frequency curve consists of two parts. If $0 < A \leq 1$ the curve is determined by equation (3.31); however, if $A > 1$, it indicates that rub occurs and the resulting curve is determined by equation (3.32).

The tip-rubbing analysis considered in this thesis is expected to result in the same behaviour as shown in Fig. 3.9. It should be remembered that the amplitude of vibration should be real, positive and greater than R_0 in order to ensure that differential equations (3.25) are correct.

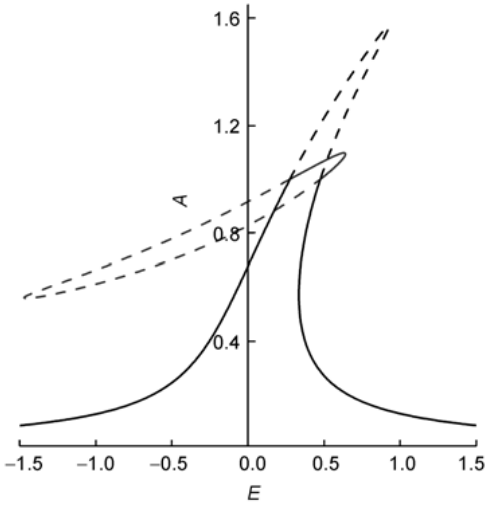

Fig. 3.9 – Frequency-amplitude curve of synchronous full annular rub [30]

Chapter 4 – Modelling Considerations

4.1 Methodology

The blade tip-rubbing phenomenon is essentially forced excitation applied to a multiple degree of freedom system. If the excitation frequency coincides with one or more of the resonant frequencies of the system, a condition of resonance is encountered which can easily lead to large-amplitude vibrations and consequently catastrophic failure of the system.

The following methodology will be adopted for this project:

1. Simplification of the model – Before any simulation can be carried, it is essential to mesh the model in order to define elements which can be solved computationally. The blade model has been meshed prior to this project and no change in the blade mesh is required. However, the groove at the disc where the blade is attached needs to be modified in order to obtain a closer approximation of the actual geometry; this will be done using Altair Hypermesh.

2. Stress initialisation due to centrifugal loads – It is essential that the prestress on the system due to centrifugal loads should be defined before simulating the tip-rubbing event. It is necessary to determine that the centrifugal loads have converged to a steady-state value. The parameters essential for this are defined in Altair Hypermesh.

3. Modal analysis – It is important to gain an understanding of the resonant frequencies of the system, and to identify if excitation frequencies match resonant frequencies. The natural frequencies of the compressor blade will be determined by finite element analysis. For comparison purposes, the modal analysis will be conducted using LS-DYNA and ANSYS. A second modal analysis will be conducted to study the effect of centrifugal loads on resonant frequencies.

4. Dynamics of the tip-rubbing event – This is a nonlinear event which will be processed using LS-DYNA. Post-processing of this event to extract relevant results will be done using LS Pre-Post and SIGVIEW.

4.2 Simulation Tools

The simulation of compressor blade tip-rubbing required five key software to be used, each of which served a different purpose. Since only the LS-DYNA keyword file of the simulated model was provided, any changes to the geometry first required creation of the geometry from elements in the LS-DYNA file. This was done by generating geometry in CATIA V5R20 from the imported LS-DYNA file.

Altair Hypermesh was chosen as the pre-processor for this project because it provides a GUI (Graphical User Interface) environment that allows the user to define the keywords for defining boundary conditions of simulations. Also, Hypermesh allows good control over mesh size, and provides a good platform for importing geometry from CATIA V5R20 and for exporting files for finite element analysis.

LS-DYNA was developed by LSTC (Livermore Software Technology Corporation) to solve highly nonlinear, transient dynamic finite element analysis using explicit time integration. LS-DYNA was chosen as the finite element analysis software for this project because it has been used successfully in the past for solving nonlinear problems due to turbofan engine blade tip-rubbing [15] [26]. Also, because of its wide range of contact algorithms and extensive material database, LS-DYNA enables the user to simulate complicated finite element problems. The blade-casing impact event is a highly nonlinear problem because the contact between the two parts evolves with time; also, the blade is expected to undergo large deformations post impact.

LS-PrePost is a pre- and post-processor for LS-DYNA provided by LSTC. This software was mostly used for post-processing results from simulations, and for generating relevant pictures and animations.

SIGVIEW is a signal analysis shareware package which was also used to post-process time series data and generate FFT (Fast Fourier Transform) plots.

The GRID HPC (High Performance Computing) facilities available at Cranfield University were used to run the larger models. This allowed substantial savings in computation time.

The simulations studied for this project and their purpose are illustrated in the following flowchart (Fig. 4.1).

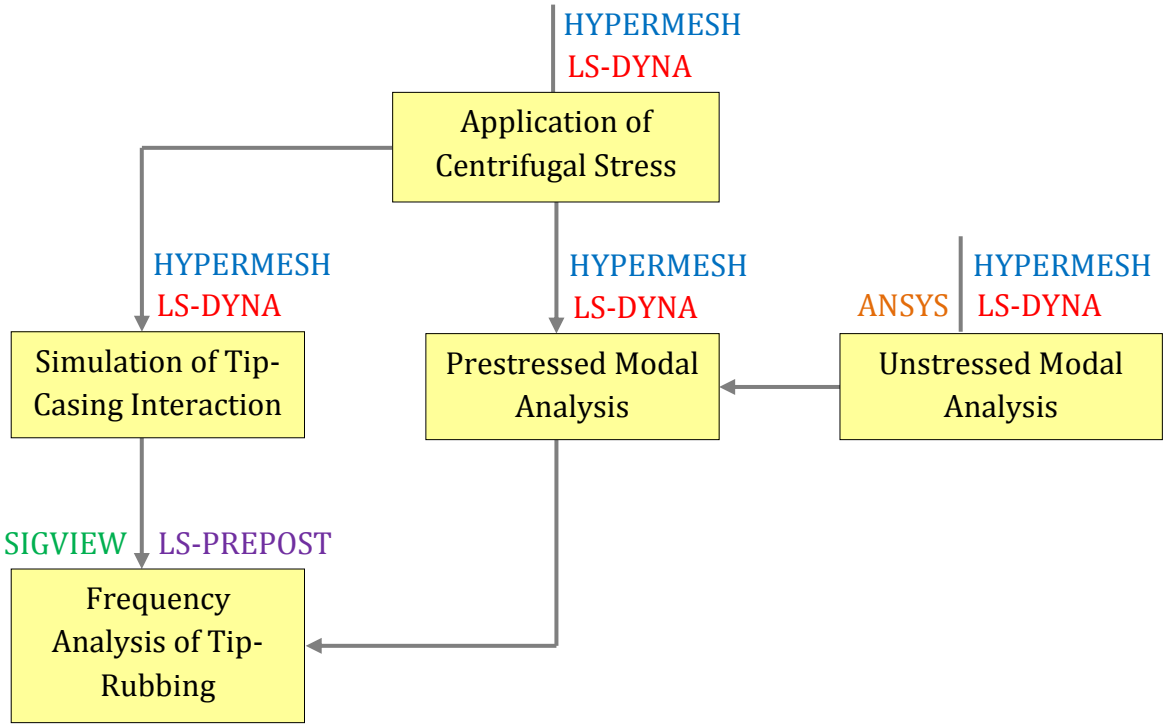

Fig. 4.1 – Structure of simulations

4.3 Units Used

LS-DYNA has no unit system; therefore, it is necessary to define a consistent set of units for the model. The units used for this project are shown in Table 4.1.

Table 4.1 – Units used

Quantity	Units
Length	m
Time	s
Frequency	Hz
Angular Velocity	rad/s
Density	kg/m^3
Mass	kg
Force	N
Stress	Pa

4.4 Casing Geometry

The geometry of the casing was taken from previous projects done on the tip-rubbing analysis and a brief description is mentioned here for completeness. For a more detailed description, the reader should refer to [15] and [23].

The design for the casing was decided upon parameters suggested by Rolls-Royce. Only part of the casing had been modelled. Rolls-Royce requested that the casing should be designed such that the blade incursion into the casing is ramped linearly from zero to a maximum of 10 μm. The casing is meshed using hexahedral elements. Material properties of the casing are given in Section 4.7. The geometry of the casing is shown in Fig. 4.2.

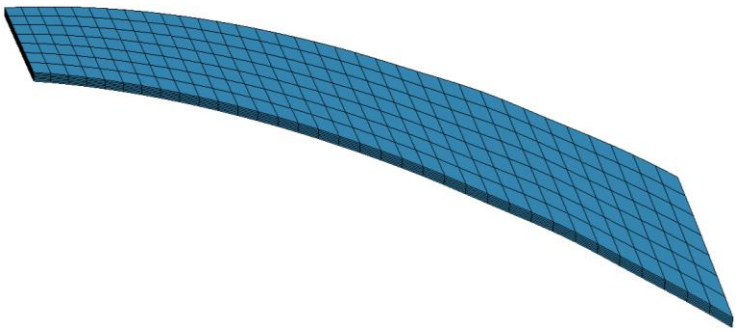

Fig. 4.2 – Geometry and mesh of compressor casing

4.5 Blade Geometry

The compressor blade dimensions have been provided by Rolls-Royce and are mentioned in Table 4.2 for completeness.

Table 4.2 – Compressor blade dimensions

Quantity	Length (mm)
Top blade diameter	56.6
Bottom blade diameter	66
Length of leading edge	124.7
Length of trailing edge	115.1
Distance between leading edge tip and base	136.5
Distance between trailing edge tip and base	129.2
Base length	65.2
Distance between blade root and rotation axis	334.7 (leading edge) 337.5 (trailing edge)

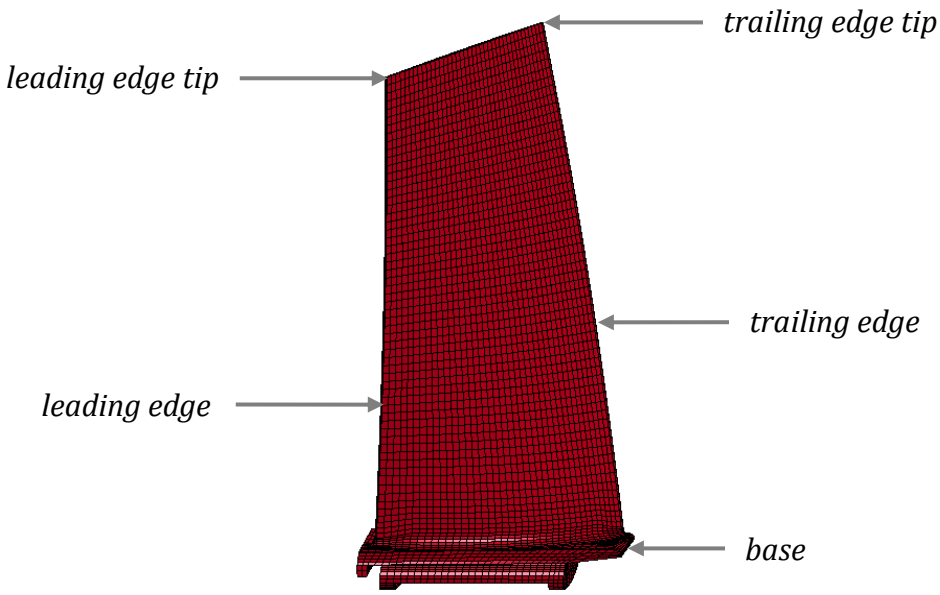

Fig. 4.3– Compressor blade geometry and mesh

4.5.1 Blade Plastic-Kinematic Material Model

For most metals, the yield strength increases as the strain rate increases. The *MAT_PLASTIC_KINEMATIC model available in LS-DYNA is suited to include strain rate effects. This model was formulated by Krieg and Key [5]. The variables used for the blade are shown in Table 4.3.

*Table 4.3 – Values for *MAT_PLASTIC_KINEMATIC card*

Variable	Value
σ_{scaled}	1.098E GPa
E_{tan}	1.972 GPa
C	120
p	9

σ_{scaled} is the scaled yield strength and is calculated by the Cowper-Symonds model as follows:

$$\sigma_{scaled} = \sigma_0 \left[1 + \left(\frac{\dot{\varepsilon}}{C}\right)^{\frac{1}{p}}\right] \tag{4.1}$$

The values of $C = 120\ s^{-1}$ and $p = 9$ are assumed for this project [32]. $\dot{\varepsilon}$ is determined numerically by initially modelling both the blade and the casing as elastic with the *MAT_ELASTIC card. The uniaxial strain rate $\dot{\varepsilon}$ is then determined to be $4.216 \times 10^{-4}\ s^{-1}$. This gives the value of $\sigma_0 = 1.098$ GPa.

E_{tan} is the gradient of the bilinear stress-strain curve (Fig. 4.4). The yield strain ε_0 is considered insignificant and therefore ignored. Therefore E_{tan} is approximated as

$$E_{tan} = \frac{\sigma_{fail} - \sigma_0}{\varepsilon_{fail} - \varepsilon_0} \cong \frac{\sigma_{fail} - \sigma_0}{\varepsilon_{fail}} \tag{4.5}$$

where

$$\varepsilon_{fail} = ln\left(\frac{l_0}{l_{fail}}\right) \tag{4.6}$$

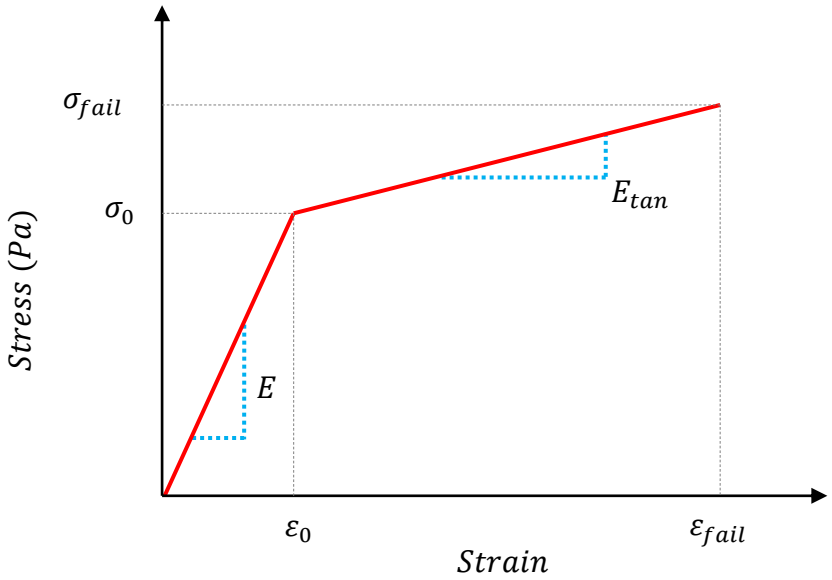

Fig. 4.4 – Bilinear stress strain curve

It should be noted that initially the Cowper-Symonds formulation was set to incorporate the yield surface of the blade when it interacts with the casing. However, this resulted in the material model not converging. Initially this was thought to be an issue with setting the timestep manually instead of allowing the software to set it automatically (see Section 7.2.2); this was found out to not be the case. Non-convergence of the material model could have probably been solved by using a model which has a better iterative solver such as *MAT_24. However, this improvement was realised at a late stage in the project and therefore not incorporated into the thesis.

4.6 Modification of Blade Geometry

Previous work done on this project (see [15] and [23]) did not take into account the effect of the disc groove on the dynamics of a tip-rubbing event, but did acknowledge its significance. The modelling of this geometry is likely to have a significant impact on the results obtained since it defines the constraints on the blade. In this project, the blade root has been modelled with a closer

approximation to the real geometry. The meshing of this geometry proved to be quite challenging.

The model file provided to the author contained information about the mesh, but no information was available about the geometry. Therefore, it was necessary to generate a solid model of the blade from the mesh provided, and to perform a Boolean subtraction on a solid geometry of the disc section. This is shown in Fig. 4.5.

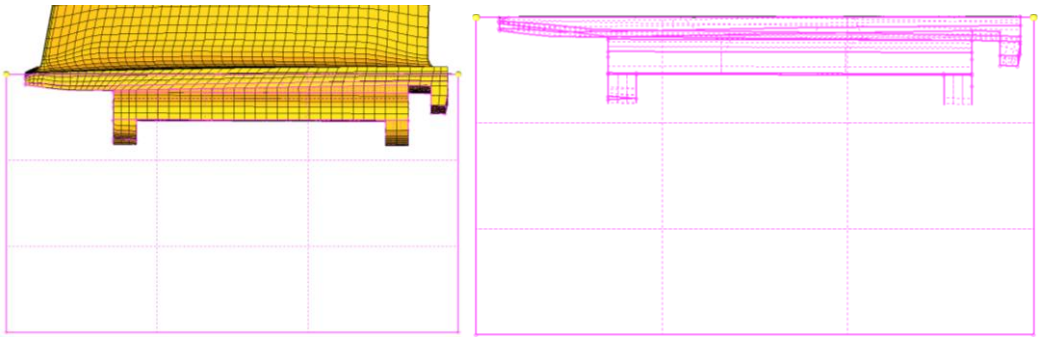

Fig. 4.5 – Disc groove generated by Boolean subtraction from blade root profile

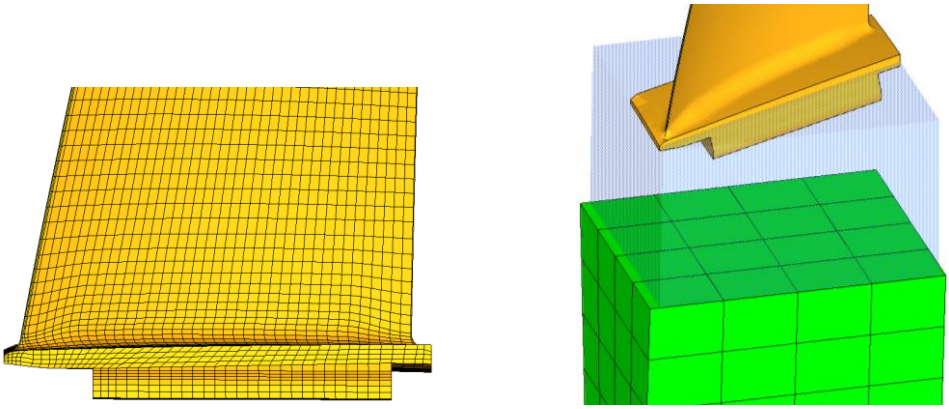

Fig. 4.6 – Simplified blade and section of disc in contact with blade

The disc geometry was further simplified to ease the meshing process; consequently, the blade geometry was also simplified (Fig. 4.6). The section of the disc in contact with the blade has been meshed using tetrahedral elements. Although many attempts have been made to model the groove in the disc using

hexahedral elements in order to maintain consistency, the complex geometry did not allow this to happen. Therefore, the section of the disc containing the groove for the blade root was meshed using tetrahedral elements with Type 1 element formulation. Since the disc will be modelled as a rigid body, the type of mesh used does not affect the analysis. However, for maintaining good contact during analyses, the section of the disc not containing the groove was also meshed with Type 1 tetrahedral elements. The final meshed model of the disc is shown in Fig. 4.7.

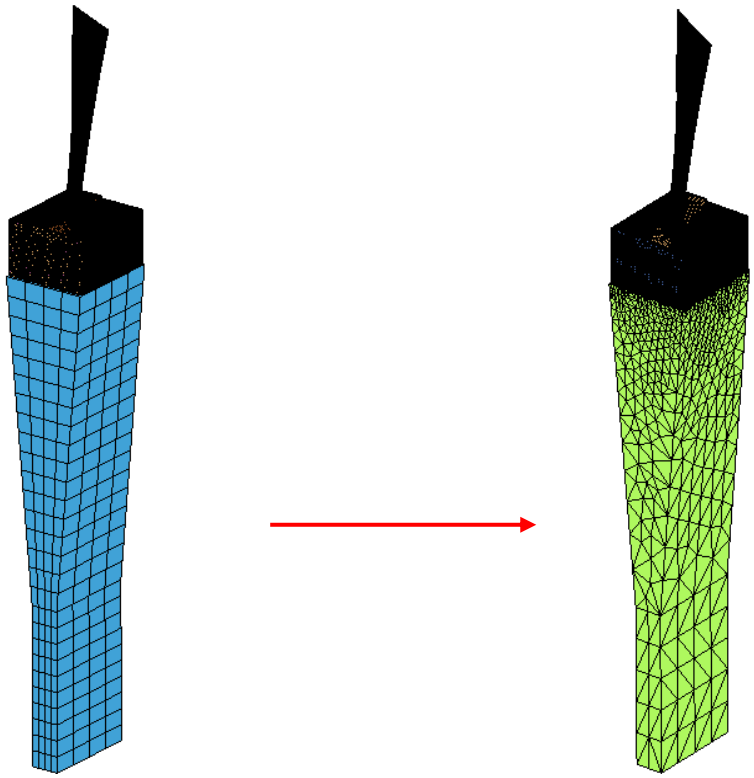

Fig. 4.7 – Remeshing of disc using tetrahedral elements

When this modified model was run in LS-DYNA, the input file size was very large and took a long time to solve. Also, another way of simplifying the analysis was realised at this stage; this was to remove the disc altogether and instead constrain the blade at the root to mimic the constraining effect of the disc. Previously, it was understood that the presence of the disc was necessary in order to provide an axis of rotation.

Although the removal of the disc is most likely to have an effect on the frequency content of the analyses, the objective of this project is to look at the local blade-casing interaction and not the global picture of the compressor. The final model of the blade chosen for the subsequent analyses for this project is shown in Fig. 4.8.

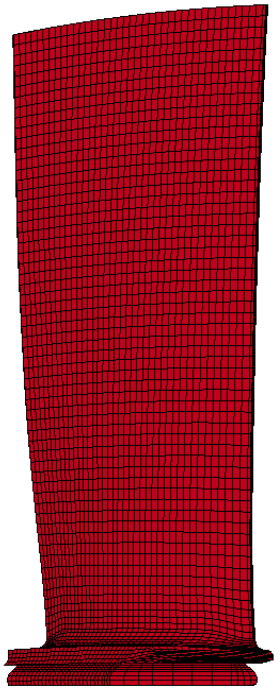

Fig. 4.8 – Final blade model

4.7 Material Properties and Models

Table 4.4 below outlines the material properties and models used. Appendix E contains more detailed information about the material properties of Ti-6Al-4V.

Table 4.4 – Material properties of blade and casing

Part	Material	ρ (kg/m^3)	E (GPa)	ν	Material Model
Blade	Titanium Ti-6Al-4V	4430	113.8	0.342	MAT_003 (Plastic Kinematic)
Casing	Abradable material	4430	8	0.330	MAT_001 (Elastic)

It should be noted that no material data was provided for the abradable material lining the casing; the properties presented in Table 4.4 were decided on the basis that the casing should have a low Young's modulus so that it behaves elastically during contact, and that erosion of the blade tip or casing material should not occur during the tip-rubbing analysis. An accurate modelling of the abradable layer would give more realistic results about the dynamics involved. This could be achieved by defining a layer of foam elements on the inner surface of the casing to model the abradable layer. However, the current model serves the purpose since the effect of tip-rubbing on the casing is not of interest to this project.

Chapter 5 – Stress Initialisation Due to Rotation

An object rotating with a constant angular velocity experiences a constant centrifugal force, given by equation (5.1)

$$F = m\omega^2 r \tag{5.1}$$

Where F is the centrifugal force, m is the mass of the spinning object, ω is the angular velocity and r is the radial distance from the axis of rotation. The centrifugal force generated is a static force which creates a state of constant stress in the rotating object that does not vary with time.

Stress initialisation due to centrifugal forces is the first phase of any transient analysis of a dynamic event on the blade such as blade tip-rubbing, bird strike or fan blade-off events. It should be noted that there are other loads on the blades such as gas loads and thermal loads. However, due to the relatively small magnitudes these loads are disregarded in this project.

The following sections demonstrate how this constant stress state was applied to the compressor blade. The techniques used to validate the prestress are also discussed.

There are numerous approaches for applying the prestress for a rotating blade in LS-DYNA; two methods have been investigated in this project:

(i) The *CONTROL_DYNAMIC_RELAXATION card

(ii) An implicit prestress static solution followed by an explicit transient solution.

Both methods have been studied on a sensitivity model which has fewer elements and is therefore computationally less expensive to run. The second approach has been found to be the more robust of the two.

The following sections also contain the LS-DYNA keyword cards used for the models. In general, variables left to default values will not be discussed in detail and the reader should refer to the LS-DYNA 971 Keyword Manual [5] and LS-DYNA Theory Manual [6] for further explanation of the cards used.

5.1 Sensitivity Model – Stress Initialisation by Dynamic Relaxation Card

The compressor blade is set to rotate at an angular velocity of 890 rad/s (8500 rpm). The acceleration of the blade from a state of rest to the prescribed angular velocity causes transient vibration of the compressor blade, which could potentially complicate the results from a tip-rubbing event if not allowed to converge properly. The determination of the centrifugal force is important in this analysis because it is expected to have a noticeable effect on the blade resonant frequencies. Hence, it is important that the centrifugal forces achieve a stable state prior to any dynamic analysis. This is done by the process of dynamic relaxation.

The dynamic relaxation method converges the system to a stable state; this is done by the introduction of certain parameters which force the system to converge to a stable state. Damping is applied to system by multiplying the angular velocity with a damping factor. In order for the system to converge to a stable value, the ratio of the current distortional kinetic energy to peak distortional kinetic energy should be less than the convergence tolerance limits specified. Once the solution converges, dynamic relaxation stops.

The sensitivity model consists of a single blade attached to a disc section. The centre of the disc has been constrained in translational degrees of freedom. Previously, in [15] and [23], a rigid support at the axis of rotation was attached to the disc with a *CONSTRAINED_JOINT_REVOLUTE card which creates a revolute

joint between two rigid bodies. The objective of this rigid support was to provide an axis of rotation. However, after dynamic relaxation, the model showed axial vibrations exceeding 50 μm.

Possible reason for this excessive vibration could be due to the fact that although the revolute joint existed between two rigid bodies, the disc was connected to the elastic blade which in turn was subjected to centrifugal force due to rotation. Contact between the blade and the disc was defined by the *CONSTRAINED_EXTRA_NODES_SET card, which created rigid nodes at the blade root and connected them to the disc. An optional card available in LS-DYNA is the *CONSTRAINED_JOINT_STIFFNESS_OPTION, which allows definition of joint stiffness specified by revolute joint card. This optional card had not been used for the revolute joint between the disc and the rigid support. It is assumed that lack of proper joint stiffness definition led to excessive axial vibration of the disc which was transmitted through to the blade.

Further research into this was not carried out since the presence of the rigid support as an axis of rotation was deemed unnecessary and therefore removed. The disc was instead constrained in all six degrees of freedom (three translational, three rotational) at the axis of rotation by the *BOUNDARY_SPC_NODE card. The removal of the support and the revolute joint reduced the vibration to 1 μm (Fig. 5.2).

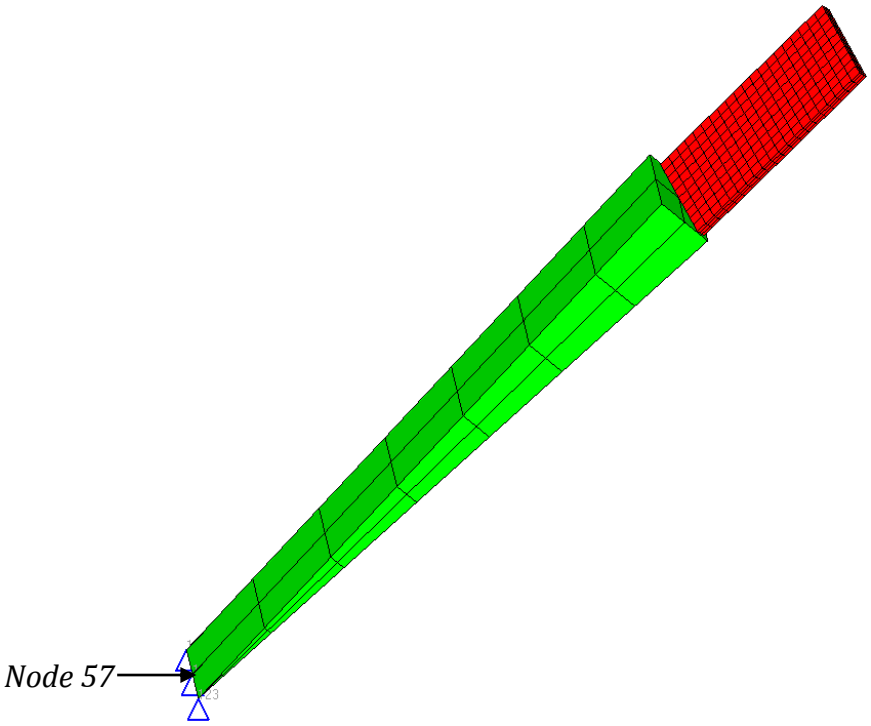

Fig. 5.1 – Sensitivity model constrained at base

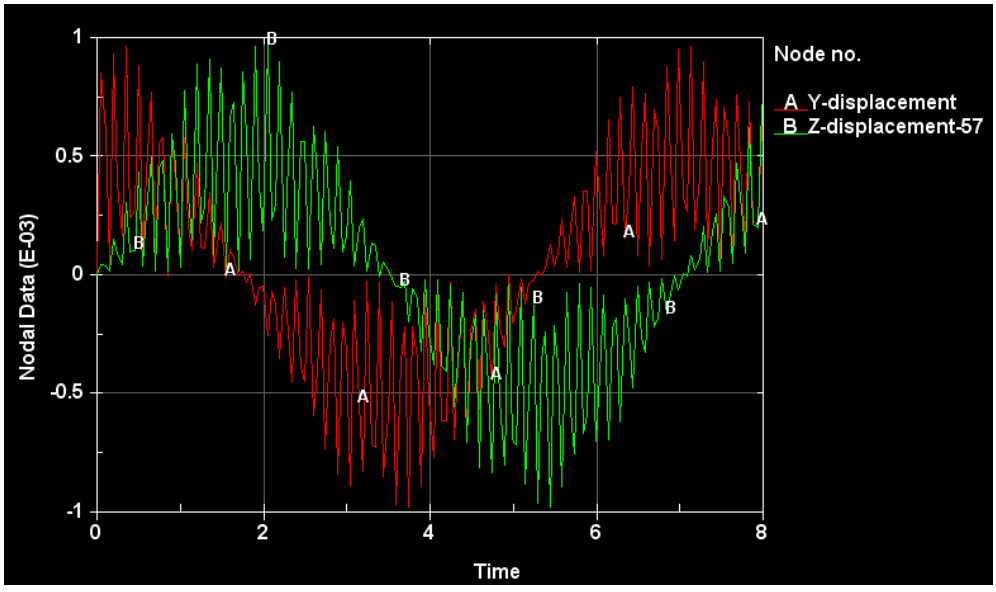

Fig. 5.2 – Axial displacement of Node 57 [Units: time (s), Nodal Data (mm)]

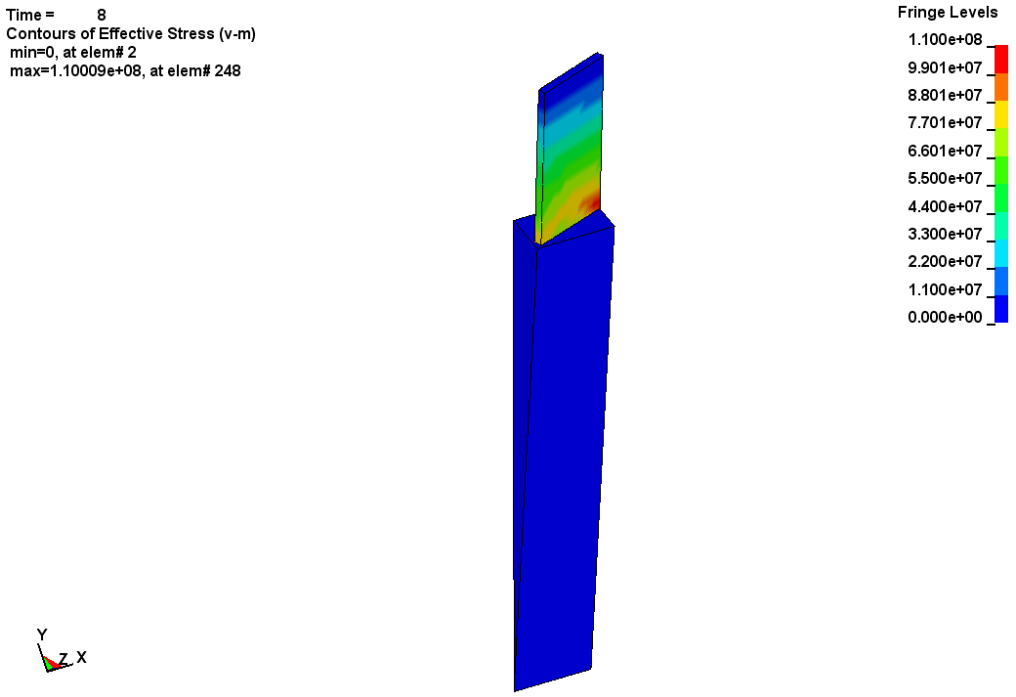

Fig. 5.3 – Von Mises stress distribution on sensitivity model [Units: Pa]

The maximum stress values seen at the root are close to 100 MPa. These results are verified by hand calculation using equation (5.2)

$$\sigma = \frac{\rho\omega^2[R^2 - r^2]}{2} = \frac{2700 \times 890^2[0.44^2 - 0.33^2]}{2} = 90.6 \text{ MPa} \qquad (5.2)$$

where ρ is the density of aluminium, ω is the angular velocity, R is the hub radius and r is the blade radius, both radii measured from the axis of rotation. This gives a calculated stress of 90.6 MPa at the blade root.

Fig. 5.4 shows the convergence rate plot for dynamic relaxation. Convergence is the ratio of the current distortional energy to maximum distortional energy. The solution is said to converge if

$$cv_{tol} > \frac{KE}{KE_{max}} \qquad (5.3)$$

where cv_{tol} is the convergence tolerance.

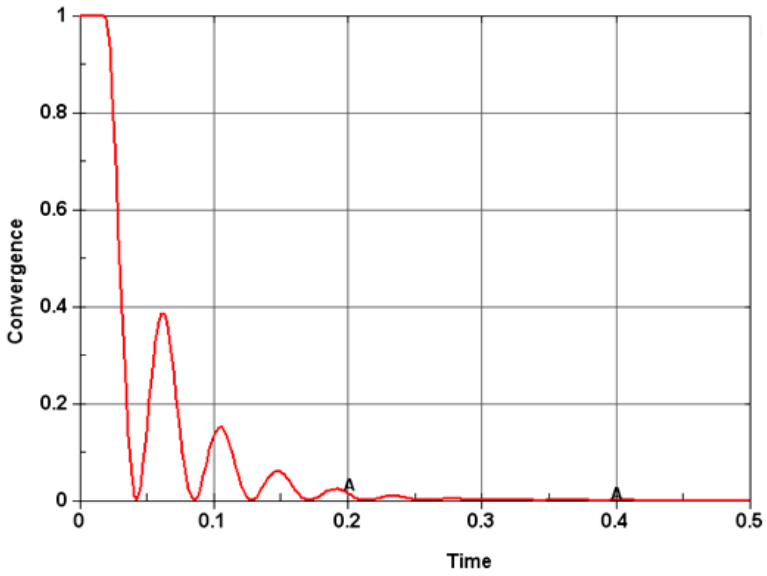

Fig. 5.4 – Convergence rate for model [Units: Time (s)]

Additional effort was made to improve upon the sensitivity model by removing the disc since it was not considered necessary for the analysis. This modified model is used for Section 5.2.

5.2 Stress Initialisation by Implicit and Explicit Solvers

This is an alternative approach to using the *CONTROL_DYNAMIC_RELAXATION card for applying the centrifugal force. In this approach, the centrifugal force is first applied in an implicit prestress static solution followed by blade rotation in an explicit transient solution. During the implicit analysis, all the root nodes of the blades are fixed in space, and a velocity is assigned to each node of the blade according to a linear function starting from 0 to 890 rad/*s*.

When the analysis is completed, a *dynain* file is generated which contains stress distribution in the blades due to the application of the angular velocity. This file is used as input in the transient dynamic analysis of the blade rotation and fan case impact event using an explicit algorithm.

The implicit and explicit analyses were applied to both the sensitivity model and the real compressor blade. The results from the sensitivity model helped

validate the parameters to be used for the compressor blade. The results from the actual blade are discussed in this section.

5.2.1 Implicit Prestress Static Solution

In order to prevent rigid body motion, the blade is constrained from movement in all degrees of freedom at the root. Angular velocity is then ramped up linearly as shown in Fig. 5.5.

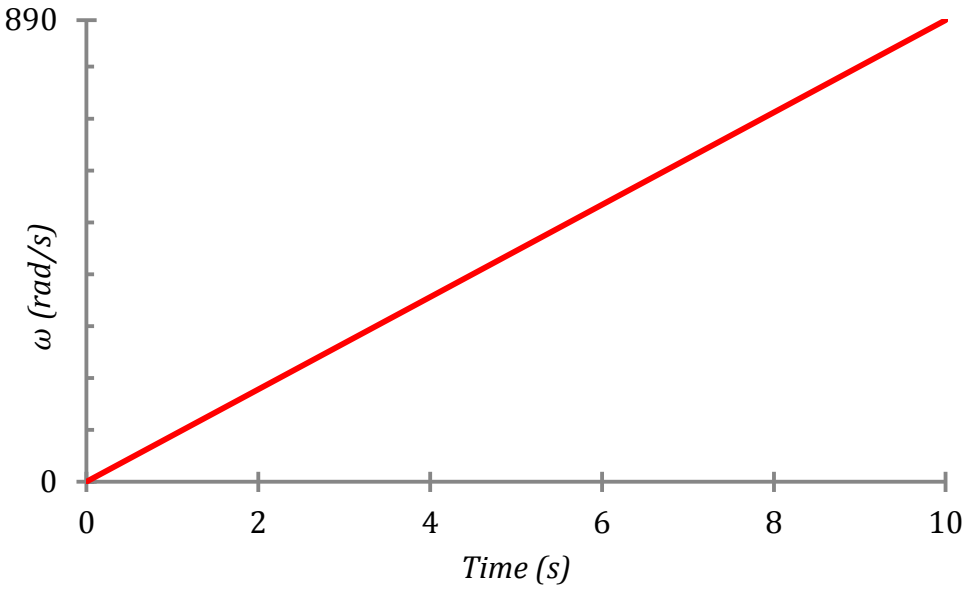

Fig. 5.5 – Load curve for implicit solution

The *LOAD_BODY_OPTION card is used to define the body force load due to rotation specified by the *DEFINE_CURVE card. The blade is made to rotate about the x-axis and the analysis is set to terminate after ten seconds. Implicit analysis is defined by using the *CONTROL_IMPLICIT_GENERAL card and setting the parameter IMFLAG = 1.

The *dynain* file contains the blade deformed geometry and the stress state at the end of the analysis. This is used to input the stressed elements of the blade (Fig. 5.6) for the explicit transient rotation state.

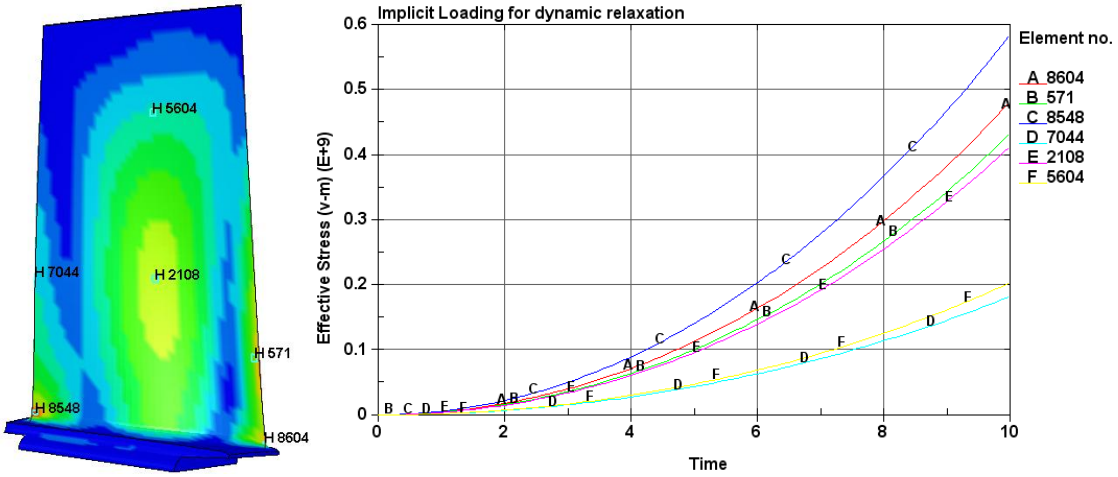

Fig. 5.6 – Effective von Mises stress states after implicit analysis [Units: time (s), stress (Pa)]

After the implicit analysis, there is a reduction in the amount of twist in the blade (Fig. 5.7b). This "straightening" of the blade can be attributed to the centrifugal force acting radially along the blade length. The result is that since there is a drop in the blade twist, there will be a reduction in the stiffness of the blade. This is most likely to reduce the resonant frequencies of the prestressed blade; this will be further looked into in Chapter 6.

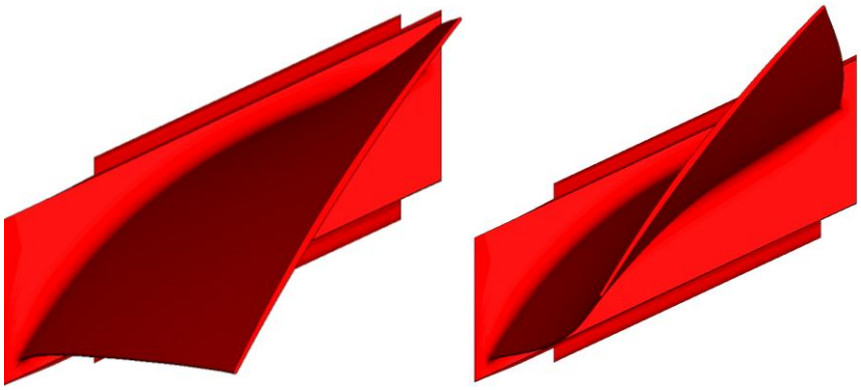

(a) *(b)*

Fig. 5.7 – Blade shape (a) before and (b) after implicit analysis

5.2.2 Explicit Transient Rotation

The *dynain* file generated from the implicit analysis is used as the input for this stage. The *INITIAL_VELOCITY_GENERATION is used to apply the nodal

velocities for rotation. The termination time on the *CONTROL_TERMINATION input is defined to correspond to one revolution of the blade.

$$\text{Termination time} = \frac{2\pi}{890} = 7.06 \text{ ms} \tag{5.4}$$

In order to understand the effect of blade root constraints, comparison of transient analysis has been carried out on two different boundary conditions of the blade. In one, no constraints are applied on the blade; in the second one, the blade root which would be attached to the disc is constrained from translation degrees of freedom. The results from these two different models are shown in Figs. 5.8 and 5.9. The results show that the root constraints increase the maximum stress by 200 MPa.

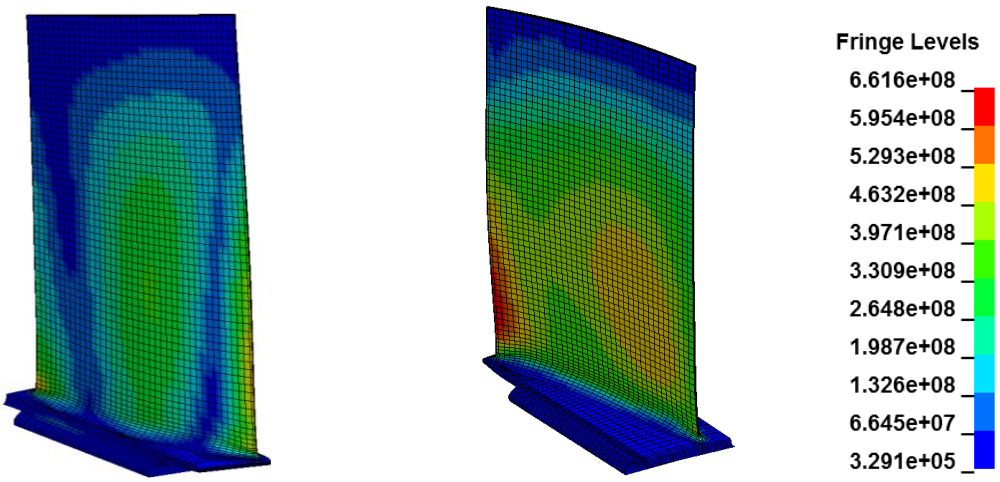

Fig. 5.8 – Von Mises stress distribution in blade after transient analysis [Units: Pa]; constraining forces on blade root are not taken into account

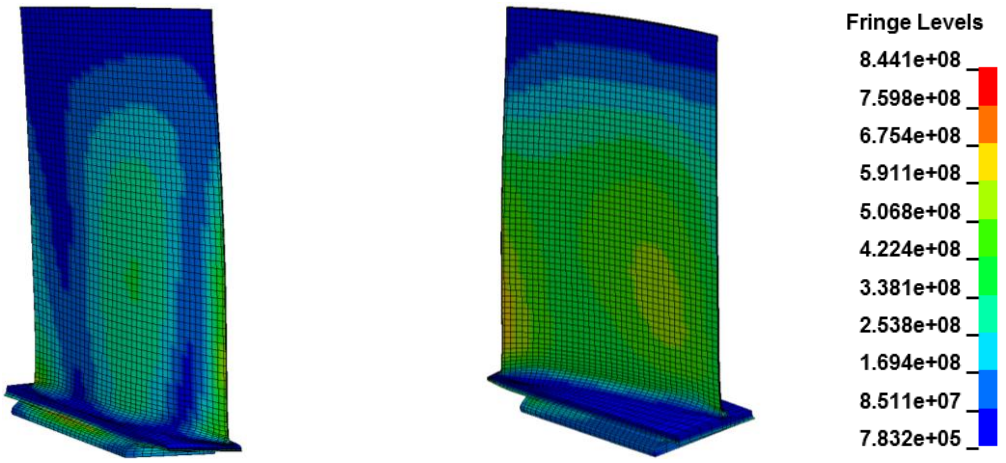

Fig. 5.9 – Von Mises stress distribution in blade after transient analysis [Units: Pa]; constraining forces on blade root are taken into account

Notice that at t = 0, there are virtually no stresses on the blade root but at t > 0, the constraints at the blade root are taken into account. This results in a sudden increase in acceleration. The reason for this is not known. The effect of this sudden onset of constraint on analysis results is little because dynamic relaxation of the blade is allowed to complete before the tip-rubbing event occurs (see Chapter 7).

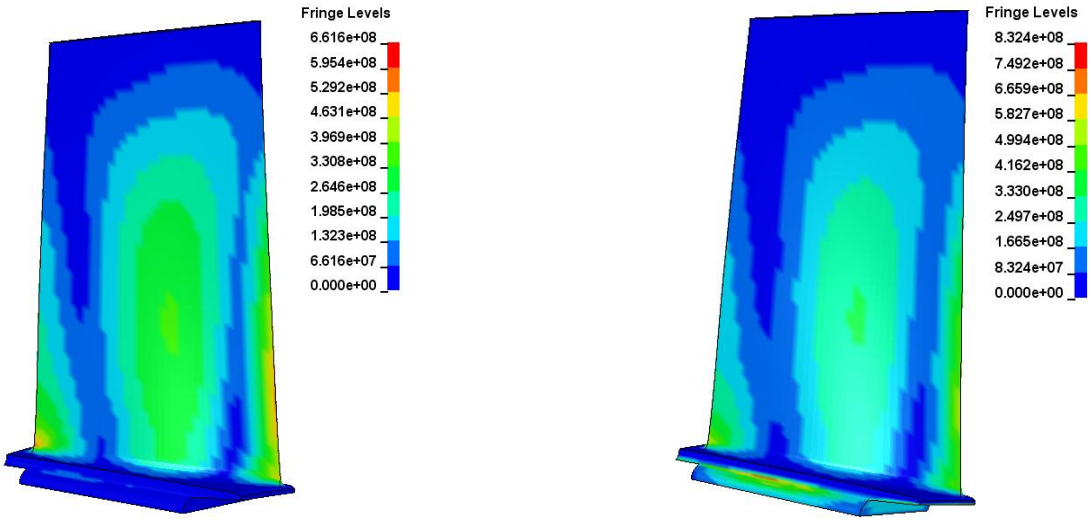

(a) *(b)*

Fig. 5.10 – Application of root constraints at (a) t = 0 s (b) t > 0 s; Von Mises stress shown on fringe levels [Units: Pa]

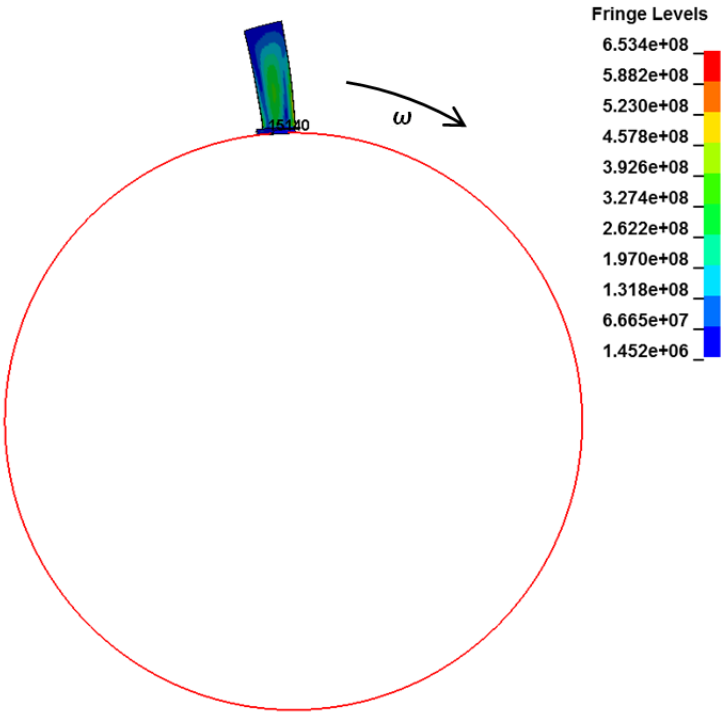

Fig. 5.11 – Rotating blade after transient analysis; red line traces path of rotation. Von Mises stress shown on fringe levels [Units: Pa]

5.2.3 Stable Solution Verification

There are two conditions that are checked against to verify if the transient solution has converged. The first condition is that the centrifugal stresses should be constant by the end of the analysis. To check for a stable solution, centrifugal stresses of selected elements on the blade are plotted (Fig. 5.12). It is seen that the centrifugal stresses have reached a constant value at the end of the transient analysis; therefore, the solution is assumed to have converged.

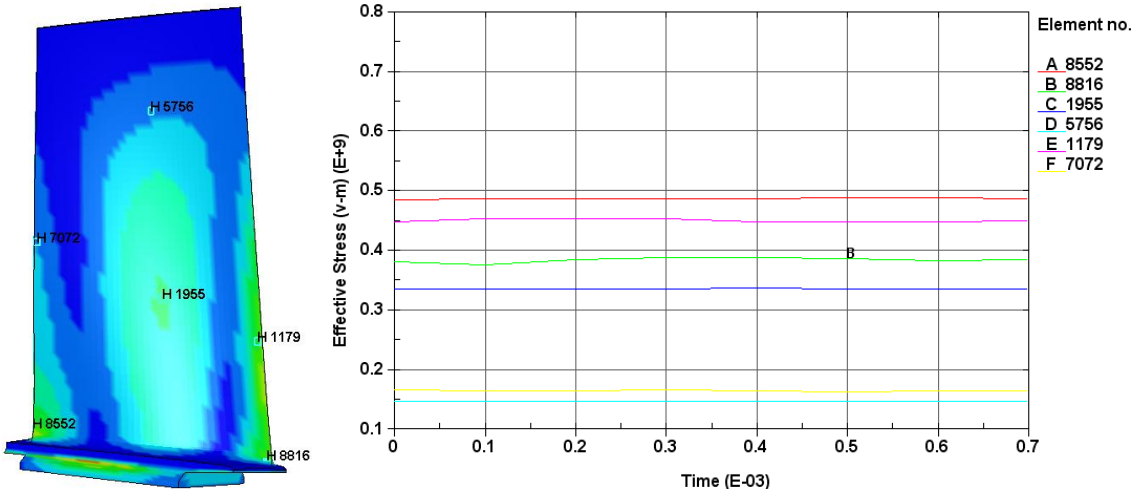

Fig. 5.12 – Von Mises stresses in elements after transient analysis [Units: stress (Pa), time (s)]

It has been specified by Rolls-Royce that the maximum incursion of the blade into the casing is 10 μm. Therefore, the second condition from the transient analysis simulation is that the axial displacement of the blade tip from the axis of rotation does not exceed 10 μm or it will interfere with the results of the tip-rubbing analysis. The displacement of the blade from the axis of rotation (node 18707) to a selected node on the blade tip is plotted in Fig. 5.13.

From Fig. 5.13, it can be seen that the maximum displacement the blade experiences from the axis of rotation does not exceed 0.09 μm. Also, Fig. 5.14 shows that the tip of the blade does not experience excessive vibration after the transient analysis; the maximum displacement seen is 0.25 μm.

Therefore, it can be concluded that centrifugal forces on the blade have converged at the end of the transient analysis.

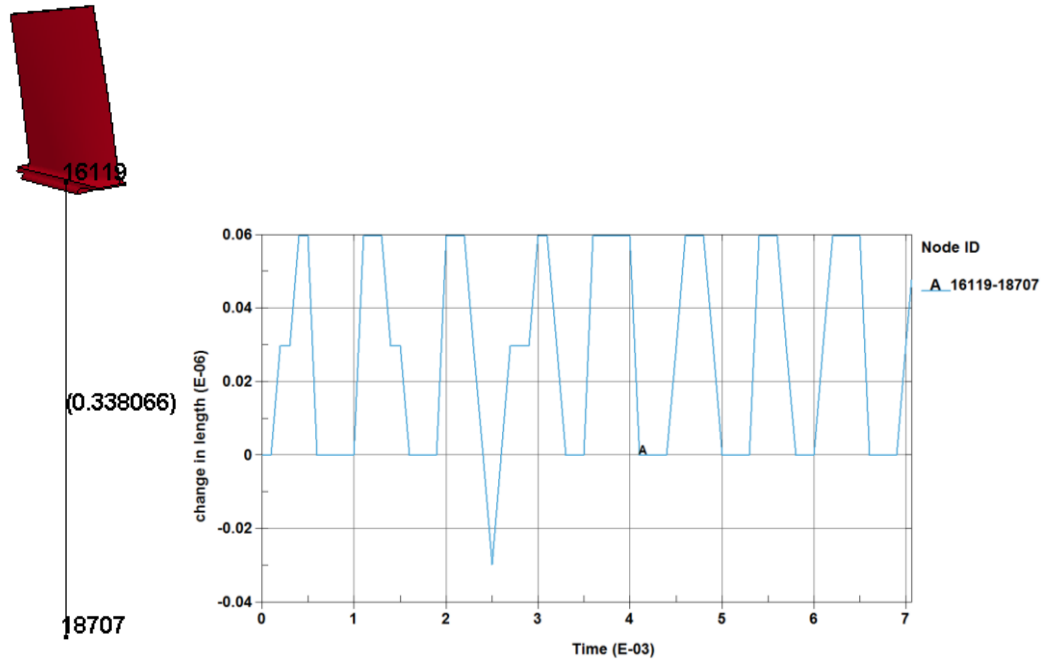

Fig. 5.13 – Axial displacement of blade base (Node 16119) from axis of rotation (Node 18707) during transient analysis [Units: length (m), time (s)]

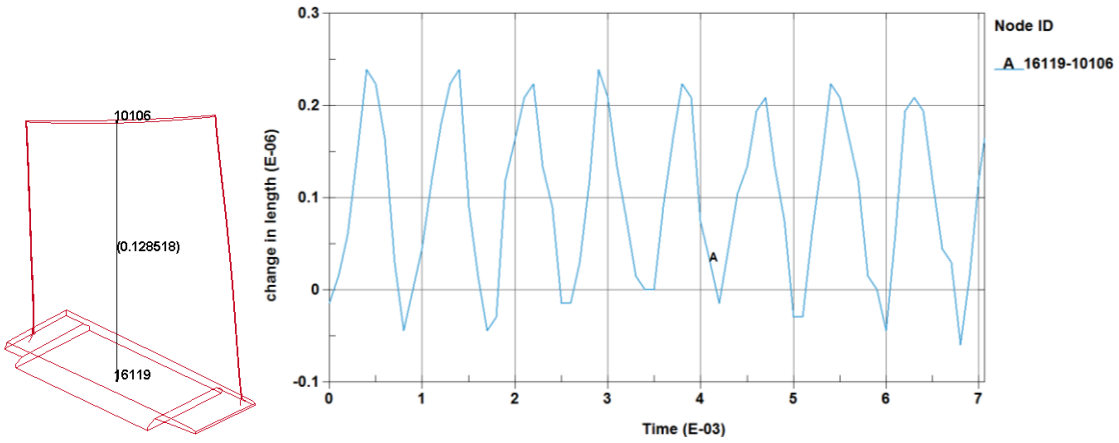

Fig. 5.14 – Axial displacement of blade tip (Node 10106) from blade base (Node 16119) during transient analysis [Units: length (m), time (s)]

Chapter 6 – Modal Analysis of Compressor Blade

In real life, many structures are subject to excessive oscillatory motion as a result of resonance. Resonance is mainly caused by an interaction between the inertial and elastic properties of the materials within a structure. In order to understand vibration-related problems, it is important to identify and quantify resonant frequencies. Modal analysis is widely used to determine the natural frequencies and mode shapes of a structure.

In FEA, modal analysis of structures is often simulated without taking into account the effect of preload conditions. This approach generally works quite well for structures with a high stiffness. However, it is expected that prestress on a structure, such as centrifugal stress on the compressor blade due to rotation, can have a noticeable impact on the resonant frequencies. This is because the stress state alters the stiffness matrix of the blade which in turn affects the resonant frequencies.

Modal analysis on the blade has been conducted taking into account the constraining effect of the disc at the blade root (Fig. 6.1). The constraints are applied in all translational degrees of freedom.

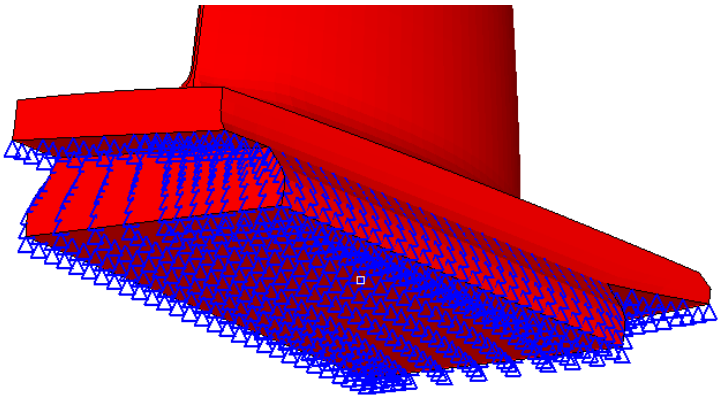

Fig. 6.1 – Blade root constrained in translational degrees of freedom

In this chapter, two different stress states are analysed:

(i) Unstressed modal analysis – stresses on the blade are not taken into account. This is carried out using LS-DYNA and ANSYS. In the unstressed state, the effect of different element formulations on modal frequencies is studied.
(ii) Prestressed modal analysis – this analysis takes into account the centrifugal forces due to rotation (see Chapter 5). This is carried out using LS-DYNA.

It should be noted that apart from centrifugal forces there are other types of loads acting on the blade, such as preloads due to temperature. However, this is not within the scope of this thesis and is therefore ignored. Only the centrifugal force is taken into account.

6.1 Unstressed Modal Analysis and Comparison of Different Element Formulations

LS-DYNA offers two main types of element formulations for solid elements – reduced-integrated and fully-integrated. Each have their own advantages and disadvantages. Reduced-integrated elements have one integration point at the centre of the element as shown in Fig. 6.1(a). They are computationally fast but prone to hourglassing errors. This type of element formulation is recommended for explicit analysis. On the other hand, fully-integrated elements (Fig. 6.1(b)) avoid potential hourglassing modes but are computationally four times slower and tend to shear lock when poor aspect ratios, such as in the current model of the blade, are present.

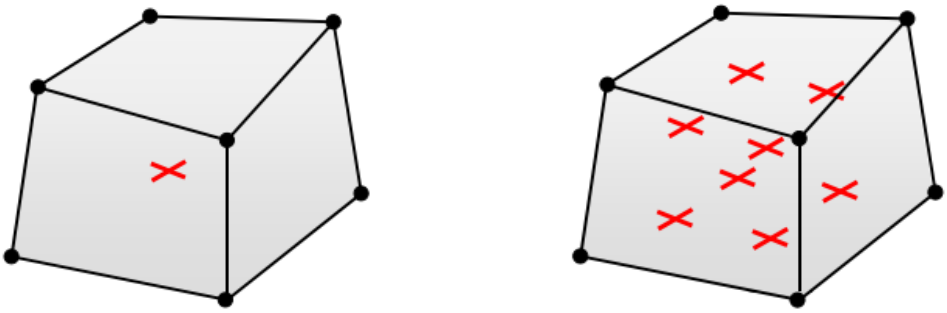

(a) *(b)*

Fig. 6.2 – Solid element formulations in LS-DYNA (a) Reduced-integrated (b) Fully-integrated [31]

Element formulations for solid elements are defined using the *SECTION_SOLID card. Initially, Type 2 element formulation was used since it solves fast. However, there are certain drawbacks to using Type 2 which will be described later. The element formulations studied in LS-DYNA are types 1, 2 and 18. Type 1 is a reduced-integrated constant stress solid element. Type 2 is a fully-integrated selective reduced solid element. Type 18 is a eight-point enhanced strain solid suitable for linear statics and hence is used for the modal analysis only [6]. Therefore, during tip-rubbing analysis, the blade element type is changed to Type 1.

The *CONTROL_IMPLICIT_EIGENVALUE card was used to calculate the first fifteen resonant frequencies in LS-DYNA. The results are shown in Table 6.1.

Table 6.1 – Resonant frequencies for different element formulations in LS-DYNA

Mode	Frequency (Hz)		
	Type 1	Type 2	Type 18
1	355	361	368
2	1066	1157	1110
3	1340	1422	1375
4	2198	2381	2300
5	2771	3128	2855
6	3206	3387	3349
7	3293	3813	3663
8	3796	4186	4219
9	4636	5529	4792
10	5274	5928	5449
11	5466	6253	5590
12	6217	7739	6315
13	6711	7863	6952
14	7132	8338	7336
15	7416	8393	7581

It can be seen from Table 6.1 that using Type 2 element formulation results in much higher resonant frequencies compared to Types 1 and 18. This is most likely due to shear locking in the elements due to poor aspect ratios. As a general rule of thumb, aspect ratios below 5.0 are acceptable for solid elements and not prone to shear locking. However, 40 % of the aspect ratios of the blade elements have been found to be greater than this acceptable parameter (Fig. 6.3).

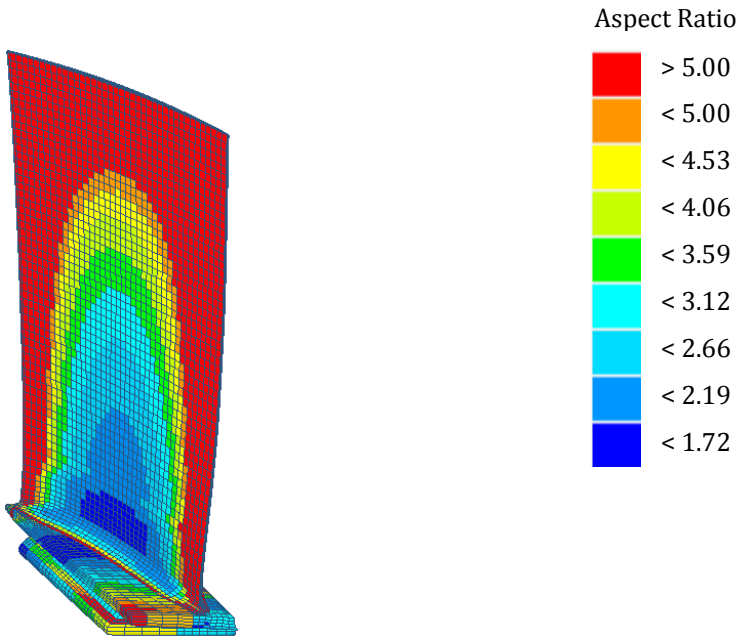

Fig. 6.3 – Aspect ratios of blade elements

Shear locking is an error that is caused by bending modes in fully-integrated elements with poor aspect ratios. This is better explained by understanding how fully-integrated elements work during bending. When bending deformation takes place, the top and bottom edges of fully-integrated elements remain straight and the right angles are not preserved (Fig. 6.4(b)). A parasitic shear stress is introduced to oppose the bending modes. This shear stress causes the element to appear stiffer than it actually is; consequently, displacements are much lower than they should be and the resonant frequencies determined from the simulation are higher than their actual value.

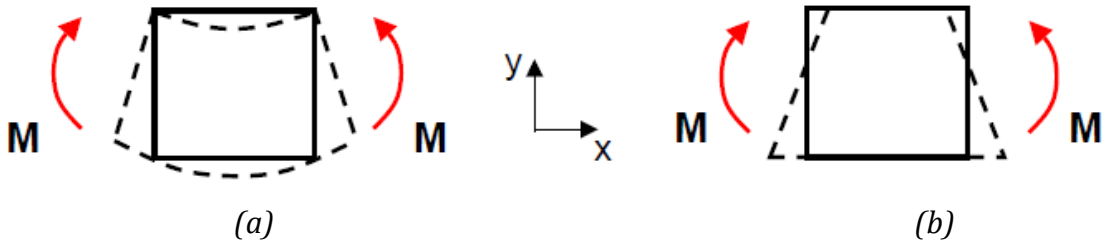

Fig. 6.4 – (a) pure bending deformation – no shear locking (b) shear locking error [31]

There are two possible ways in which shear locking can be alleviated. The first is to use one point solid element formulations such as Type 1. Alternatively, LS-DYNA recommends using enhanced strain formulations such as Type 18 for poor aspect ratios. In the latest version of LS-DYNA, a new type of fully-integrated element formulation is available which is suited to modelling poor aspect ratios [31]; this is reported to eliminate both shear locking and hourglass errors. This could be incorporated into future studies.

Modal analysis was conducted in ANSYS used the SOLID 185 element formulation with enhanced strain. SOLID 185 element is defined by eight nodes having three degrees of freedom at each node. The results for this are shown in Table 6.2; results from modal analysis of Type 18 elements in LS-DYNA are presented alongside for comparison. Some minor variations between LS-DYNA and ANSYS codes should be expected as the element formulations are slightly different in the two solvers [26].

Table 6.2 – Comparison of resonant frequencies between ANSYS and LS-DYNA

Mode	Frequency (Hz)		Difference (%)
	LS-DYNA Type 18 (enhanced strain)	ANSYS SOLID 185 (enhanced strain)	
1	368	361	-1.78
2	1110	1090	-1.84
3	1375	1368	-0.52
4	2300	2254	-1.99
5	2855	2839	-0.53
6	3349	3261	-2.63
7	3663	3361	-8.24
8	4219	3889	-7.83
9	4792	4775	-0.36
10	5449	5445	-0.07
11	5590	5615	0.45
12	6315	6352	0.58
13	6952	6956	0.06
14	7336	7378	0.57
15	7581	7616	0.45

6.2 Prestressed Modal Analysis

Centrifugal forces are expected to have an effect on blade resonant frequencies. The deformation of any rotating object under dynamic loads is influenced by the inertial forces they experience due to the rotation. This leads to a phenomenon called centrifugal stiffening where the natural frequencies may significantly increase with rotor speed. This is an important factor in the design of high-speed compressors and turbines, since the changing natural frequencies can give rise to unexpected resonances.

The natural frequency of vibration of a beam is almost always increased by the presence of blade pre-twist. Recalling from Section 5.2.1, it can be seen that the compressor blade pre-twist decreases slightly due to this additional stress. The result is that since there is a drop in the blade twist, there will be a reduction in the stiffness of the blade. The effect of this reduction in stiffness will be studied a little later in this section.

Prestressed modal analysis was conducted in LS-DYNA using Type 18 element formulation. The results are presented in Table 6.3; resonant frequencies of the unstressed blade are also included for comparison. The mode shapes for the unstressed and prestressed blade are also described.

Table 6.3 – Comparison of resonant frequencies for unstressed and prestressed blade using LS-DYNA

Mode	Unstressed		Prestressed		% Difference
	F (HZ)	Description	F (Hz)	Description	
1	368	Fundamental (1F)	382	Fundamental (1F)	3.85
2	1110	First torsional (1T)	1065	First torsional (1T)	-4.08
3	1375	First combined flexural-torsional (1C)	1371	First combined flexural-torsional (1C)	-0.28
4	2300	Second torsional (2T)	2216	Second torsional (2T)	-3.64
5	2855	Second flexural (2F)	2918	Second flexural (2F)	2.21
6	3349	Tramline mode	3316	Tramline mode	-0.99
7	3663	Third torsional (3T)	3669	Third torsional (3T)	0.15
8	4219	Similar to Mode 7	3946	First edgewise (1E)	-6.48
9	4792	Third flexural (3F)	4912	Third flexural (3F)	2.50
10	5449	Fourth torsional (4T)	5331	Fourth torsional (4T)	-2.16
11	5590	Second combined flexural-torsional (2C)	5548	Second combined flexural-torsional (2C)	-0.75
12	6315	Third combined flexural-torsional (3C)	6345	Third combined flexural-torsional (3C)	0.47
13	6952	Fourth flexural (4F)	6989	Fourth flexural (4F)	0.54
14	7336	Fourth combined flexural-torsional (4C)	7225	Fourth combined flexural-torsional (4C)	-1.52
15	7581	Fifth combined flexural-torsional (5C)	7538	Fifth combined flexural-torsional (5C)	-0.58

Comparisons of blade resonant frequencies show that there is an increase in flexural resonant frequencies and a decrease in the torsional frequencies for the prestressed blade. This agrees with the theory that an increase in blade pre-twist results in a higher blade stiffness; by the same token, since centrifugal forces on the blade have resulted in a loss in blade pre-twist, the torsional stiffness of the blade has decreased and therefore resonant frequencies are expected to decrease in the torsional modes. Resonant frequencies are expected to increase in the flexural modes due to centrifugal force acting radially outward from the blade. This increases the blade bending stiffness.

Mode shapes for the unstressed and prestressed blades are shown in Fig. 6.6 and Fig. 6.7 respectively. Two mode shapes are presented per mode to capture the maximum and minimum vibration of the blade at the selected resonant frequency. The terms used to explain the mode shapes are described shown in Fig. 6.5; nodes on the figures are points of zero displacement.

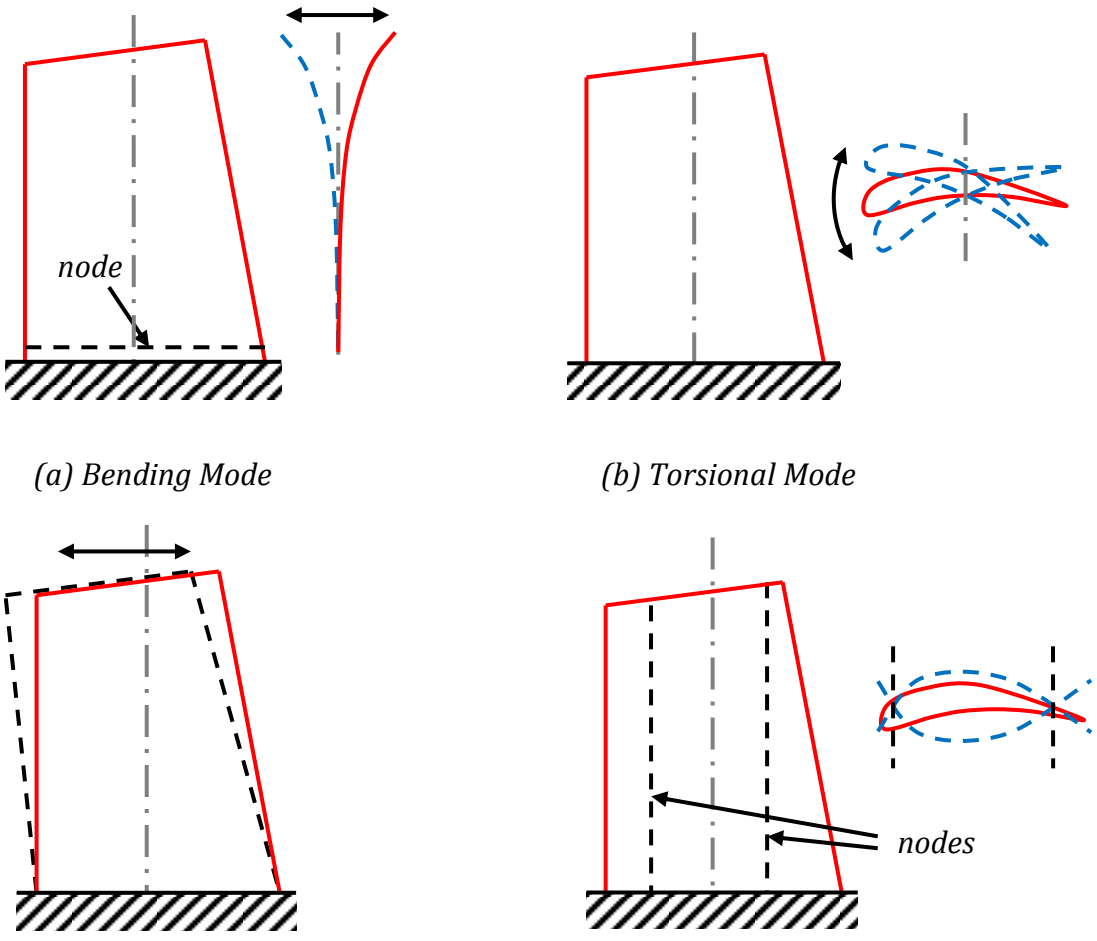

(a) Bending Mode

(b) Torsional Mode

(c) Edgewise Mode

(d) Tramline Mode

Fig. 6.5 – Modes of vibration

On comparing the mode shapes of the unstressed and prestressed blade, it can be seen that the mode shapes are identical for all modes except for Mode 8 (4219 Hz). At this mode, the unstressed blade shows a mode shape identical to Mode 7. At Mode 8, the prestressed blade shows an edgewise mode. An edgewise mode of vibration is where the blade vibrates from leading edge to trailing edge and vice versa (Fig. 6.5(c)).

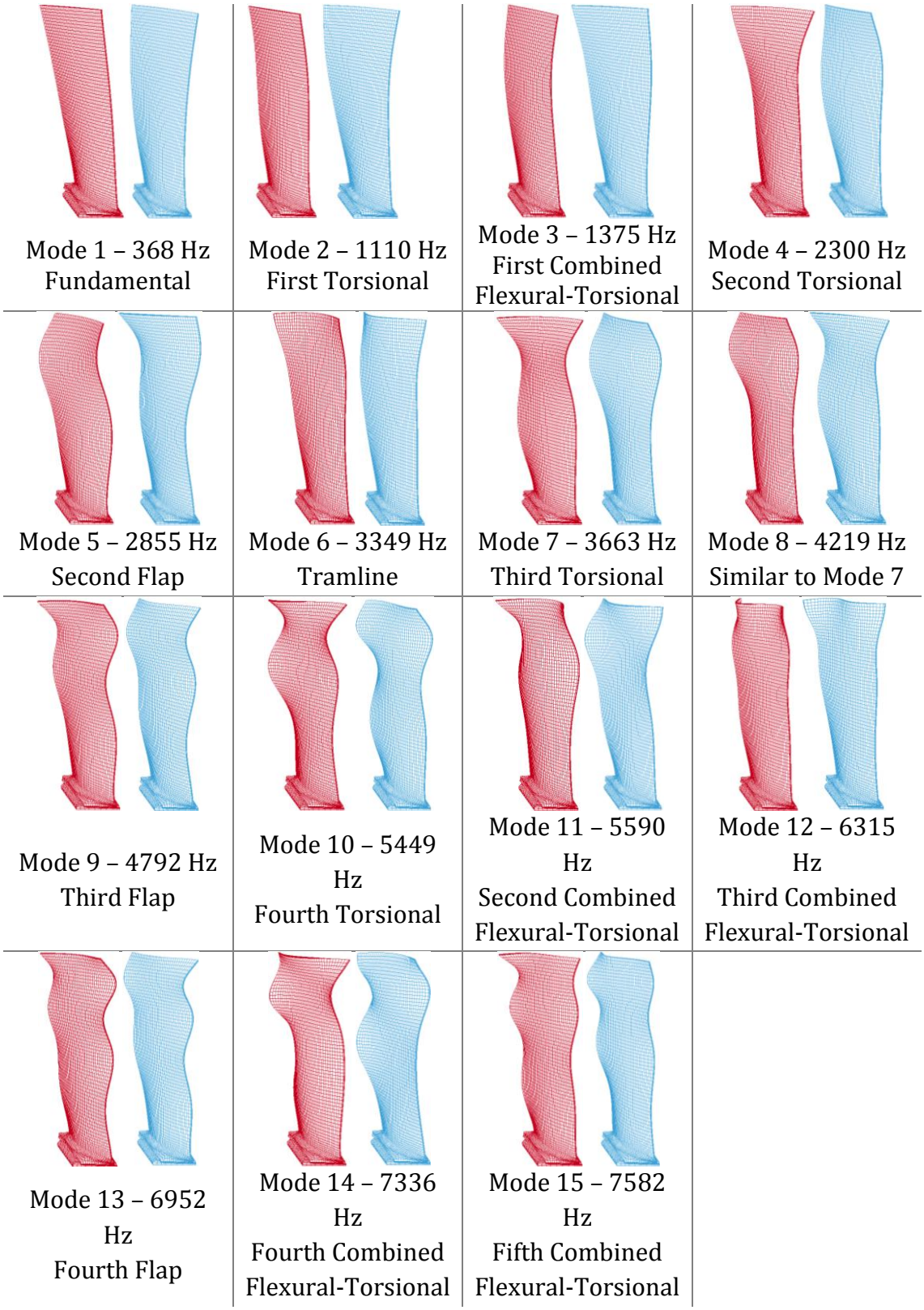

Fig. 6.6 – Mode shapes of unstressed compressor blade

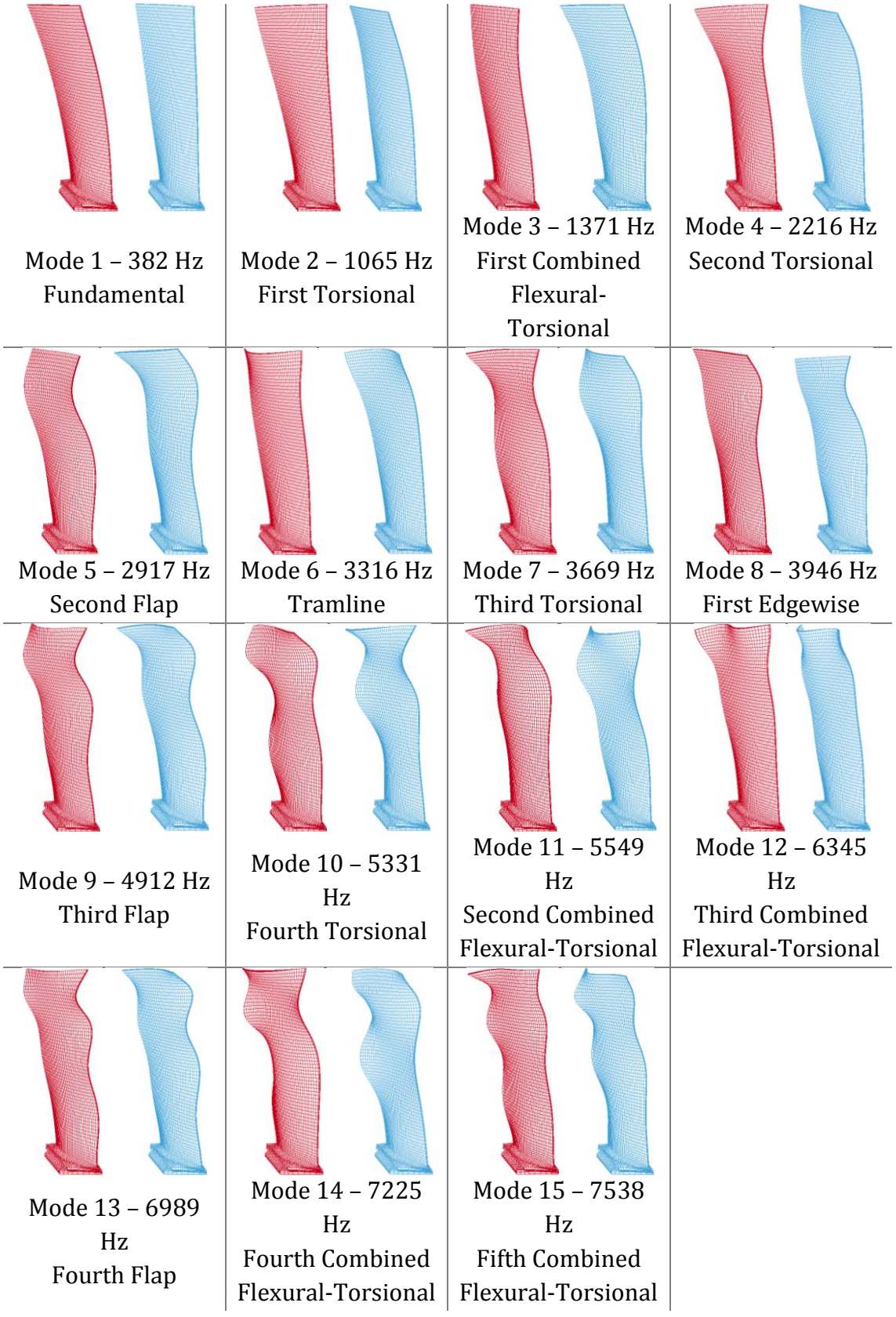

Fig. 6.7 – Mode shapes of prestressed compressor blade

6.3 Campbell Diagram

Campbell diagrams are used to illustrate the interference between natural frequencies and common exciting forces. In a turbofan, the most common sources of excitation are running speed harmonics (also known as engine orders) and blade passing frequencies. Running speed harmonics are multiple frequencies of the rotor operating speed. For example, the compressor rotor running at 8500 RPM (141.64 cycles/sec or Hz) would be having running speed harmonics occurring at 283.28 Hz, 424.92 Hz, 566.56 Hz, and so on. The blade passing frequency is discussed in detail in Section 6.4.

In a Campbell diagram, the natural frequencies of the system are plotted against engine speed. If the blade natural frequency crosses an engine order during engine operation resonance can be triggered in the system. The Campbell diagram is of importance to this project because it highlights key resonances which can be triggered during operation; the vibration of the blade at these resonances during engine operation could contribute to tip-rubbing. Also, if these resonances occur in the blade during tip-rubbing, they are likely to be aggravated by the engine orders and the amplitude of vibration could grow to destructive levels in a very short period of time.

Engine orders for the Trent 900 IP compressor have been calculated for this project for speeds between 0 rpm and 10,000 rpm; the values are given in Appendix G. Fig. 6.8 shows the Campbell diagram for the IP compressor. The first three resonant frequencies determined from prestressed modal analysis are plotted. It should be noted that during actual engine operation, the resonant frequencies can decrease by as much as 15% due to thermal effects. During engine acceleration and deceleration these modes would get excited but the time spent at resonance is key. If resonance is excited during engine acceleration or deceleration then it has a small effect and does not pose any concern but if there is a long time to be spent at a specific speed like cruising of aircraft then care must be taken to avoid resonance at long dwells.

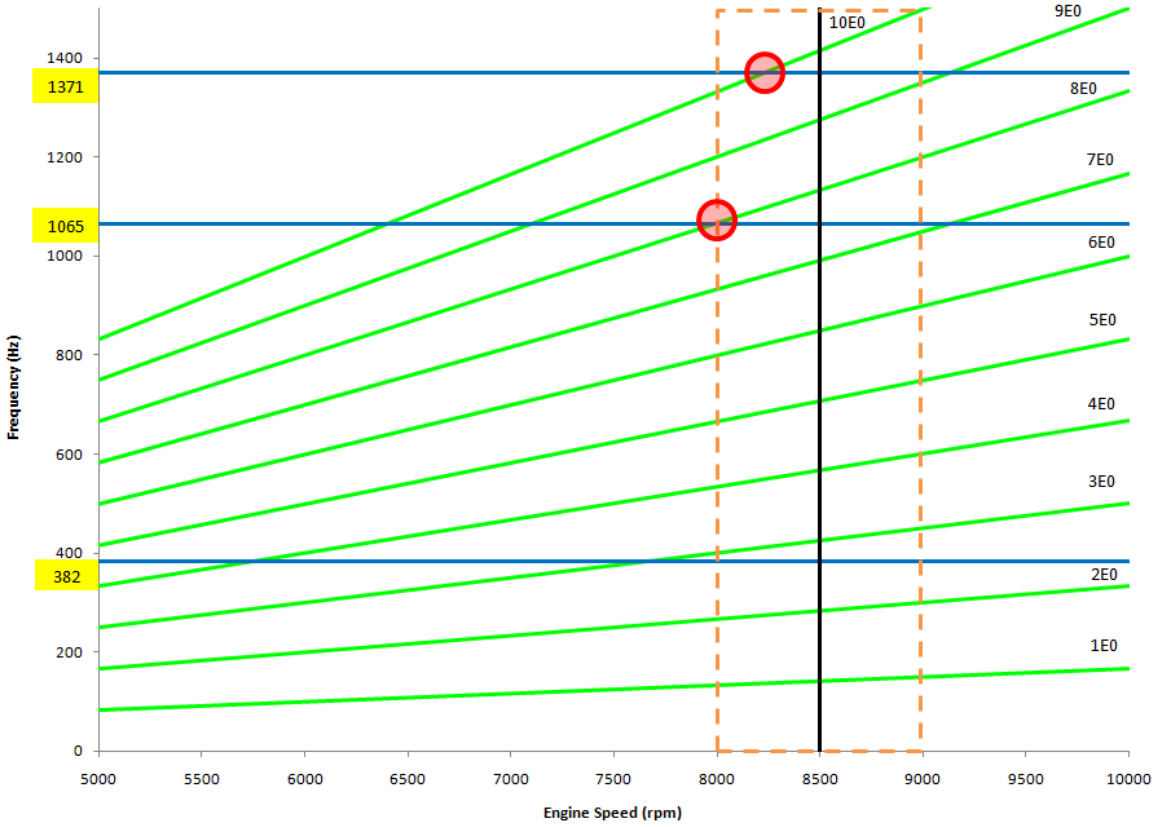

Fig. 6.8 – Campbell diagram of IP compressor

As stated previously, the first three resonances of the prestressed blade are plotted against the engine orders in the Campbell diagram (Fig. 6.8). Also, engine speeds in the range of 8000 – 9000 rpm have been considered. From the Campbell diagram, it can be seen that the fundamental flexural mode (1F) does not cross any engine orders during operation; however, resonance can be triggered in the first torsional (1T) and first combined flexural-torsional (1C) modes by the eighth and ninth engine order respectively.

6.4 Blade Passing Frequency

The calculation of the BPF (Blade Passing Frequency) of the compressor is of importance since it is another frequency of excitation which should be avoided during tip-casing interactions. The BPF (Blade Passing Frequency) of the

compressor can result in unwanted vibrations if it coincides with any of the resonant frequencies at operating conditions.

It has been estimated that there are 72 blades on a single compressor disc for the IP stage. The BPF is calculated as

$$\text{BPF} = \frac{\omega_{rpm} \times \text{number of blades}}{60} = \frac{8500 \times 72}{60} = 10.2 \text{ kHz} \tag{6.1}$$

Since the BPF is 10.2 kHz, it is much higher than the resonant frequencies and is therefore not expected to pose a problem during engine operation.

6.5 Conclusions

In this chapter, it has been seen that using an incorrect element formulation can lead to erroneous results for resonant frequencies; therefore, one has be very careful in choosing the correct element formulation for a problem to prevent potential shear locking or hourglassing errors.

Modal analysis has been conducted on the unstressed and prestressed blade. It has been seen that the centrifugal force acting on the rotating blade tends to reduce its torsional stiffness due to loss of blade pre-twist, and increase the flexural stiffness. Resonant frequencies which can occur during engine operation have been identified by the Campbell diagram. These show that the first torsional mode (1110 Hz) and first combined flexural-torsional mode (1375 Hz) can be triggered during engine operation.

Although only the blade resonances have been studied in this chapter, it should be noted that the casing resonant frequencies can also be of significance since they can feed unwanted vibrations into the system during tip-rubbing. However, due to lack of data about the actual geometry of the casing, this was not achieved.

Chapter 7 – Analysis of Blade Tip-Rubbing

In this chapter, finite element analysis of the tip-rubbing event is described. The content of this chapter is divided into two main parts. The first part details the finite element model used for the analysis and definition of key input parameters for the blade-to-casing contact. The second part of this chapter contains the results from the analysis. The results provide an understanding into the vibration of the system; these are presented in the form of images and graphs.

7.1 Tip-Rubbing Configuration

Initially, a single-blade-single-casing configuration had been analysed, where tip-rubbing occurred once per revolution. However, Rolls-Royce are more interested in analysing a two-blade-two-casing configuration since this is a more realistic representation of the contact of the blade tip with a casing that had deformed elliptically due to external loading conditions (such as deformation of casing due to heavy landing). The configuration used for the analysis is shown in Fig. 7.1.

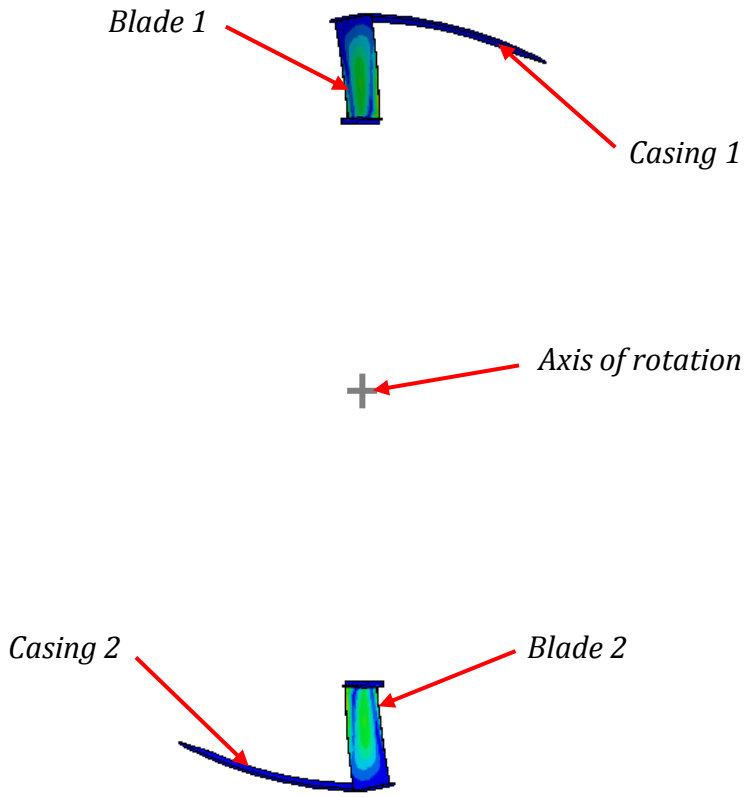

Fig. 7.1 – FEA model of two-blade two-casing configuration

7.2 Parameters for Contact Modelling

In this section, various key parameters used to set up the simulation and output results are discussed. For the complete input file, the reader should refer to Appendix C.

7.2.1 Interface Definition of Blade Tip-Casing Contact

A reasonably accurate simulation of the tip-rubbing event is very important. LS-DYNA offers quite a few contact types appropriate for this type of simulation; *CONTACT_SURFACE_TO_SURFACE is used in this project. This is a two-way treatment of contact which means that both the master and slave surfaces of contact are checked for penetration during the simulation.

Generally in LS-DYNA modelling, the contact between two impacting bodies is defined by an interface set made up of slave and master sides. In any explicit-integration scheme, it is imperative that for proper load transfer between the two

bodies in contact the slave side mesh is finer than the master side mesh. For this simulation, the blade is taken as the slave side while the casing is defined as the master side.

The penalty method of contact is used for simulation of the tip-rubbing event. In penalty methods, contact treatment is generally represented by linear compressive springs between the slave and master nodes. Penalty contacts tend to be quite stable and do not excite hourglassing in the mesh of the contacting parts. There are three types of penalty contact implementation available in LS-DYNA:

(i) Standard penalty formulation
(ii) Soft constraint penalty formulation – this is used to model contact between bodies with highly dissimilar material properties, such as metal and foam.
(iii) Segment-based penalty formulation – this type of contact is similar to soft constraint penalty formulation except for segment masses at contact being used as opposed to nodal masses. This method of contact will be considered in this project.

During contact, some level of interpenetration between master and slave segments is expected to occur. Segment-based contacts detect penetration of one segment into another segment and apply penalty forces to the segment nodes. Initial penetrations do not produce any contact forces and are not eliminated when segment-based contacts are used; instead, the location at which initial penetration occurs becomes the baseline from which further penetration is measured. The additional penetration produces the contact forces.

In segment-based contacts, the segment mass is approximately equal to half the element mass at contact [5]. Segments are created on the inner surface of each casing and on the top surface of each blade (Fig. 7.2).

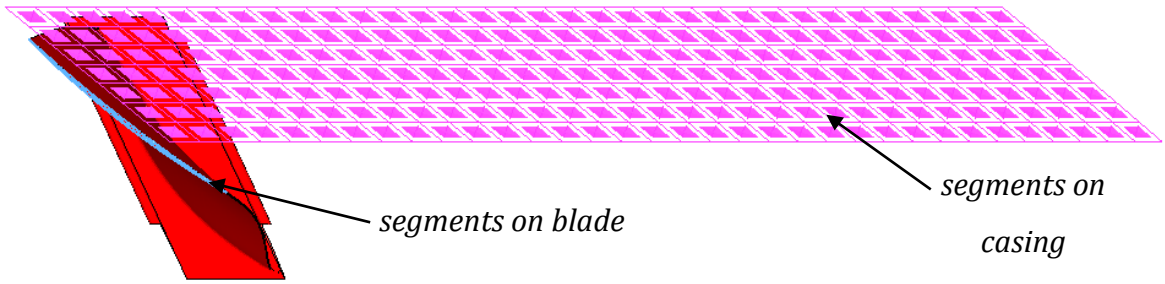

Fig. 7.2 – Segments defined on blade and casing for contact

When two segments of blade and casing come into contact, forces are distributed among the nodes surrounding the segments; this results in a more realistic distribution of contact forces. The contact stiffness k_c is affected by the timestep size Δt_c as shown in equation (7.3).

$$k_c(t) = 0.5\left(\frac{m_1 m_2}{m_1 + m_2}\right)\left(\frac{1}{\Delta t_c(t)}\right)^2 \tag{7.3}$$

Where m_1 and m_2 are masses of the master and slave segments respectively. The timestep size is calculated by

$$\Delta t_c = \frac{V_e}{cA_{max}} \tag{7.4}$$

Where V_e is the element volume, $A_{max}$is the maximum surface area of the element and c is the plane stress sound speed for solid elements. A sample element is chosen from the blade to calculate A_{max}. The timestep is calculated as per the procedure outlined in LS-DYNA Theory Manual [5]; the parameters are shown in Table 7.1.

Table 7.1 – Parameters for determination of timestep

V	2.240E-10
A_{max}	2.935E-06
L_e	7.631E-05
G	4.240E+10
C_0	1.5
C_1	0.06
CN	7.488E+10
CD	1.879E+03
C	6313.39
Q	3.788E+02
Δt_c	1.138E-08

The initial penetration between Blade 2 and Casing 1 (Fig. 7.3) has been measured at t = 0.0038 s; this shows depth of the initial penetration to be approximately equal to 0.3 μm. This level is considered to be acceptable since it is 3% of the blade-casing incursion level of 10 μm. Therefore, actual blade-casing incursion is 9.7 μm.

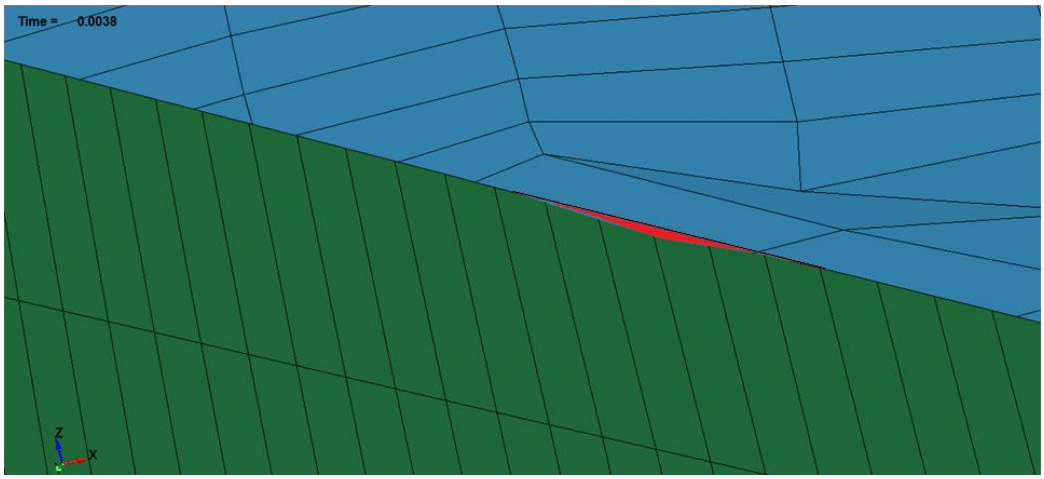

Fig. 7.3 – Initial penetration (shown by red area) between Blade 2 (green elements) and Casing 1(blue elements)

7.2.2 Friction and Damping Parameters

Friction in LS-DYNA is calculated by a Coulomb friction formulation. Frictional parameters in the *CONTACT_SURFACE_TO_SURFACE card is defined by Card 2. The transition from static to dynamic friction is described by an exponential interpolation as shown in equation (7.1).

$$\mu_c = \mu_d + (\mu_s - \mu_d)e^{-DC\cdot|v_{rel}|} \tag{7.1}$$

Where μ_c is the frictional coefficient of contact, μ_s and μ_d are the static and dynamic coefficients of friction respectively, DC is a decay coefficient which determines the manner in which the frictional coefficient of contact is transitioned from μ_s to μ_d, and v_{rel} is the relative velocity of the surfaces in contact. For this simulation, $\mu_s = 0.36$, $\mu_d = 0.30$, v_{rel} is calculated as the tangential velocity of the blade (418.656 ms^{-1}). The decay coefficient DC is taken as 1/10,000.

In the *CONTACT_SURFACE_TO_SURFACE card, two other parameters are required to calculate the contact friction. These are:

(i) coefficient of viscous friction VC , which limits the frictional contact stress based on the strength of the materials in contact and is calculated as

$$VC = \frac{\sigma_0}{\sqrt{3}} = 508.07 \tag{7.2}$$

(ii) the viscous damping coefficient VDC; this is implemented in order to damp out oscillations in order to reduce high-frequency oscillation of contact forces.

7.3 Analysis of Results

In this section, the results from the tip-casing interactions are discussed. Throughout the tip-rubbing analysis, data was collected by defining two rotating

local coordinate systems per blade (Fig. 7.4). Contact is started after 0.0035 s in order to ensure that dynamic relaxation has been applied properly to the blade prior to contact. The simulation is run for ten revolutions (0.0706 s).

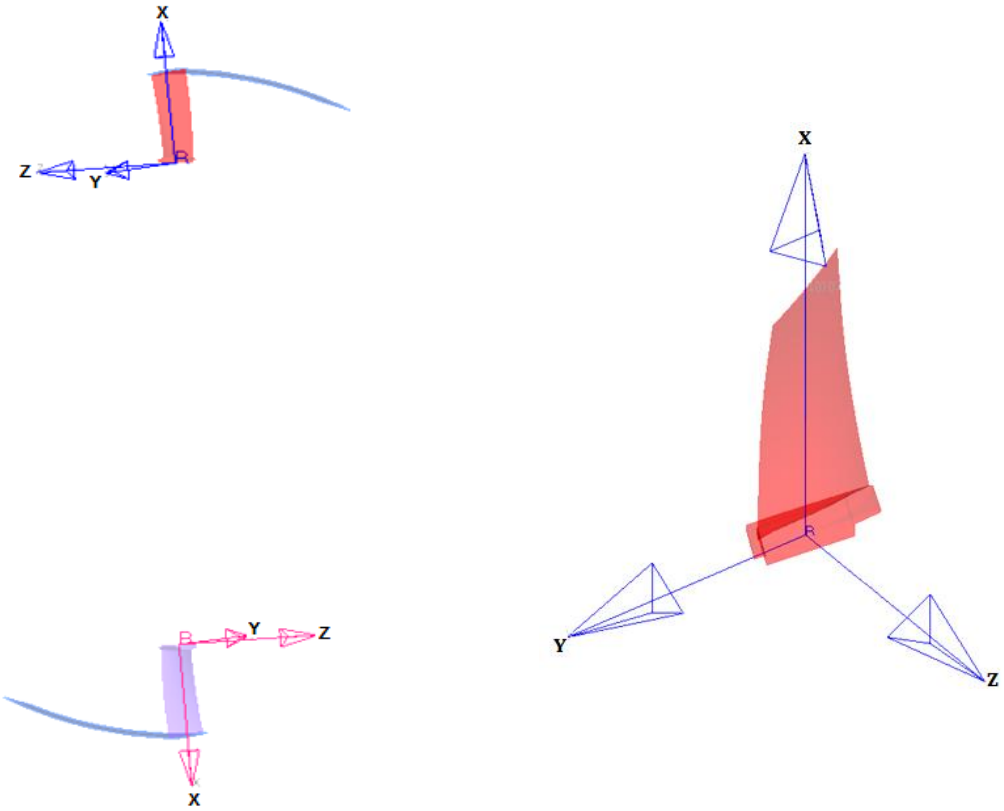

Fig. 7.4 – Rotating local coordinate systems of blades

After the application of dynamic relaxation, inconsistencies were noticed in the stress distributions of Blade 1 and Blade 2 (Fig. 7.5). Although both blades have the same stress distribution pattern, the magnitudes of stress are different. Post dynamic relaxation the maximum stress is 839 MPa for Blade 1 and 1.087 GPa for Blade 2; this gives a difference in stress of 0.248 MPa.

The reason for this inconsistency is not known since the same boundary conditions were applied to both the blades. Blade 2 was created by rotating the implicitly prestressed Blade 1 (see Section 5.2.1) about the axis of rotation. Therefore, the stress state of both the blades at the beginning of the explicit transient analysis should be the same as the stress state of Blade 1 at the end of the implicit analysis. Recall from Section 5.2.2 that during transient analysis maximum

stress in the blade at t = 0 is 662 MPa; this is true for both the blades. However, at the next time plot (t = 0.0001 s) the stress values suddenly increase due to application of constraining forces at the root. It is after this time that inconsistencies in stress distribution are noticed between the two blades.

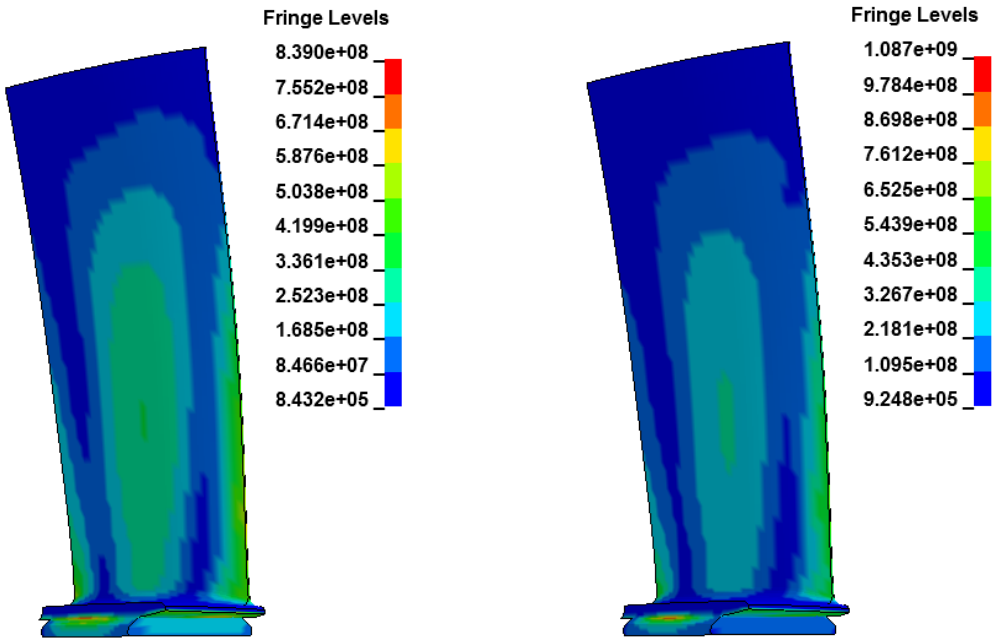

(a) Blade 1 *(b) Blade 2*

Fig. 7.5 – Inconsistencies in von Mises stress distribution in Blade 1 and Blade 2 after dynamic relaxation (t = 0.003 s) [Units: Pa]

The results from the tip-rubbing simulations will be analysed for both the blades since the difference in the stress distributions after dynamic relaxation is not too much. However, any anomalies discovered will be discussed further.

7.3.1 Hourglassing Modes

Before studying the blade response after tip-rubbing, it is important to look at the hourglass energies first. This is because spurious hourglassing modes have been observed in the casing which will most likely have an effect on the tip-rubbing analysis results.

Looking at Fig. 7.6, there are plastic strains on the casing at the end of the analysis. However, this is not considered to be true since the casing has been modelled as elastic. Closer look at the distorted elements shows that the casing appears to have undergone hourglass deformation.

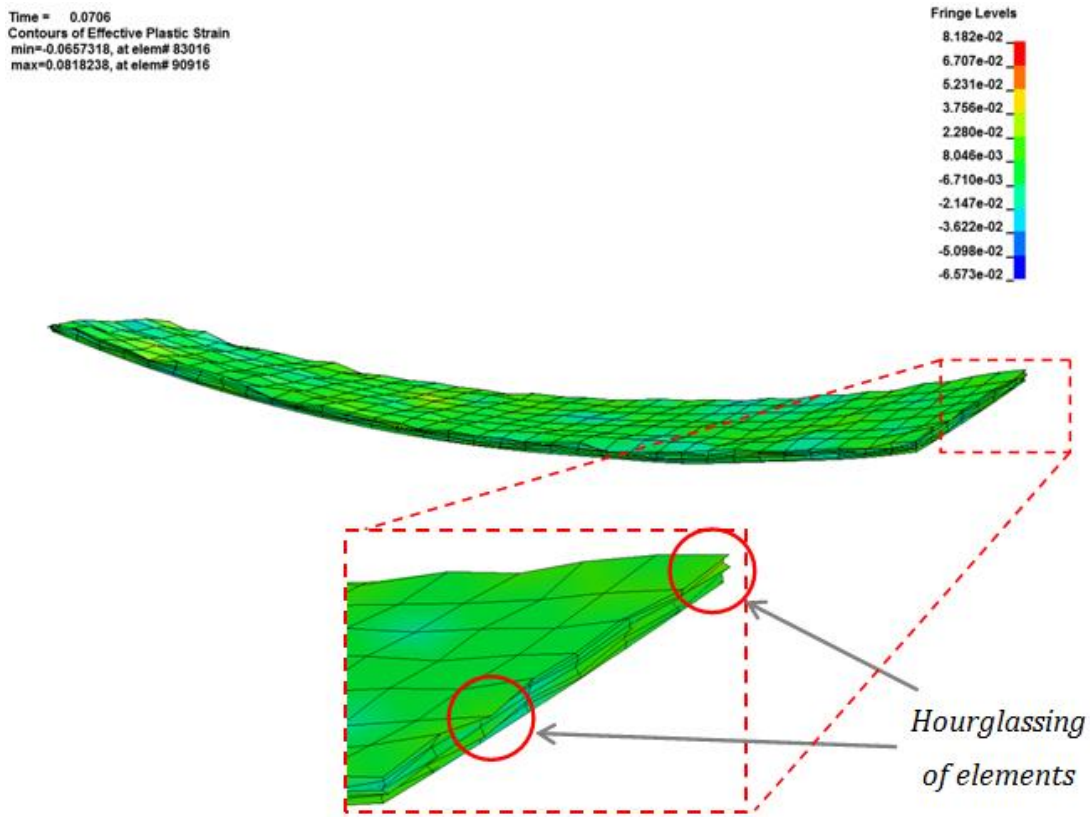

Fig. *7.6 – Plastic strains and hourglassing of Casing 1 after simulation (t = 0.0706 s)*

Prior to running the analysis, care had been taken to avoid hourglassing errors by using the *CONTROL_HOURGLASS card. The purpose of hourglass control is to add stiffness to the system to resist hourglass modes. Element formulation for the blade was initially specified to be Type 18 (see Section 6.1) which is the eight-point enhanced strain element; however, at the start of the tip-rubbing simulation LS-DYNA defaults to Type 1 which is a one-point integrated element; this occurs because Type 18 is suitable for linear statics only [5] and is therefore unsuitable for modelling the tip-rubbing analysis. The element formulation for the casing has been taken to be Type 1. Although Type 1 does not

shear lock for elements with poor aspect ratios, it is known to be prone to hourglass modes.

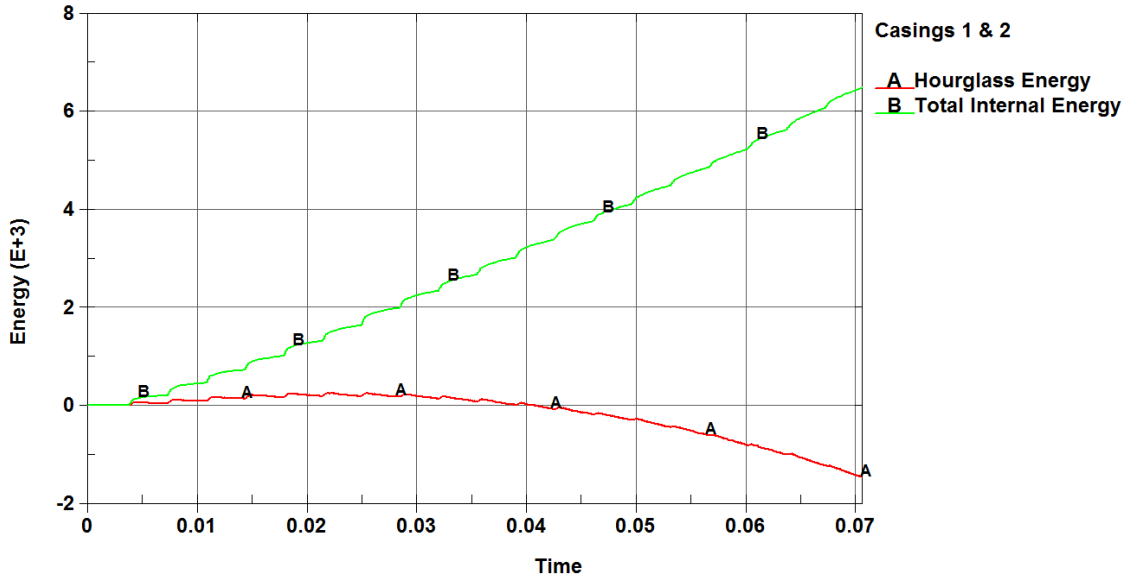

Fig. 7.7 – Hourglass and total internal energies for Casings 1 and 2 [Units: time (s), energy (J)]

Hourglass energy is usually acceptable in a simulation if it is within ±10% of the total energy [1]. From Fig. 7.7, it can be seen that maximum hourglass energy seen in the casing is 20% of the total internal energy. Therefore, hourglassing of the casing has a considerable effect on stress state of the casing, and consequently on the simulation. For the blades, hourglass energy is within 1% of the total internal energy (Fig. 7.8 and Fig. 7.9) and can therefore be considered acceptable.

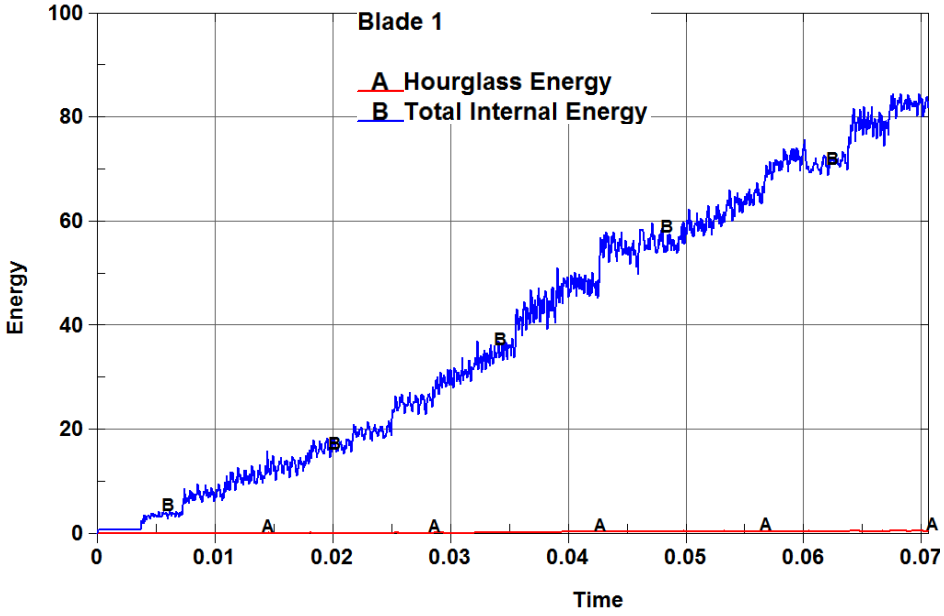

Fig. 7.8 – Hourglass and total internal energy for Blade 1 [Units: time (s), energy (J)]

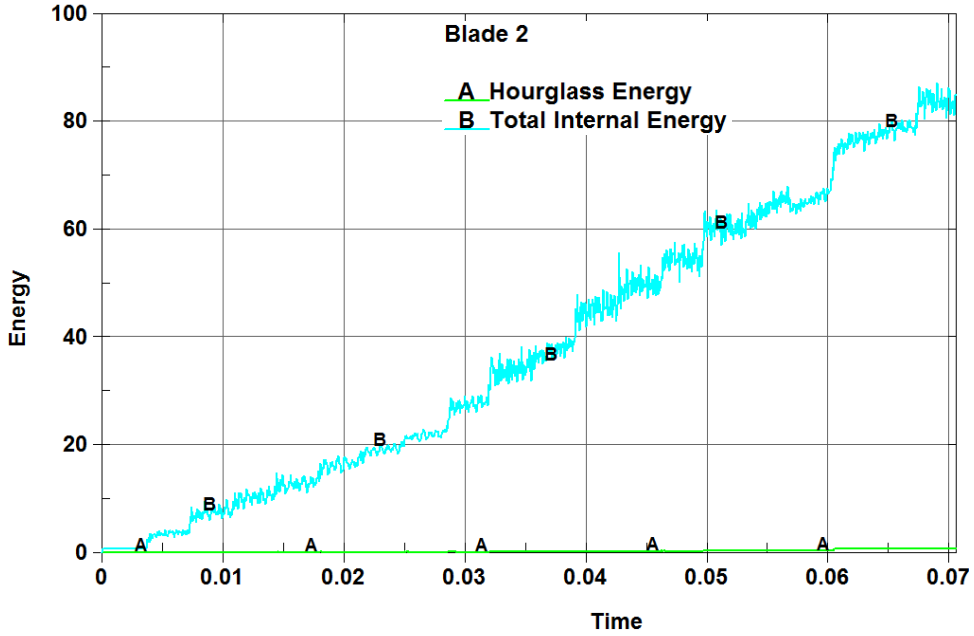

Fig. 7.9 – Hourglass and total internal energy for Blade 2 [Units: time (s), energy (J)]

Frictional energies for Blade 1 and Blade 2 are shown in Fig. 7.10 and Fig. 7.11 respectively; the dotted lines indicate the trend of the frictional energies.

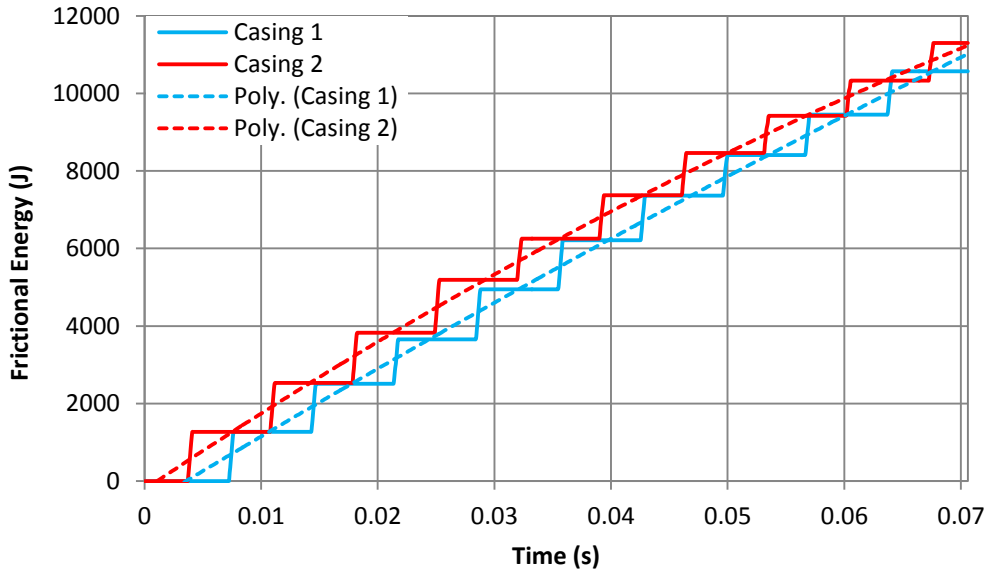

Fig. 7.10 – Frictional energies of Blade 1 after contact with Casings 1 and 2

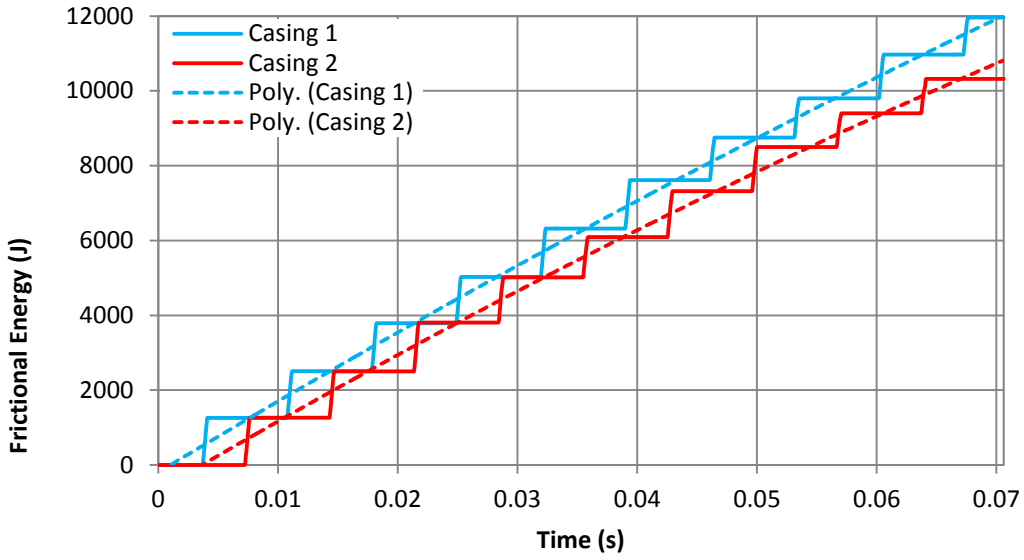

Fig. 7.11 – Frictional energies of Blade 2 after contact with Casings 1 and 2

Frictional energy for the first contact event is approximately 1.25 kJ. Ideally, the frictional energies should have the same magnitude throughout the simulation since the casing material is defined to be elastic and no material erosion is allowed to take place at the contacting surfaces; however, from Fig. 7.10 and Fig. 7.11, it

can be seen that the energy per contact for each of the blades tends to decrease over time. This can be attributed to the hourglassing phenomenon, seen in Section 7.3.1, which results in distortion of casing elements. Also, frictional energies of each blade after contact with Casing 1 tend to follow a linear trend, whereas frictional energies after contact with Casing 2 are seen to decrease nonlinearly. This suggests that contact with Casing 2 is intermittent and reduced over time due to the fact that Casing 2 suffers a more severe distortion of elements due to hourglassing than Casing 1. This is further confirmed by looking at the contact forces shown in Fig. 7.12.

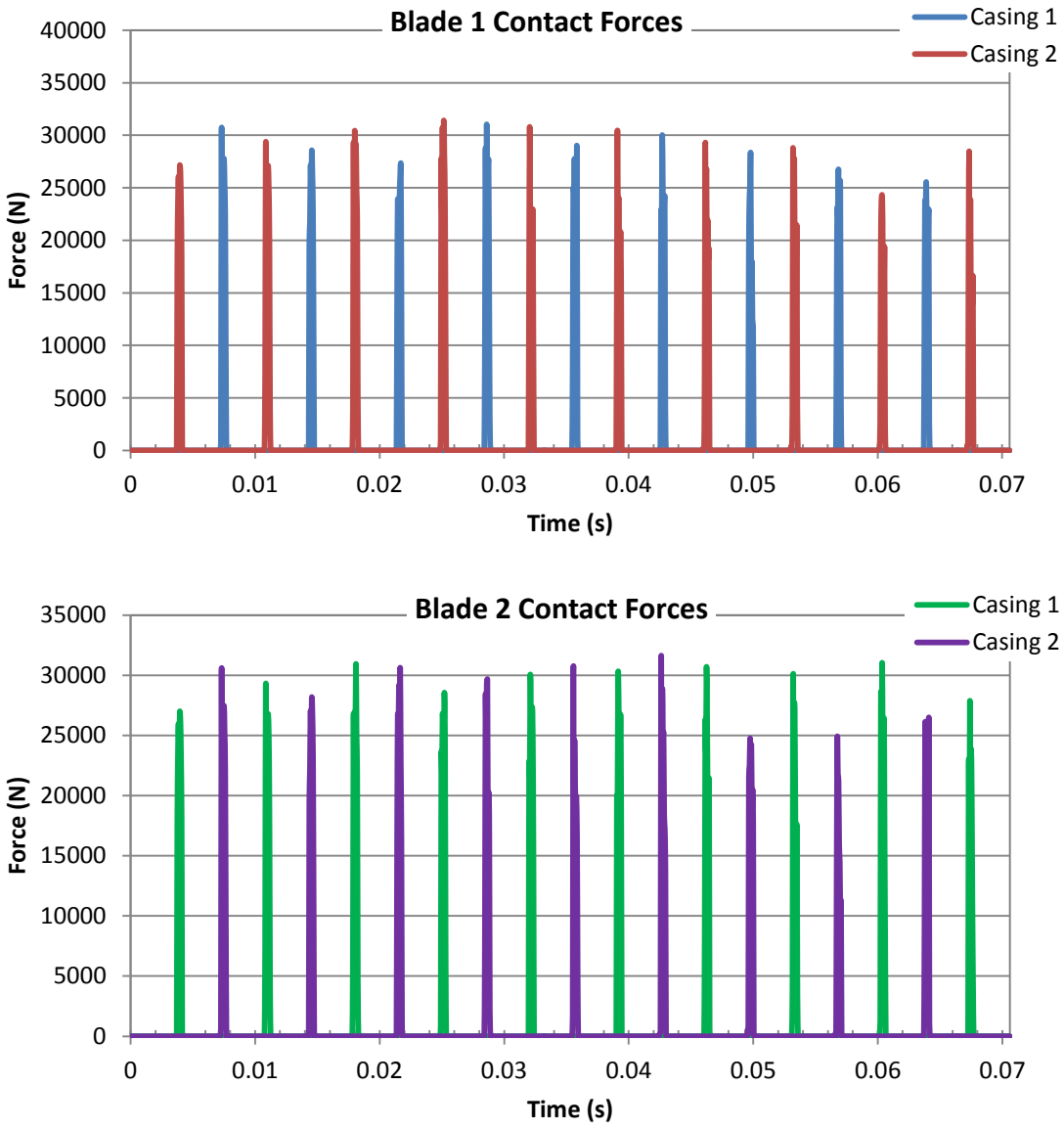

Fig. 7.12 – Contact forces for Blade 1 and Blade 2

7.3.2 Displacement Results

Displacement graphs are presented for the blades. The nodes on the top of the blade are the ones most likely to experience the maximum amplitudes in vibration during tip-rubbing; therefore, results are processed from this location for both the blades (Fig. 7.13). All results are computed from the rotating local coordinate systems specified on the blades (Fig. 7.4).

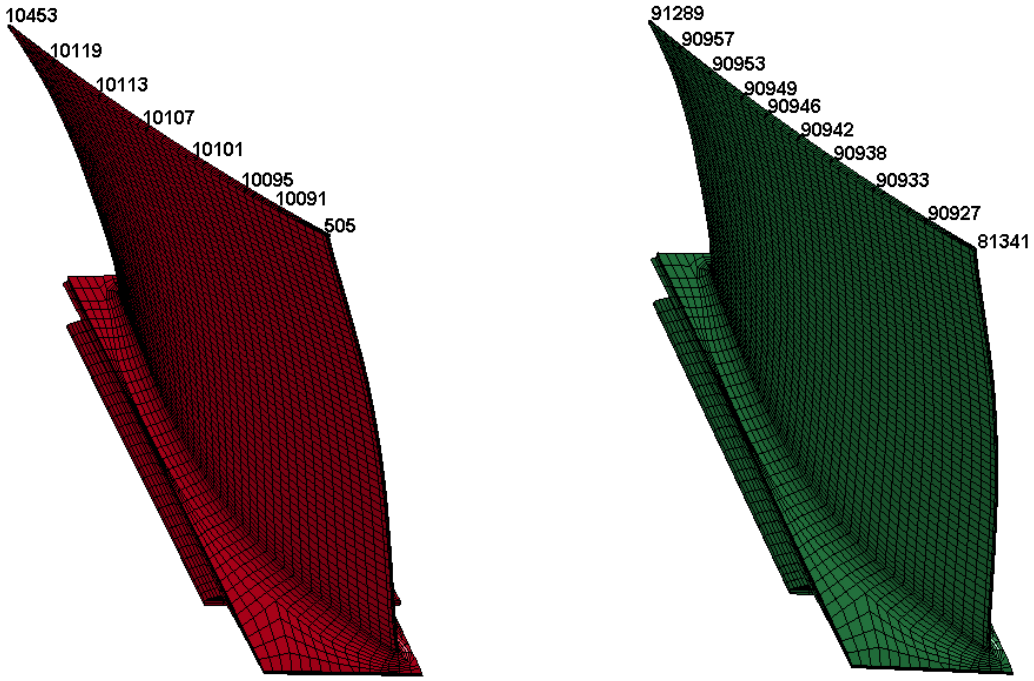

(a) Blade 1 *(b) Blade 2*

Fig. 7.13 – Nodes on each blade for which results are computed

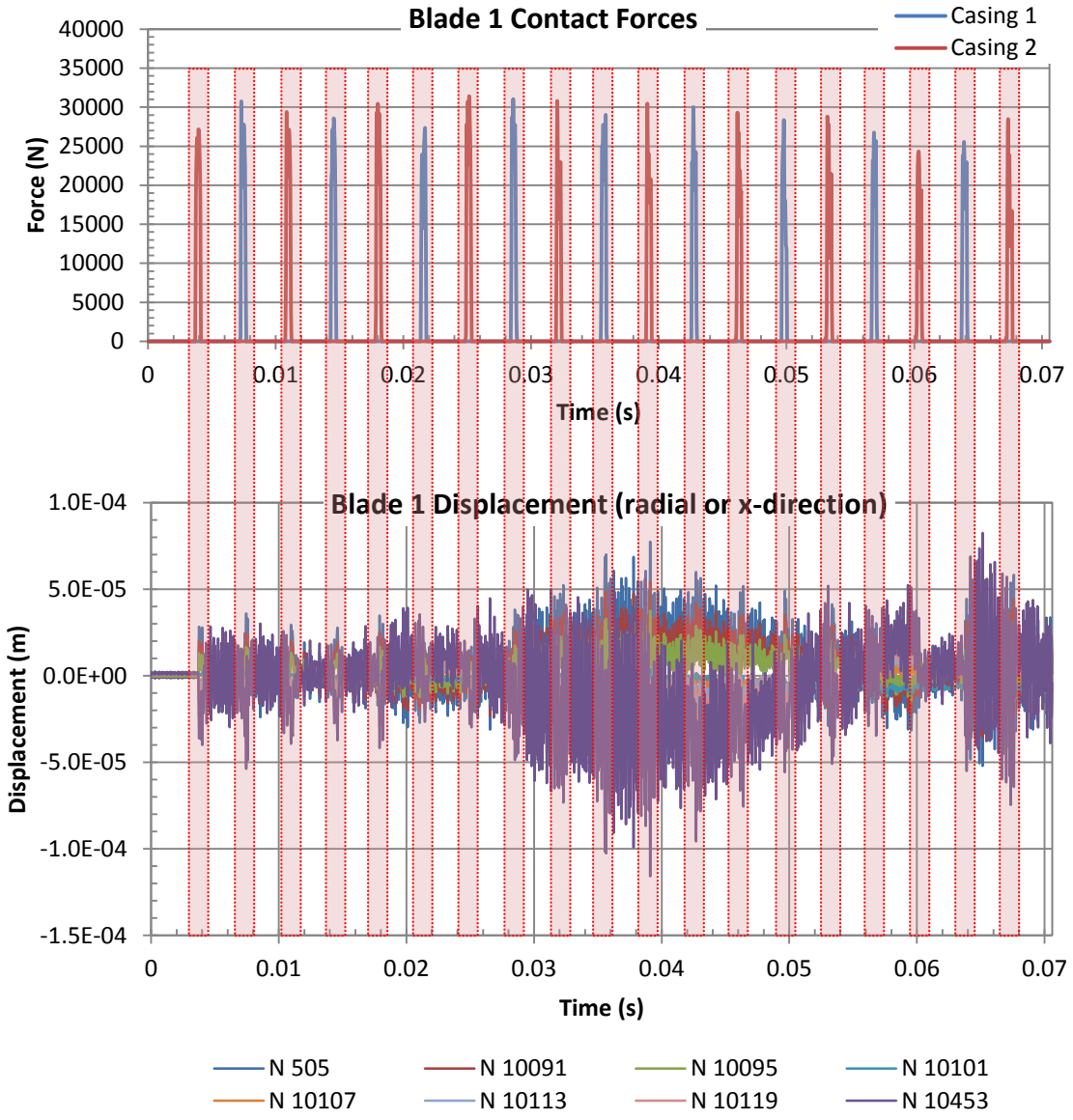

Fig. 7.14 – Displacements of Blade 1 nodes in radial direction and contact forces

Fig. 7.14 shows that there is a spike in nodal displacement in the radial direction whenever contact occurs. After eight contact events ($t \approx 0.028$ s), the displacement pattern changes; Node 10453 (on the leading edge tip) is seen to vibrate in the opposite direction to Node 505 (on the trailing edge tip) until $t = 0.061$ s. Also, the amplitude of vibration is much higher. This suggests that between these two time limits, the blade undergoes resonance in torsional mode in the radial direction.

After t = 0.064 s, vibration amplitude of Node 10453 is seen to increase suddenly; this is also true of the other nodes. This is possibly due to flexural mode of resonance.

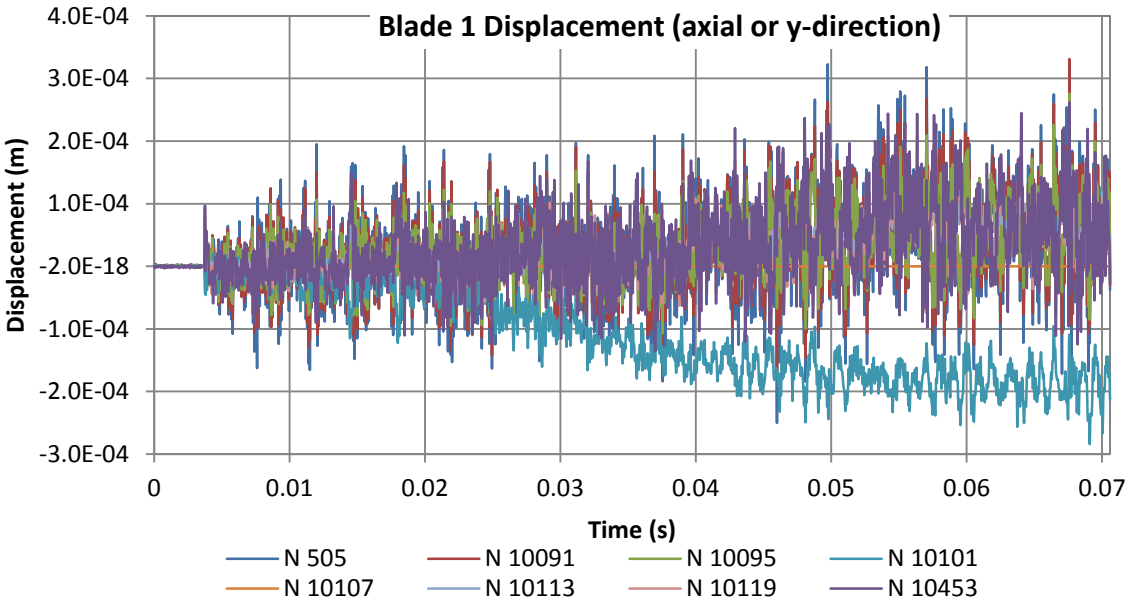

(a)

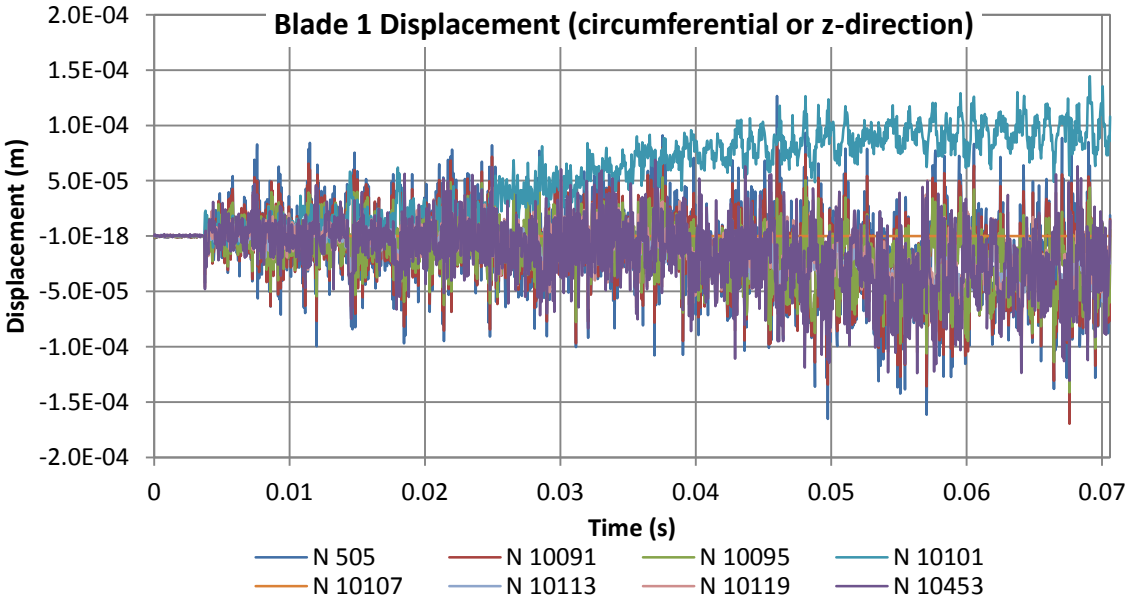

(b)

Fig. 7.15 – Displacements of Blade 1 nodes in (a) axial direction (b) circumferential direction

From Fig. 7.15, it can be seen that the amplitude of vibration grows with time; there is little evidence of resonance and no anomalies are noticed except at Node 10101 which is located close to the trailing edge. The behaviour of Node 10101 shows a permanent shift in displacement in the y- and z-directions. This suggests that plastic deformation of elements near Node 10101 seem to have occurred in the axial and circumferential directions; further analysis of the plastic strains seen in the blade tip (Fig. 7.16) proves this to be the case.

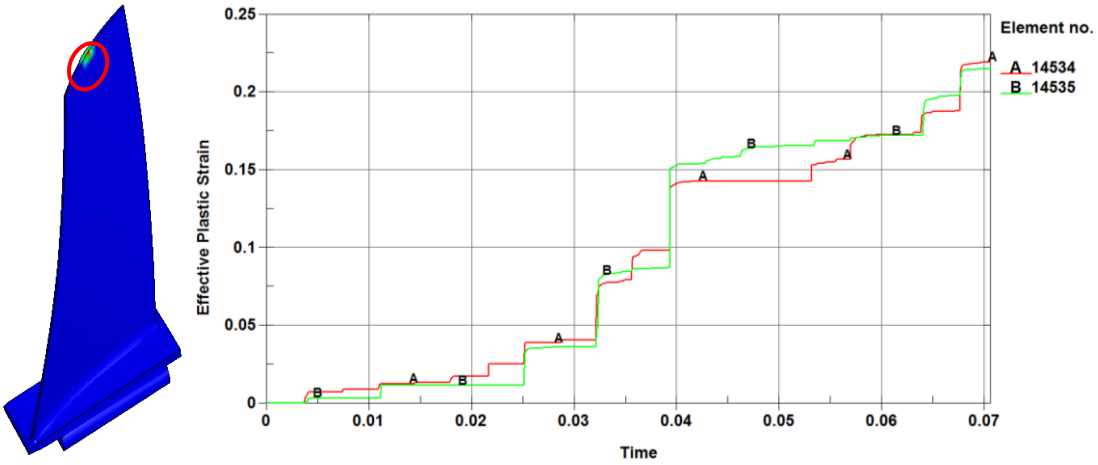

Fig. 7.16 – Effective plastic strains on Blade 1 tip (region circled in red) [Units: time (s)]

Displacements of Blade 2 in the radial, axial and circumferential are shown in Fig. 7.17. It can be seen that response is of Blade 2 is very different from Blade 1 even though both blades are symmetrically opposite and are subject to the same boundary conditions. Discrepancies in initial stresses have already been noticed between the two blades.

Torsional vibration is noticed in the radial direction between the leading and trailing edge tips between t = 0.04 s and t = 0.05 s; beyond that, the nodes show a permanent shift in amplitude. Like Blade 1, plastic strains are observed in this region and elements are seen to have yielded. Permanent deformation observed in the yield zone is also the reason for the sudden shifts in vibration amplitudes of Node 90938 in the axial and circumferential directions.

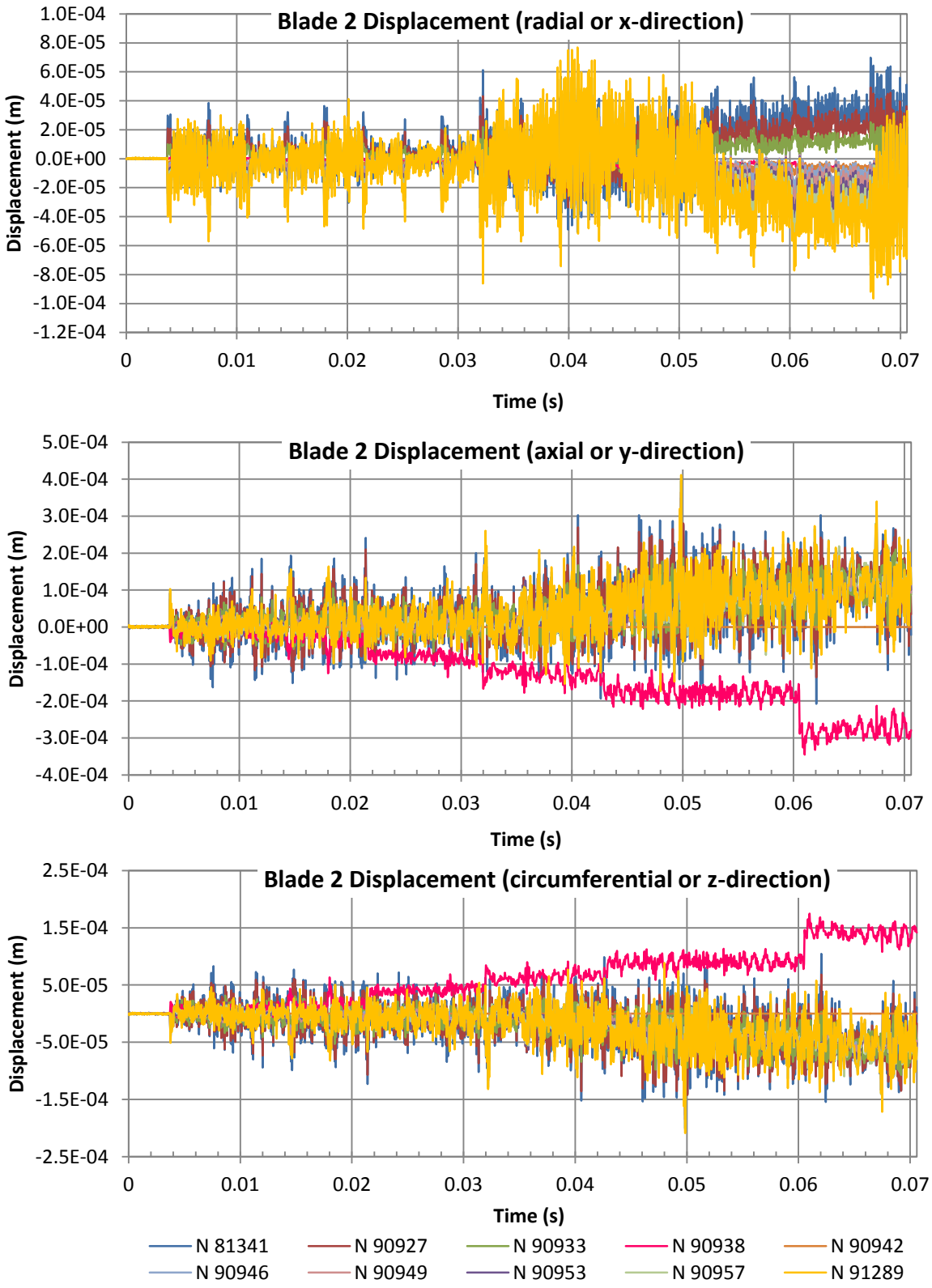

Fig. 7.17 – Displacements of Blade 2 nodes in radial, axial and circumferential directions

7.3.3 Frequency Response Results

Frequency response curves for the tip-rubbing analysis are presented in this section. LS-PrePost and SIGVIEW software were used to process the displacement results obtained from the tip-rubbing analysis. The displacement curves seen in Section 7.3.2 are converted from time domain to frequency domain using FFT (Fast Fourier Transform); this is done using SIGVIEW. A spike in response amplitude at a certain frequency most likely means resonant behaviour at that frequency.

The complete frequency response curves for both blades are shown in Appendix D; only regions where nonlinear behaviour is observed are included in this section. The frequency response curves for both blades are identical; therefore, only Blade 1 will be discussed.

7.3.3.1 Response in Local X-Direction

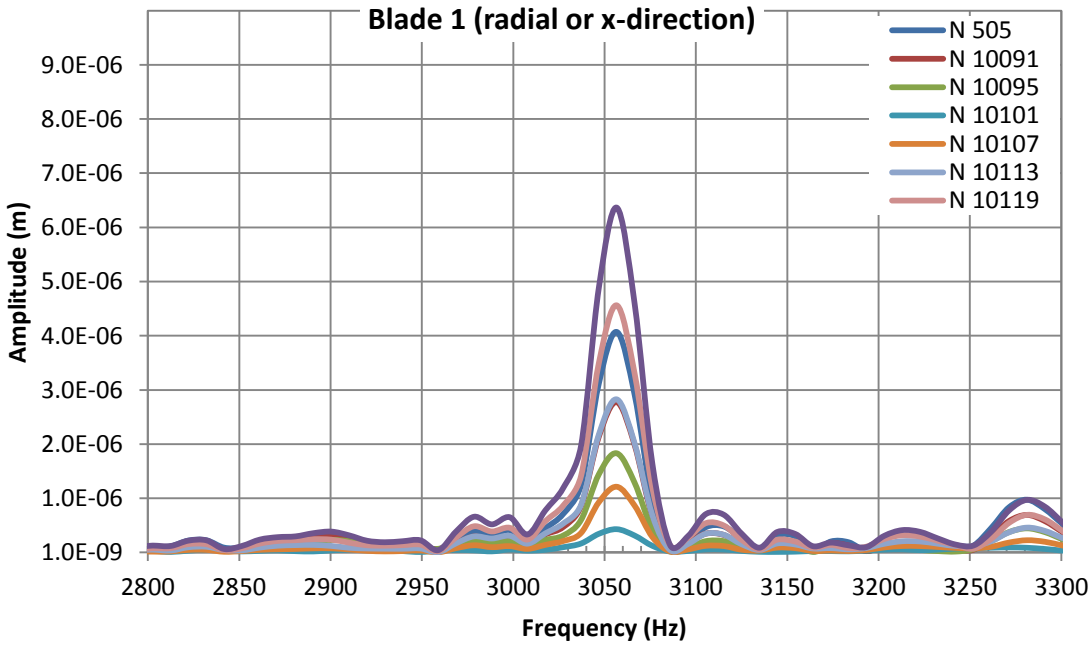

Fig. 7.18 – Frequency response curves in radial direction for Blade 1 (2800 Hz – 3300 Hz)

During tip-rubbing, sudden spikes in amplitude are seen at approximately 280 Hz intervals from 0 Hz till 2000 Hz. These spikes are attributed to be a

reaction of the blade due to contact with casing segments and not resonant behaviour. The frequency of contact is calculated to be equal to 283 Hz which is twice the angular velocity of of the blade (890 rad/s or 141.65 Hz) since contact event occurs twice per revolution. Therefore, these spikes are ignored.

The first nonlinear behaviour in the radial direction is detected at 3062.5 Hz (Fig. 7.18). The curves show hardening nonlinearity; that is, the frequency increases with amplitude and the curve tends to lean towards higher frequencies. The amplitude of vibration is 6.5 μm. However, this nonlinear behaviour does not coincide with any of the resonant frequencies determined from modal analysis in Chapter 6.

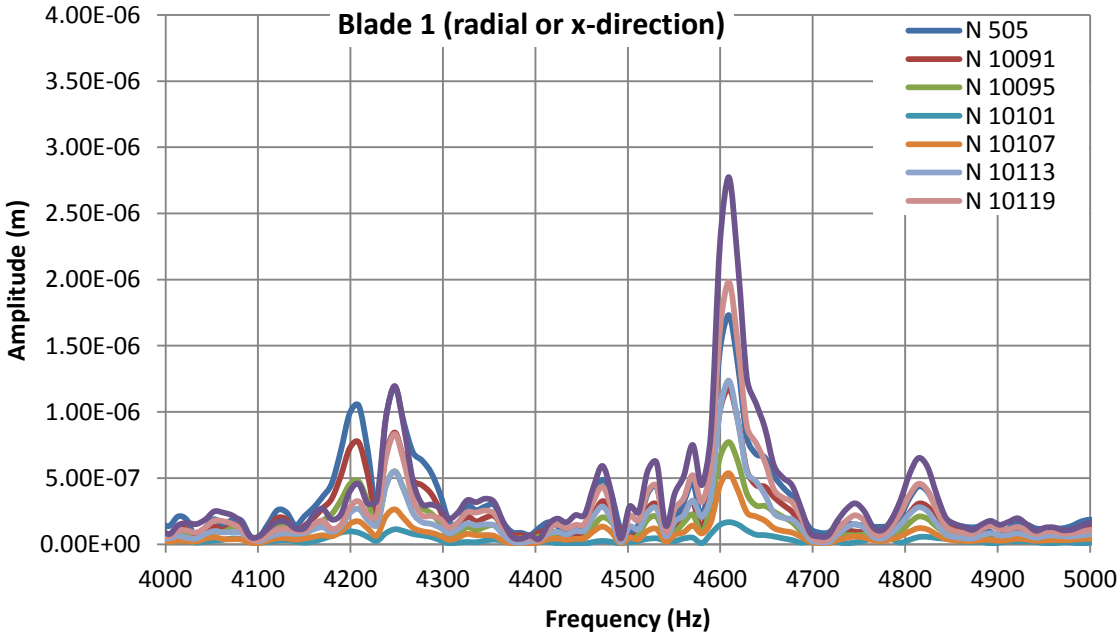

Fig. 7.19 – Frequency response curves in radial direction for Blade 1 (4000 Hz – 5000 Hz)

As can be seen from Fig. 7.19, the next nonlinear behaviour is detected at 4200 Hz (hardening), 4250 Hz (softening) and 4600 Hz (softening). These frequencies do not coincide with any resonant frequencies. The response curves are not very distinct and maximum amplitude detected is 2.8 μm. It is unlikely that the nonlinearities observed between 4000 Hz – 5000 Hz will pose any problems.

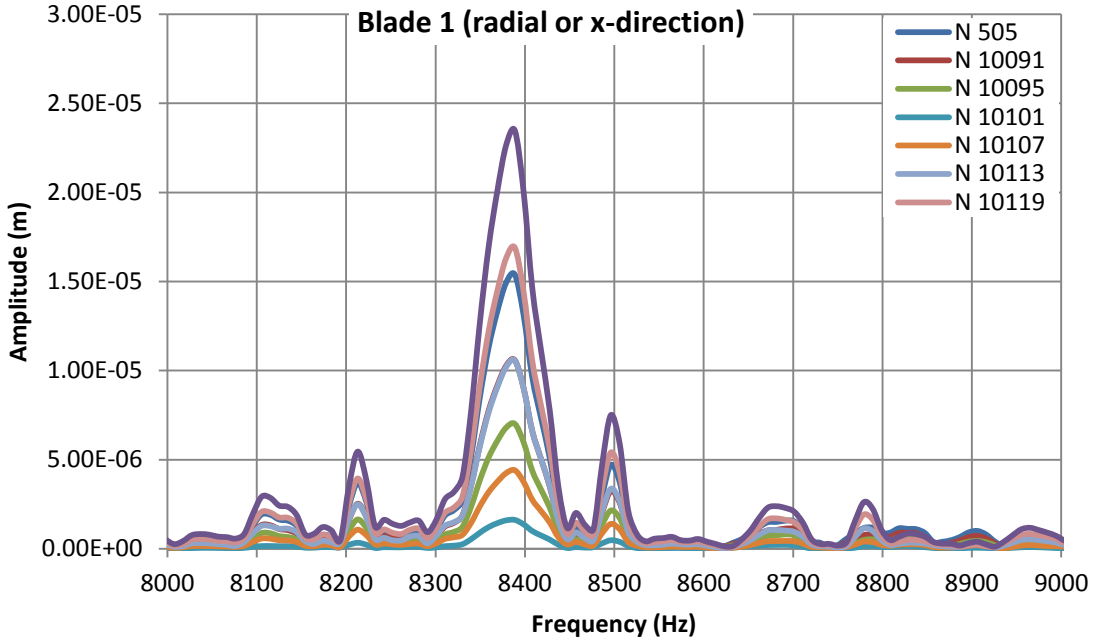

Fig. 7.20 – Frequency response curves in radial direction for Blade 1 (8000 Hz – 9000 Hz)

In Fig. 7.20, hardening nonlinearity is seen at 8380 Hz with an amplitude response of 23 μm. It is suspected that it is a resonant frequency due to the high amplitude of vibration; however, since the modal analysis in Chapter 6 calculated only the first fifteen modes, it is unknown if resonance occurs at this frequency. If the nonlinear behaviour observed is at a resonant frequency, further analysis is required to identify if it is likely to cause any damage to the blade in the long run.

7.3.3.2 Response in Local Axial Direction

The following figures show response of Blade 1 in the axial direction. Frequency response curves for the circumferential direction are identical to the axial direction and therefore not included.

The response curves are noisy and show no distinct nonlinearities; however, it should be remembered that the blade responses are affected as a result of hourglassing of the casing and therefore should be used with caution.

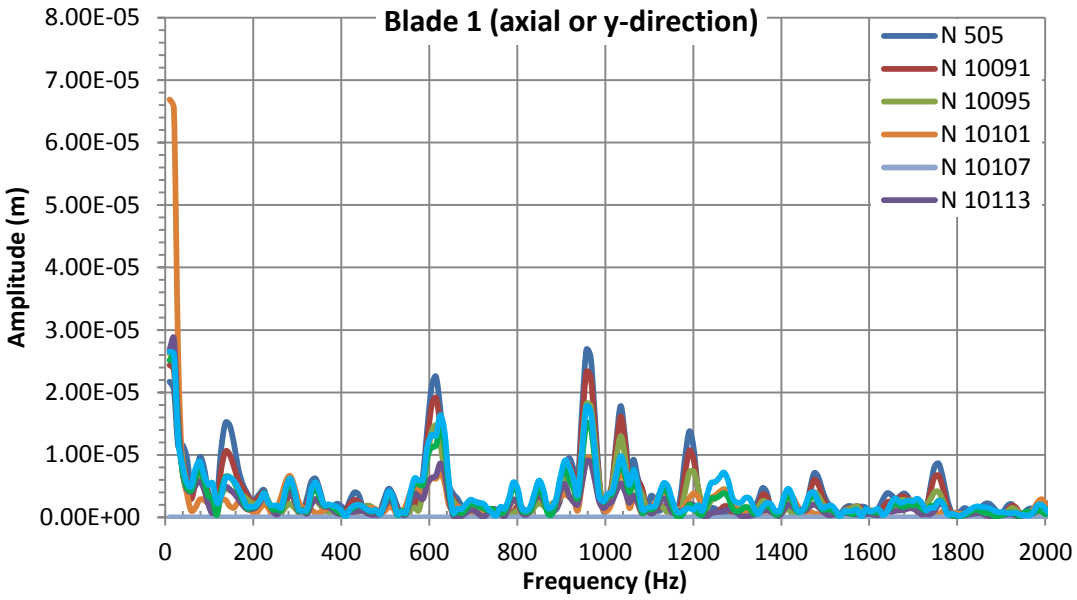

Fig. 7.21 – Frequency response curves in axial direction for Blade 1 (0 Hz – 2000 Hz)

Fig. 7.21 shows response between 0 Hz and 2000 Hz; there are suggestions of hardening nonlinear behaviour occurring at around 600 Hz with an amplitude of 22 μm; this does not occur at a resonant frequency. In Fig. 7.22, nonlinear behaviour is seen at 7350 Hz at an amplitude of 23 μm. This is close to Mode 14 (7225 Hz) which is a combined flexural-torsional mode.

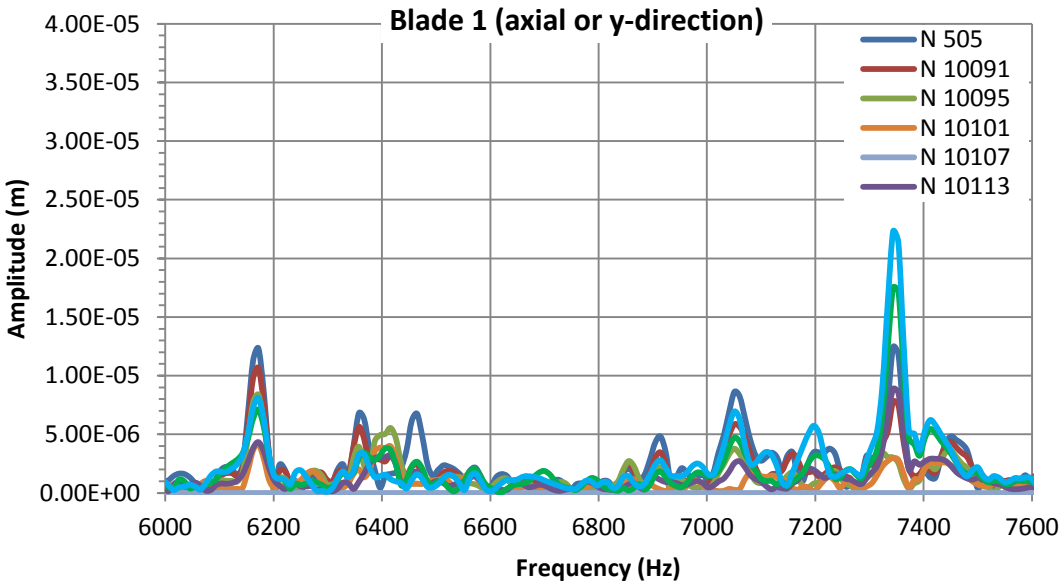

Fig. 7.22 – Frequency response curves in axial direction for Blade 1 (6000 Hz – 7600 Hz)

Overall from the frequency response curves it can be concluded that although nonlinear behaviour is detected in the compressor blades it does not lead to hysteretic behaviour of the blades since no amplitude jumps are detected at resonance.

Resonant frequencies determined from modal analysis are not detected on the frequency amplitude curves although resonant behaviour is noticed on the displacement curves. This leads to the conclusion that the nonlinear vibrations seen lead to resonant behaviour in the blade even if they do not occur at resonant frequencies. Therefore, jumps could exist in the system which have not been detected in the analysis.

Chapter 8 – Conclusions and Recommendations

8.1 Conclusions

The objective of this project was to identify nonlinear vibration of an IP compressor blade in the Trent 900 when tip-rubbing occurs. The results indicate nonlinear behaviour of the blade as a result of tip-rubbing; however, no jumps in amplitude at resonances are discovered. The simulation results were affected adversely by hourglassing of the casing segments. There are a few recommendations which can be used to overcome hourglassing and improve the quality of results. These are discussed in the next section.

8.2 Recommendations

Review of current literature on analytical rotor-stator interactions covered in Chapter 2 has discovered that full annular rub leads to nonlinear vibration and amplitude jumps at resonance. It would be of interest to apply this theory to the blade-casing interaction by modelling interaction of the whole bladed assembly with the casing.

The procedure used to generate FFT in most software (such as MATLAB and Microsoft Excel) is generally linear in nature. Therefore, software which can identify and analyse nonlinear vibration can be applied to this project in the future. The author is aware of two software – TISEAN [16] and TSTOOL [21] which are used for analysis of nonlinear time series data; these software require prior knowledge of programming. Various toolboxes available in MATLAB can also be used to identify nonlinear vibration in the system.

Various algorithms are available to postprocess and identify nonlinearity in vibrating systems. A thesis by Dinardo [13] outlines a method called the HTM

(Harmonic Tracking Method) which has been used to identify the nonlinearities in a vibrating cantilever beam with success.

Hourglassing of the casing sections were observed after multiple interactions of with the rotating blades. The results of the simulation have been affected by the increasing distortion of the casing interior surface due to hourglassing modes. This can be prevented altogether by resolving the contact forces due to the first tip-rubbing event into its components along the normal and tangential directions and then applying these forces to the blade (Fig. 8.1). A further explanation of this concept is provided in [33].

The tangential force $F_{tangent}$ is the frictional force exerted on the blade due to contact with the casing; this is expected to remain constant over time. However, the magnitude of the normal force F_{norm} will vary with time since its value during one contact event varies according to the location where contact occurs between the blade and the casing. The normal force is compressive in nature and can be calculated by

$$F_{norm}(t) = [K_{cc}]_{NxN}\left\{(\delta_i(\theta,t) - C)\cos\phi + \beta_{i,radial}^{(tip)}\cos\phi - \beta_{i,axial}^{(tip)}\sin\phi\right\} \qquad (8.1)$$

Where

$[K_{cc}]_{NxN} = \text{contact} - \text{normal stiffness}$

$N = \text{number of nodes at blade tip}$

$\delta_i = \text{radial nodal interferences}$

$\phi = \text{cone angle of casing/blade tip}$

$\beta = \text{arc of rub contact}$

$\theta = \text{angular location on blade tip}$

Therefore, it will no longer be necessary to simulate the casing. This will reduce computation time and hourglassing errors in the simulation are also avoided.

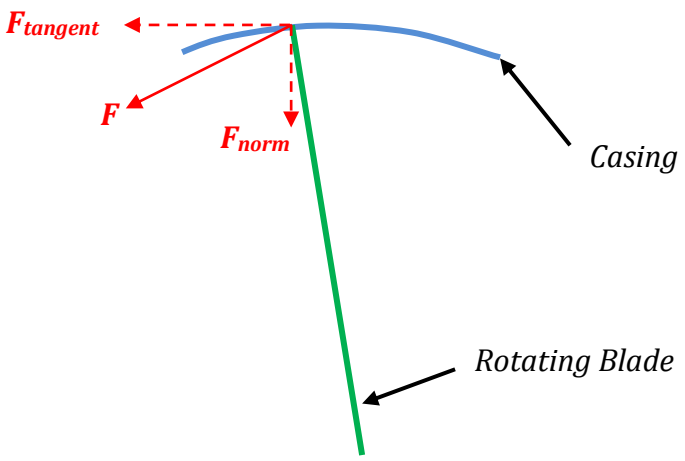

Fig. 8.1 – Resolving contact forces analytically to replace interaction of casing with blade

References

[1] *ANSYS Release 11.0 Documentation for ANSYS; Chapter 9. Hourglassing*, available at: http://www.kxcad.net/ansys/ANSYS/ansyshelp/Hlp_L_hour1.html (accessed 03/12/2011).

[2] *Aircraft Accident Report – National Airlines, Inc. DC-10-10, N60NA, Near Albuquerque, New Mexico, November 3, 1973,* (1975), NTSB-AAR-75-2, National Transportation Safety Board, Washington, D.C. 20591.

[3] *Aircraft Accident Report – In-Flight Engine Separation Japan Airlines, Inc, Flight 46e Boeing 747-121,* (1993), NTSB/AAR-93/06, National Transportation Safety Board, Washington, D.C. 20594.

[4] *Contact Modelling in LS-DYNA - Contact Parameters* (2001), available at: http://www.dynasupport.com/tutorial/contact-modeling-in-ls-dyna/contact-parameters (accessed 20/09/2011).

[5] *LS-DYNA Theory Manual* (2006), Livermore Software Technology Corporation, Livermore, California 94551.

[6] *LS-DYNA Keyword User's Manual* (2007), Version 971 ed., Livermore Software Technology Corporation, Livermore, California 94551.

[7] *Virgin Driver* (2010), available at: http://virginflightdeck.blogspot.com/ (accessed 11/11/2011).

[8] Aidanpää, J. and Lindkvist, G. (2010), "Dynamics of a Rubbing Jeffcott Rotor with Three Blades", *Proceedings of the Third Chaotic Modeling and Simulation International Conference,* 1 - 4 June 2010, Chania, Crete, Greece, .

[9] Australian Transport Safety Bureau (2008), *In-flight engine failure, Sydney, Boeing Company 747-438, VH-OJM, 03 February 2007,* 200700356.

[10] Chu, F. and Lu, W. (2007), "Stiffening effect of the rotor during the rotor-to-stator rub in a rotating machine", *Journal of Sound and Vibration,* vol. 308, no. 3-5, pp. 758-766.

[11] Dai, X., Jin, Z. and Zhang, X. (2002), "Dynamic behaviour of the full rotor/stop rubbing", *Journal of Sound and Vibration,* vol. 251, no. 5, pp. 807-822.

[12] De Ryck, H. (2008), *Turbofan Design for the Commercial Aircraft,* Warsaw University of Technology, Warsaw, Poland.

[13] Dinardo, J. E. (2009), *Signal Processing Techniques for Nonlinearity Identification of Structures Using Transient Response* (Master of Science thesis), University of Missouri, Missouri, USA.

[14] Ghasripoor, F., Schmid, R. and Dorfman, M. (2001), *Abradable Coatings Increase Gas Turbine Engine Efficiency*, available at: http://www.azom.com/article.aspx?ArticleID=739 (accessed 06/11/2011).

[15] Gryczewski, Ł. (2009), *Simulation of Compressor Blade Tip Rubbing* (Master of Science thesis), Cranfield, United Kingdom.

[16] Hegger, R., Kantz, H. and Schreiber, T., *TISEAN: Nonlinear Time Series Analysis*.

[17] Husband, J. B. (2007), *Developing an Efficient FEM Structural Simulation of a Fan Blade Off Test in a Turbofan Jet Engine.* (Doctor of Philosophy thesis), University of Saskatchewan, Saskatoon, Saskatchewan, Canada.

[18] Isaksson, J. L. (1994), "Dynamics of a rotor with annular rub", *Proceedings of the Fourth International Conference on Rotor Dynamics,* Chicago, USA, pp. 85-90.

[19] Kascak, A. F., Palazzolo, A. B. and Montague, G. (1987), "Transient Rotor Dynamic Rub Phenomena, Theory and Test", *American Society of Mechanical Engineers,* vol. 2, pp. 485-494.

[20] McMillan, A., (2008), *Material development for fan blade containment casing*.

[21] Merkwirth, C., Parlitz, U., Wedekind, I., Engster, D. and Lauterborn, W., *TSTOOL*.

[22] Muzynska, A. (2005), *Rotordynamics (Dekker Mechanical Engineering),* 1st ed, CRC Press.

[23] Rajendran, P. R. C. (2010), *Simulation of Engine Tip Rubbing using LSDYNA* (unpublished MSc Aerospace Vehicle Design thesis), Cranfield Unversity, Cranfield, United Kingdom.

[24] Rolls-Royce (2005), *The Jet Engine,* 5th ed, Rolls-Royce Technical Publications.

[25] Rolls-Royce (2011), *Trent 900 - Optimised for the Airbus Family,* VCOM13797, Rolls-Royce.

[26] Sinha, S. K. and Dorbala, S. (2009), "Dynamic Loads in the Fan Containment Structure of a Turbofan Engine", *Journal of Aerospace Engineering,* , pp. 260.

[27] Turner, K. E., Dunn, M. and Padova, C. (2012), "Airfoil Deflection Characteristics During Rub Events", *Journal of Turbomachinery,* vol. 134, no. 1, pp. 011018-1.

[28] Worden, K. and Tomlinson, G. R. (2001), *Nonlinearity in structural dynamics: detection, identification, and modelling,* IOP Publishing Ltd, Bristol and Philadelphia.

[29] Yu, J. J., Goldman, P., Bently, D. E. and Muzynska, A. (2002), "Rotor/Seal Experimental and Analytical Study on Full Annular Rub", *Journal of Engineering for Gas Turbines and Power,* vol. 124, no. 2, pp. 340.

[30] Zhang, H. and Chen, Y. (2011), "Bifurcation analysis on full annular rub of a nonlinear rotor system", *Science China Technological Sciences,* vol. 54, no. 8, pp. 1977-1985.

[31] Erhart, T. (2011), "Review of Solid Element Formulations in LS-DYNA: Properties, Limits, Advantages, Disadvantages", *2011 Developers' Forum,* Stuttgart, Germany.

[32] Cervenka, M., (2000), *The Rolls-Royce Trent Engine*.

[33] Turner, K. E., Dunn, M. and Adams, M. (2005), "Simulation of Engine Blade Tip-Rub Induced Vibration", *Proceedings of GT2005 (ASME Turbo Expo 2005),* June 6 - 9 2005, Reno-Tahoe, Nevada, USA, ASME.

Appendices

Appendix A – Input Files for Implicit and Explicit Analysis

A.1 Input File for Implicit Prestress Static Solution

***TITLE**

Implicit Loading for dynamic relaxation

***CONTROL_TERMINATION**

$$ ENDTIM ENDCYC DTMIN ENDENG ENDMAS

10.0

***CONTROL_SOLID**

$$ ESORT FMATRX NIPTETS SWLOCL

1 2

$$ PM1 PM2 PM3 PM4 PM5 PM6 PM7 PM8 PM9 PM10

***CONTROL_IMPLICIT_GENERAL**

$$ IMFLAG DT0 IMFLAG NSBS IGS CNSTN FORM ZERO_V

1 0.1 1 1 2

$$DATABASE_OPTION -- Control Cards for ASCII output

***DATABASE_SECFORC**

1.0 0

***DATABASE_BINARY_D3PLOT**

$$ DT/CYCL LCDT BEAM NPLTC

0.05 0 0 0 0

0

***MAT_ELASTIC_TITLE**

$HMNAME MATS 1TitaniumMATL1

blade titanium

1 4430.01.1380E+11 0.342

***PART**

$HMNAME COMPS 1Blade

$HWCOLOR COMPS 1 49

blade

1 3 1 0 4

***SECTION_SOLID_TITLE**

$HMNAME PROPS 3Blade

blade

3 18

***HOURGLASS**

$HMNAME PROPS 4HourglassCard

4 1

$$ Base Accelerations and Angular Velocities

***LOAD_BODY_RX**

$HMNAME LOADCOLS 2LoadBody_2

$HWCOLOR LOADCOLS 2 3

1

***LOAD_BODY_PARTS**

$HMNAME LOADCOLS 2LoadBody_2

$HWCOLOR LOADCOLS 2 3

6

***INTERFACE_SPRINGBACK_LSDYNA**

$HMNAME LOADCOLS 1Springback_1

$HWCOLOR LOADCOLS 1 7

$ PSID NSHV

6 10000 0

***DATABASE_CROSS_SECTION_SET_ID**

$HMNAME GROUPS 2BladeBaseForces

$HWCOLOR GROUPS 2 21

2

10 9 0 0

***DEFINE_CURVE_TITLE**

$HMNAME CURVES 1LoadBody_Curve

$HWCOLOR CURVES 1 17

```
$HMCURVE    1    2 LoadBody_Curve
curve1
      1       0      1.0      1.0      0.0      0.0        0
             0.0              0.0
            10.0            890.0
```

A.2 Input File for Explicit Transient Rotation

```
*CONTROL_TERMINATION
$$ ENDTIM    ENDCYC    DTMIN    ENDENG    ENDMAS
  0.0212
*CONTROL_TIMESTEP
$$ DTINIT    TSSFAC     ISDO    TSLIMT     DT2MS     LCTM     ERODE     MSIST
    0.0       0.9                                  1
*CONTROL_OUTPUT
$$   NPOPT    NEECHO    NREFUP    IACCOP    OPIFS    IPNINT    IKEDIT
       1         3
*CONTROL_ENERGY
$$    HGEN     RWEN    SLNTEN     RYLEN
       2         2         2
*CONTROL_ACCURACY
$$ OSU         INN    PIDOSU
       1         2
$$DATABASE_OPTION -- Control Cards for ASCII output

*DATABASE_GLSTAT
1.0000E-04         0
*DATABASE_MATSUM
1.0000E-04         0
*DATABASE_NODOUT
1.0000E-04         0
*DATABASE_BINARY_D3PLOT
$$ DT/CYCL     LCDT     BEAM     NPLTC
1.0000E-04         0         0         0         0
       0
*MAT_ELASTIC
$HMNAME MATS      1Titanium
       1    4430.01.1380E+11     0.342
```

***PART**

$HMNAME COMPS 1Blade

$HWCOLOR COMPS 1 3

1 1 1

***SECTION_SOLID**

$HMNAME PROPS 1BladeSectSolid

1 18

***HOURGLASS**

$HMNAME PROPS 2HourGlas

2 1 0.0 0 0.0 0.0

***INITIAL_VELOCITY_GENERATION**

$HMNAME LOADCOLS 2InitialVel

$HWCOLOR LOADCOLS 2 18

1 2 890.0 0

0.0 0.0 0.0 1.0 0.0 0.0 0

***BOUNDARY_PRESCRIBED_MOTION_SET**

$HMNAME LOADCOLS 1Rotation

$HWCOLOR LOADCOLS 1 7

2 9 0 1 1.0 0 0.0 0.0

18707

***INTERFACE_SPRINGBACK_LSDYNA**

$HMNAME LOADCOLS 3Springback

$HWCOLOR LOADCOLS 3 7

$ PSID NSHV

3 10000

***INITIAL_STRESS_SOLID**

$$ This contains the initial stress states of the blade imported from implicit step file

***DEFINE_CURVE**

$HMNAME CURVES 1LoadCurve

$HWCOLOR CURVES 1 3

```
$HMCURVE    1    2 LoadCurve
      1       0     1.0      1.0      0.0      0.0       0
            0.0            890.0
           10.0            890.0
```

Appendix B – Input File for Modal Analysis

```
*CONTROL_IMPLICIT_EIGENVALUE
$$  NEIG    CENTER    LFLAG   LFTEND    RFLAG   RHTEND   EIGMTH   SHFSCL
      15
*CONTROL_IMPLICIT_GENERAL
$$ IMFLAG      DT0   IMFLAG     NSBS      IGS    CNSTN     FORM   ZERO_V
       11.0000E-03
*MAT_ELASTIC_TITLE
$HMNAME MATS       1TitaniumMATL1
blade titanium
       1    4430.01.1380E+11     0.342
*PART
$HMNAME COMPS       1Blade
$HWCOLOR COMPS       1      49
blade
       1        3        1        0        4
*SECTION_SOLID_TITLE
$HMNAME PROPS       3Blade
blade
       3       18
*HOURGLASS
$HMNAME PROPS       4HourglassCard
       4        1
*BOUNDARY_SPC_NODE
$HMNAME LOADCOLS       Constraints
```

For the prestressed modal analysis, the *INITIAL_STRESS_SOLID card is included. This contains the stress output from the implicit prestress static analysis.

Appendix C – Input File for Blade Tip-Rubbing

***CONTROL_TERMINATION**

$$ ENDTIM ENDCYC DTMIN ENDENG ENDMAS

0.0353

***CONTROL_TIMESTEP**

$$ DTINIT TSSFAC ISDO TSLIMT DT2MS LCTM ERODE MSIST

1.1384E-08 0.9 1

***CONTROL_CONTACT**

$$ SLSFAC RWPNAL ISLCHK SHLTHK PENOPT THKCHG ORIEN ENMASS

$$ USRSTR USRFRC NSBCS INTERM XPENE SSTHK ECDT TIEDPRJ

0

$$ SFRIC DFRIC EDC INTVFC TH TH_SF PEN_SF

$$ IGNORE FRCENG SKIPRWG OUTSEG SPOTSTP SPOTDEL SPOTHIN

1 1

***CONTROL_OUTPUT**

$$ NPOPT NEECHO NREFUP IACCOP OPIFS IPNINT IKEDIT

1 3

***CONTROL_ENERGY**

$$ HGEN RWEN SLNTEN RYLEN

2 2 2 2

***CONTROL_ACCURACY**

$$ OSU INN PIDOSU

1 2

$$DATABASE_OPTION -- Control Cards for ASCII output

***DATABASE_ELOUT**

5.0000E-05 0

***DATABASE_GLSTAT**

5.0000E-05 0

***DATABASE_MATSUM**

5.0000E-05 0

***DATABASE_NCFORC**

5.0000E-05 0

***DATABASE_NODOUT**

5.0000E-05 0

***DATABASE_RCFORC**

5.0000E-05 0

***DATABASE_SLEOUT**

5.0000E-05 0

***DATABASE_BINARY_D3PLOT**

$$ DT/CYCL LCDT BEAM NPLTC

1.0000E-04 0 0 0 0

0

***DATABASE_BINARY_INTFOR**

$$ DT/CYCL LCID

5.0000E-05

***DATABASE_EXTENT_BINARY**

$$ NEIPH NEIPS MAXINT STRFLG SIGFLG EPSFLG RLTFLG ENGFLG

1

$$ CMPFLG IEVERP BEAMIP DCOMP SHGE STSSZ N3THDT IALEMAT

1

$$ NINTSLD PKP_SEN SCLP MSSCL THERM

***DEFINE_COORDINATE_NODES**

1 16119 10107 17310

2 96955 90942 98146

***MAT_ELASTIC**

$HMNAME MATS 3Casing_MAT001

3 4430.08.0000E+09 0.33

***MAT_PLASTIC_KINEMATIC**

$HMNAME MATS 2Titanium_MAT003

2 4430.01.1380E+11 0.3421.0980E+091.9720E+09 0.0

120.0 9.0 0.6 0

***PART**

$HMNAME COMPS 1Blade

$HWCOLOR COMPS 1 3

1 1 2 2

$HMNAME COMPS 2FullCasing

$HWCOLOR COMPS 2 21

2 17 3 2

$HMNAME COMPS 3Blade2

$HWCOLOR COMPS 3 37

3 1 2 2

***SECTION_SOLID**

$HMNAME PROPS 1BladeSectSolid

1 1

$HMNAME PROPS 17CasingSectSolid

17 1

***HOURGLASS**

$HMNAME PROPS 2HourGlas

2 5 0.03 0 0.0 0.0

***INITIAL_VELOCITY_GENERATION**

$HMNAME LOADCOLS 1InitialVel

$HWCOLOR LOADCOLS 1 18

1 2 890.0 0

0.0 0.0 0.0 1.0 0.0 0.0 0

***INITIAL_VELOCITY_GENERATION**

$HMNAME LOADCOLS 2InitialVel_Blade2

$HWCOLOR LOADCOLS 2 18

3 2 890.0 0

0.0 0.0 0.0 1.0 0.0 0.0 0

***BOUNDARY_PRESCRIBED_MOTION_SET**

$HMNAME LOADCOLS 3Rotation

$HWCOLOR LOADCOLS 3 7

2 9 0 1 1.0 0 0.0 0.0

18707

***BOUNDARY_PRESCRIBED_MOTION_SET**

$HMNAME LOADCOLS 4Rotation_Blade2

$HWCOLOR LOADCOLS 4 7

6 9 0 1 1.0 0 0.0 0.0

18707

***INTERFACE_SPRINGBACK_LSDYNA**

$HMNAME LOADCOLS 5Springback

$HWCOLOR LOADCOLS 5 37

$ PSID NSHV

3 10000

***INTERFACE_SPRINGBACK_LSDYNA**

$HMNAME LOADCOLS 6Springback_Blade2

$HWCOLOR LOADCOLS 6 37

$ PSID NSHV

7 10000

***SET_SEGMENT**

$HMNAME CSURFS 1Blade_Slave1

$HWCOLOR CSURFS 1 29

1

503 501 502 504

... ...

10200 10162 10454 10455

***SET_SEGMENT**

$HMNAME CSURFS 2Casing1_Master

$HWCOLOR CSURFS 2 45

2

78913 78878 78877 78912

... ...

79156 79121 79120 79155

***SET_SEGMENT**

$HMNAME CSURFS 3Casing2_Master

$HWCOLOR CSURFS 3 6

3

67153 67118 67117 67152

... ...

67396 67361 67360 67395

***SET_SEGMENT**

$HMNAME CSURFS 4Blade_Slave2

$HWCOLOR CSURFS 4 30

4

81339 81337 81338 81340

91036 90998 91290 91291

***CONTACT_SURFACE_TO_SURFACE_ID**

$HMNAME GROUPS 1ContactBlade1-Casing1

$HWCOLOR GROUPS 1 45

1

1 2 0 0 1 1

0.36 0.31.0000E-04 508.07 20.0 0.00352987

2 4.0

1.0000E-03 0.0

***CONTACT_SURFACE_TO_SURFACE_ID**

$HMNAME GROUPS 2ContactBlade1-Casing2

$HWCOLOR GROUPS 2 6

2

1 3 0 0 1 1

0.36 0.31.0000E-04 508.07 20.0 0.00352987

2 4.0

1.0000E-03

***CONTACT_SURFACE_TO_SURFACE_ID**

$HMNAME GROUPS 3ContactBlade2-Casing2

$HWCOLOR GROUPS 3 6

3

4 3 0 0 1 1

0.36 0.31.0000E-04 508.07 20.0 0.00352987

2 4.0

1.0000E-03

***CONTACT_SURFACE_TO_SURFACE_ID**

$HMNAME GROUPS 4ContactBlade2-Casing1

$HWCOLOR GROUPS 4 8

4

4 2 0 0 1 1

0.36 0.31.0000E-04 508.07 20.0 0.00352987

2 4.0

1.0000E-03

***INITIAL_STRESS_SOLID**

$$ This contains the initial stress states of the blade imported from implicit step file

***SENSOR_DEFINE_NODE**

$HMNAME SENSOR 3Accelerometer

3 18707 10105 Y 0 ACC

***SENSOR_SWITCH**

$HMNAME SENSOR 2SensorSwitch

2 Sensor 3 GT1.0000E-07 1.0

***SENSOR_CONTROL**

$HMNAME SENSOR 1SensorControl

1 CONTACT 1

ON 2

***SET_NODE_LIST**

$HMSET

$HMNAME SETS 1AxisNode

1

18707

***SET_NODE_LIST**

$HMSET

$HMNAME SETS 2BladeNodes

```
      2
*BOUNDARY_SPC_NODE
$HMNAME LOADCOLS      7BladeConstraints
$HWCOLOR LOADCOLS      7      4
18274       0       1       1       1
   ...         ...        ...      ...      ...
94572       0       1       1       1
*DATABASE_HISTORY_SOLID
$HMNAME OUTPUTBLOCKS      1ElemStrainRates
14057    14058    14059    14060    14517    14518    14519    14520
   ...         ...          ...          ...         ...          ...         ...          ...
 107002   107003   107004   107005   107018   107019   107020   107021
*DATABASE_HISTORY_NODE_SET_LOCAL
$HMNAME OUTPUTBLOCKS      3Nodout_Blade1
      8       1       2
*DATABASE_HISTORY_NODE_SET_LOCAL
$HMNAME OUTPUTBLOCKS      4Nodout_Blade2
      9       2       2
*DEFINE_CURVE
$HMNAME CURVES      1LoadCurve
$HWCOLOR CURVES      1      3
$HMCURVE     1    2 LoadCurve
      1       0      1.0      1.0      0.0      0.0       0
           0.0            890.0
          10.0            890.0
```

Appendix D – Simulation of Tip-Rubbing

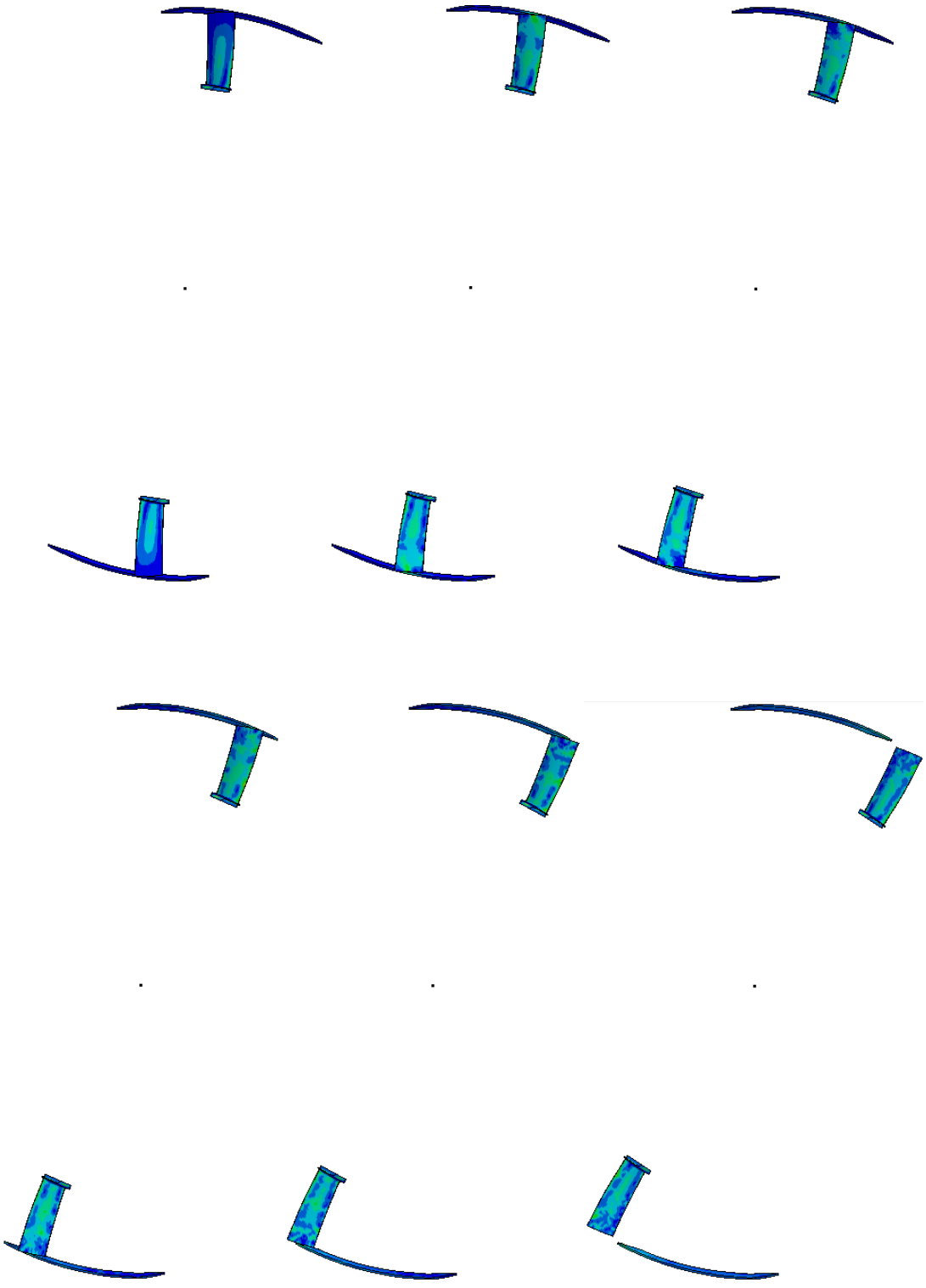

Fig. 0.1 – Tip-rubbing screenshots from t = 0.0035 s till t = 0.0040 s

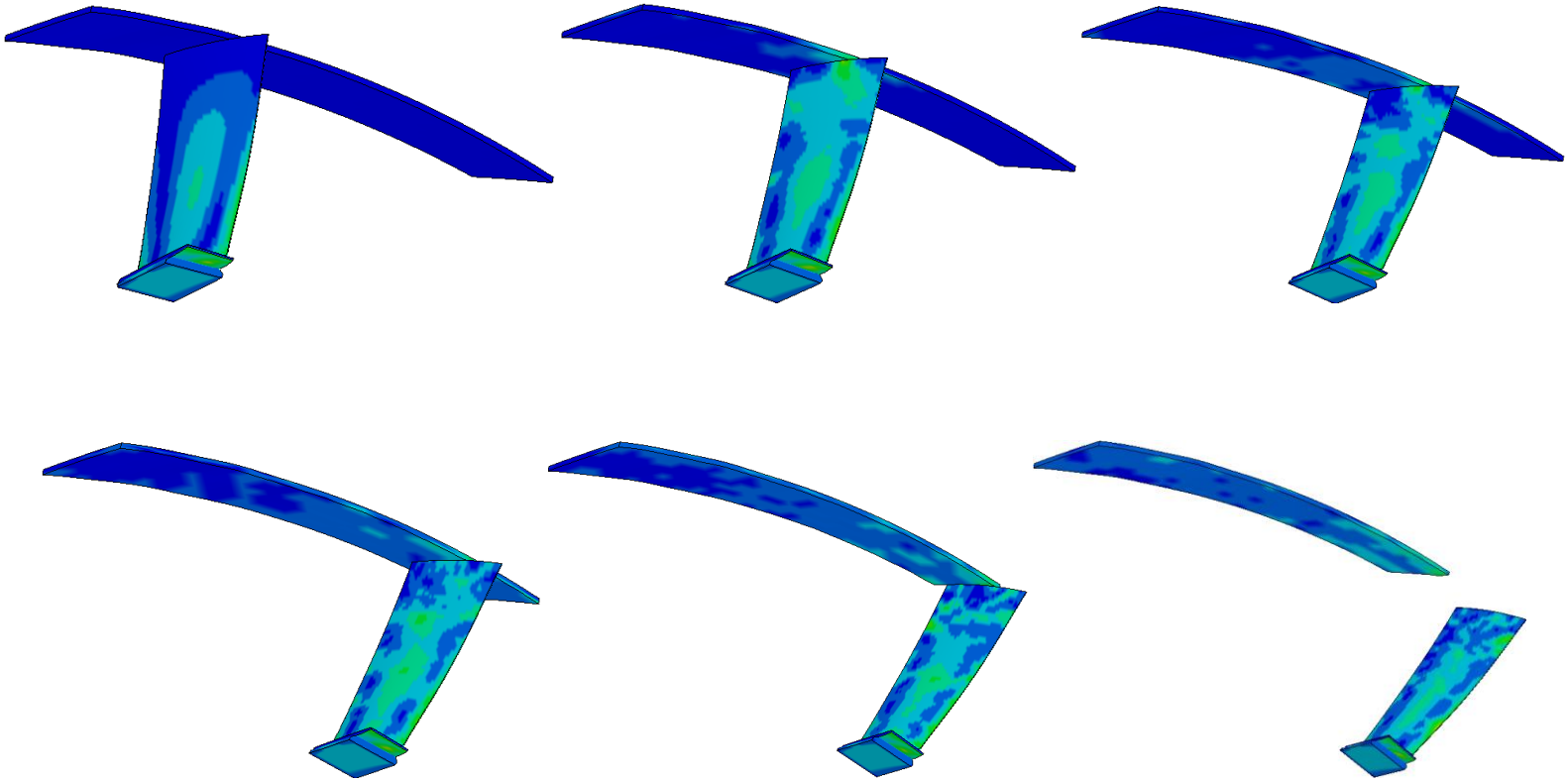

Fig. 0.2 – Interaction of Blade 2 with Casing 1 from t = 0.0035 s till t = 0.0040 s

Appendix E – Frequency Response Curves of Tip-Rubbing Analysis

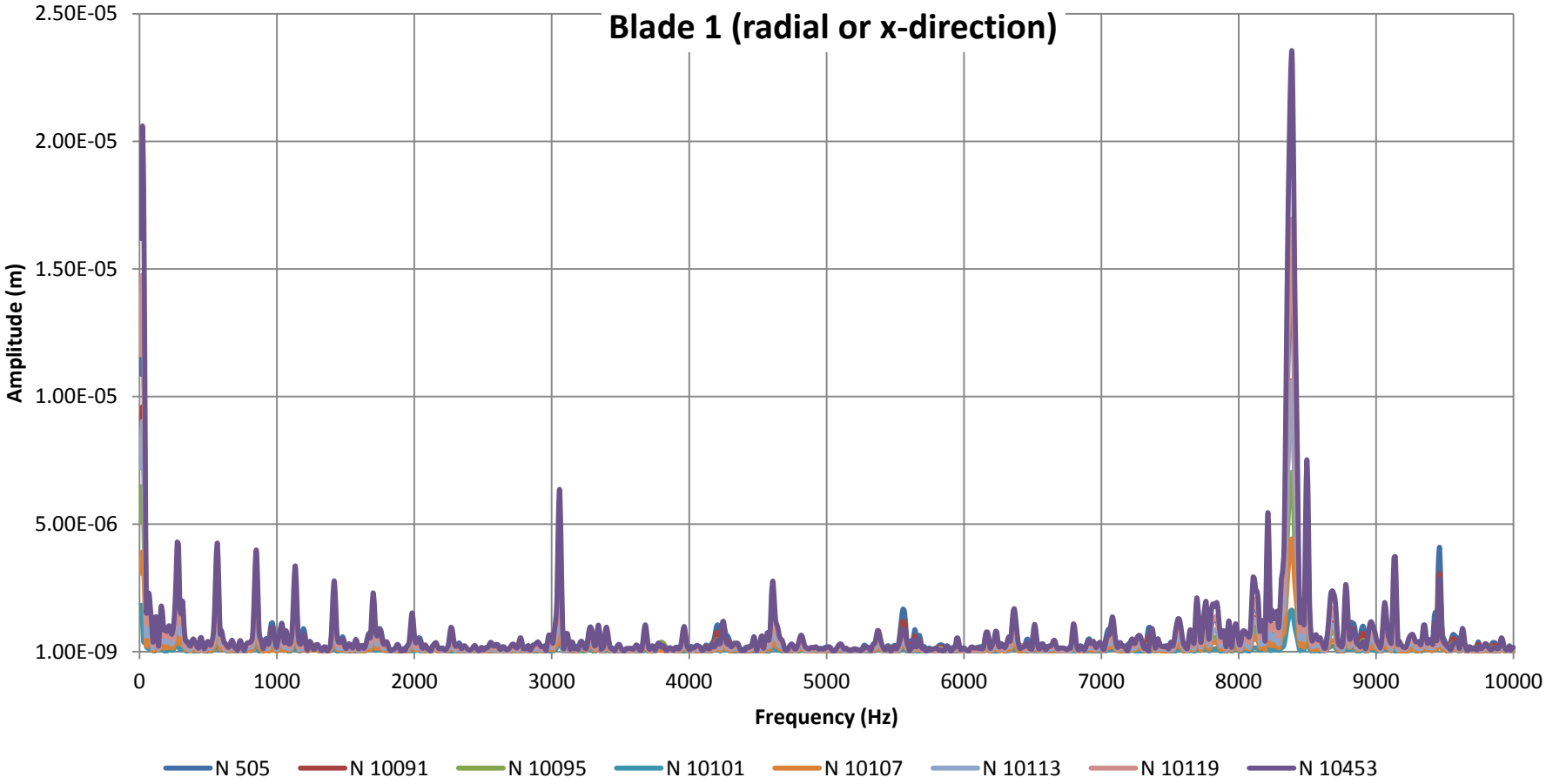

Fig. 0.3 – Frequency response curves in radial direction for Blade 1

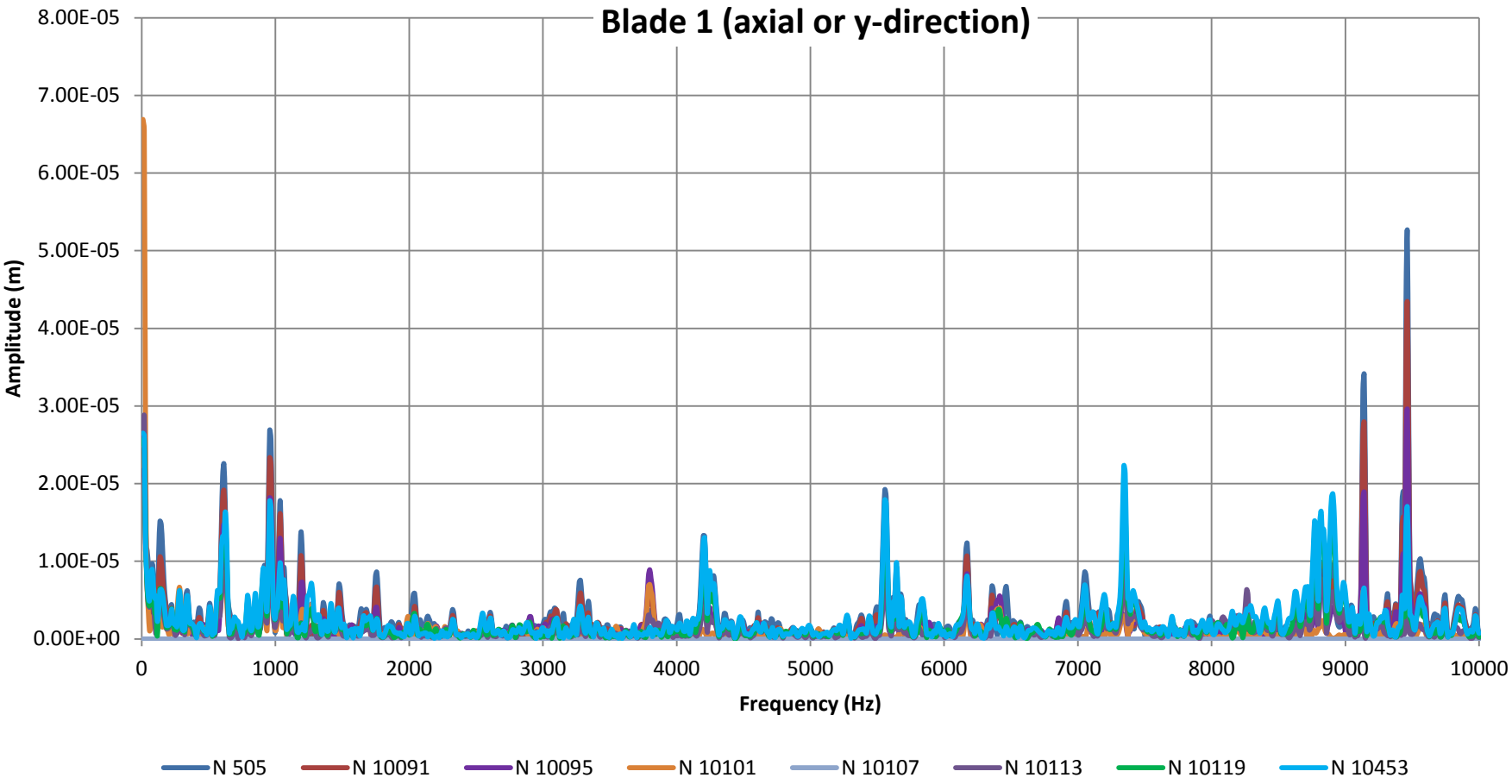

Fig. 0.4 – Frequency response curves in axial direction for Blade 1

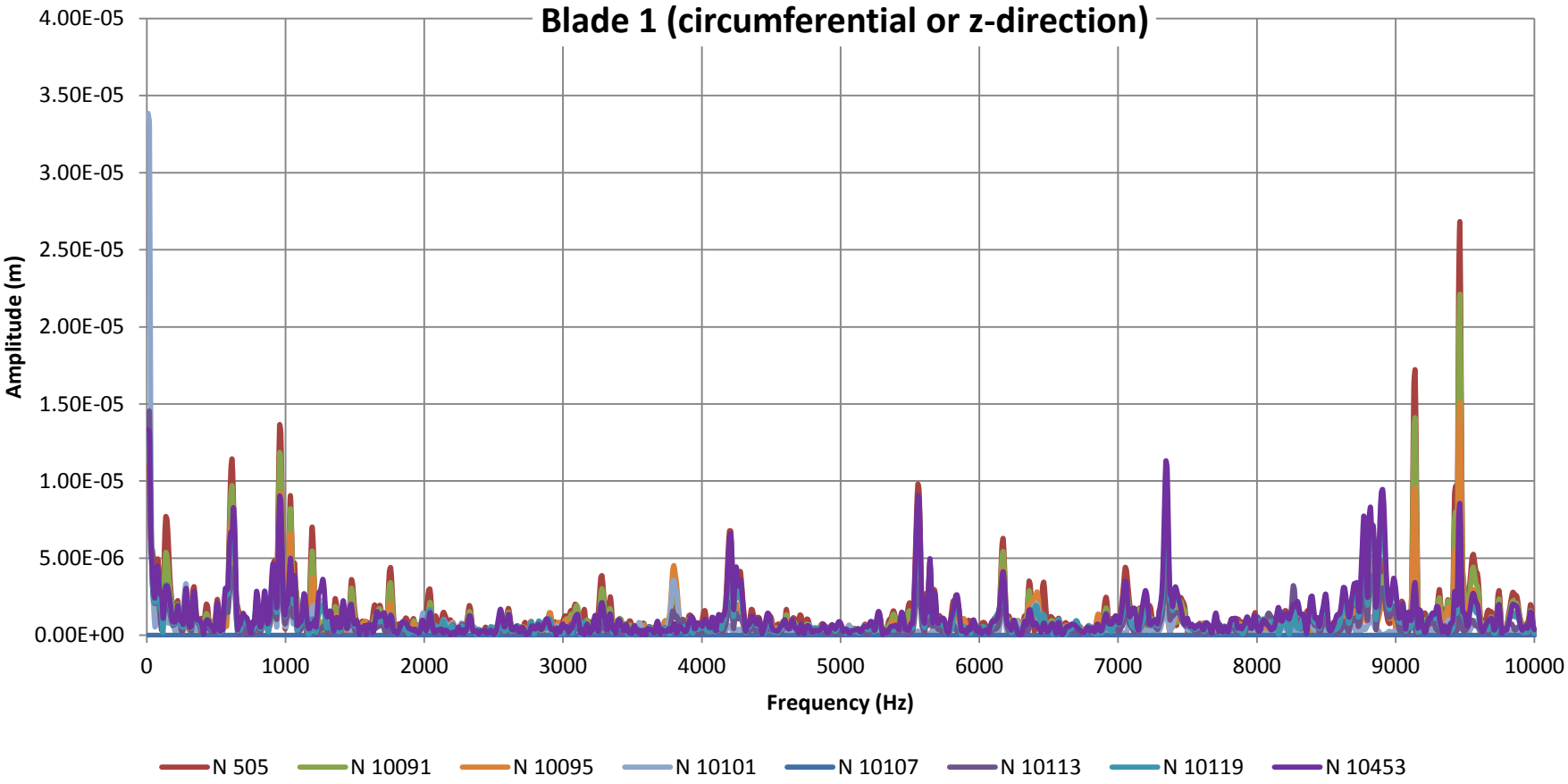

Fig. 0.5 – Frequency response curves in circumferential direction for Blade 1

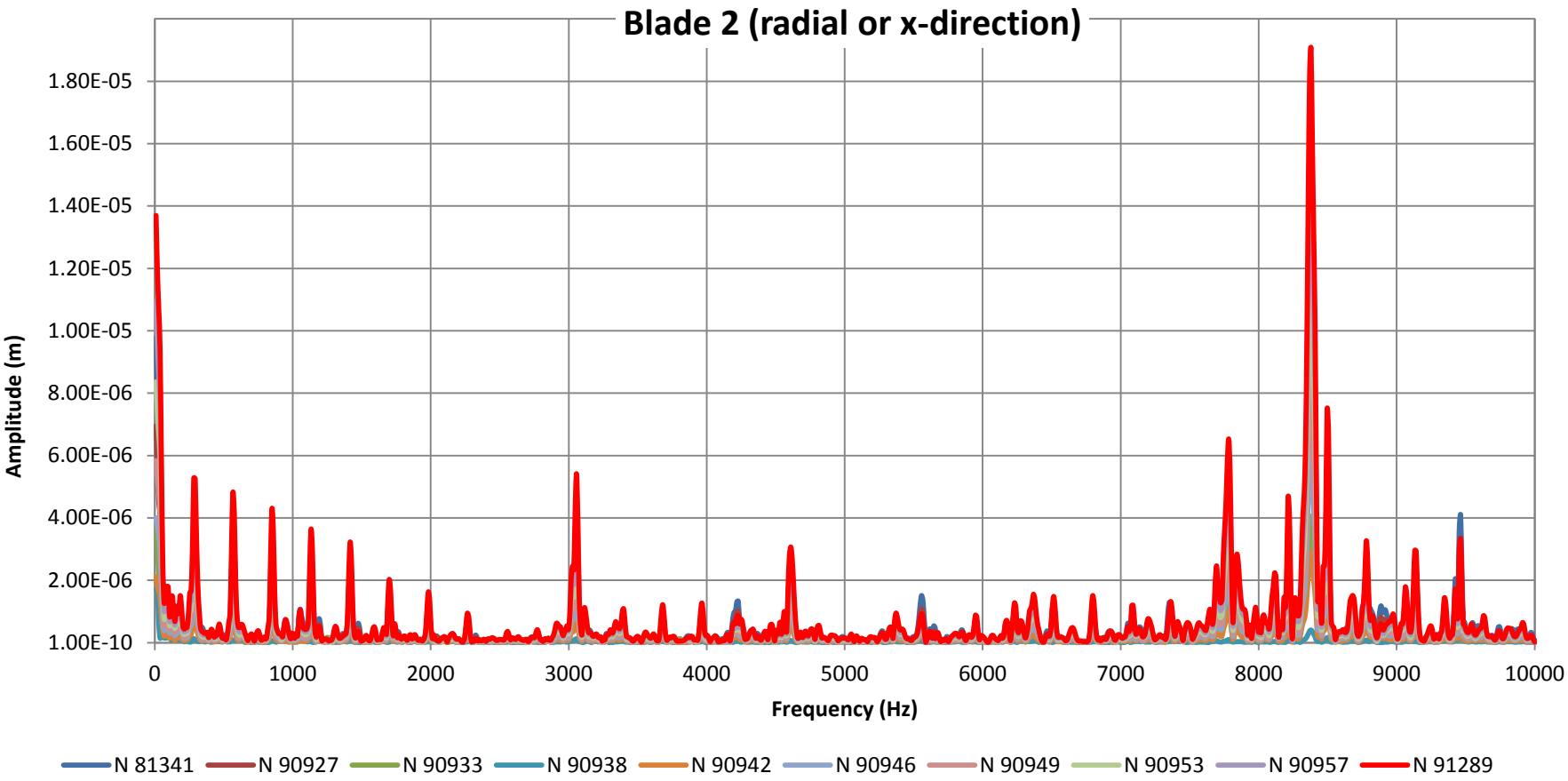

Fig. 0.6 – Frequency response curves in radial direction for Blade 2

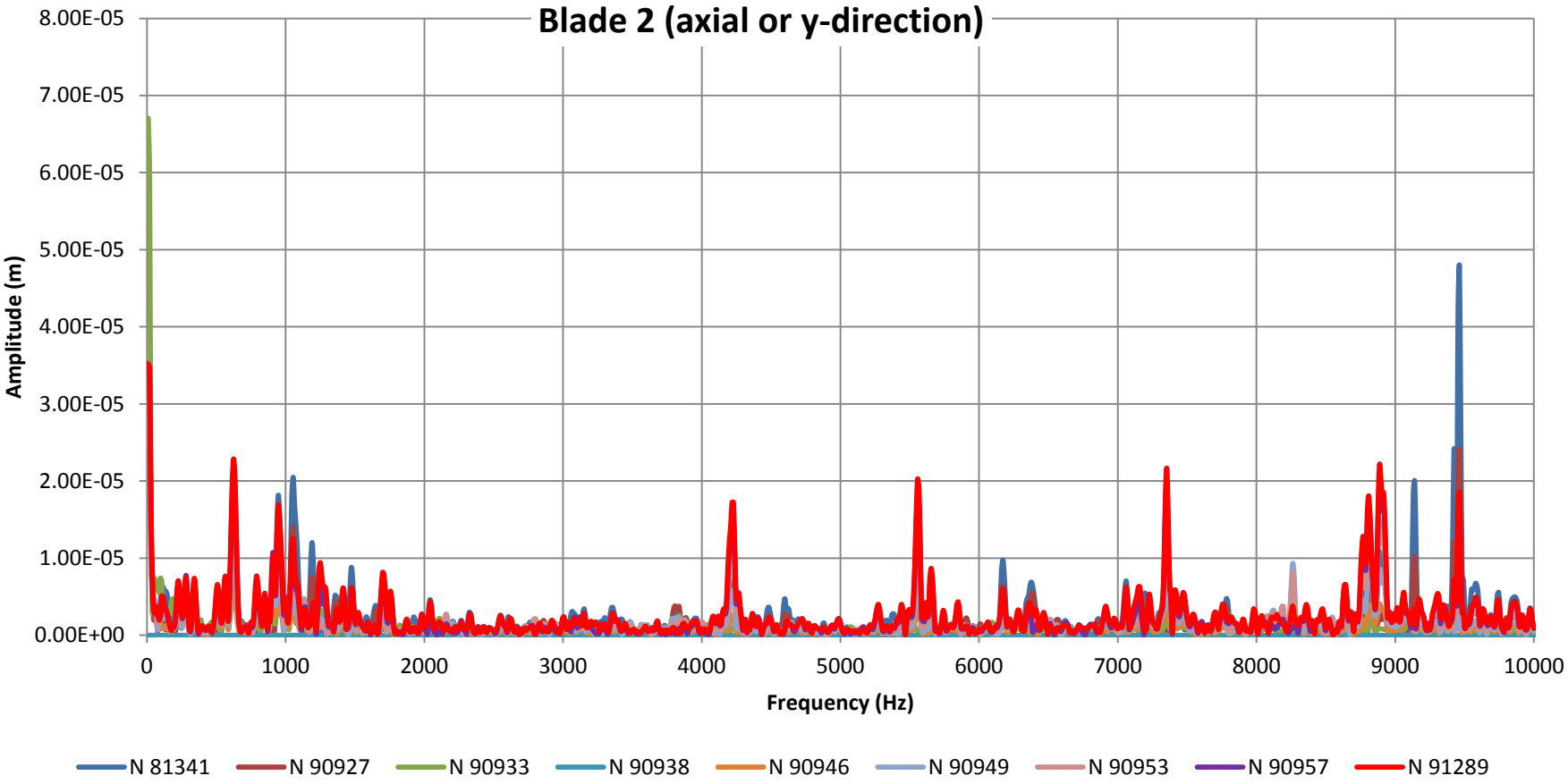

Fig. 0.7 – Frequency response curves in axial direction for Blade 2

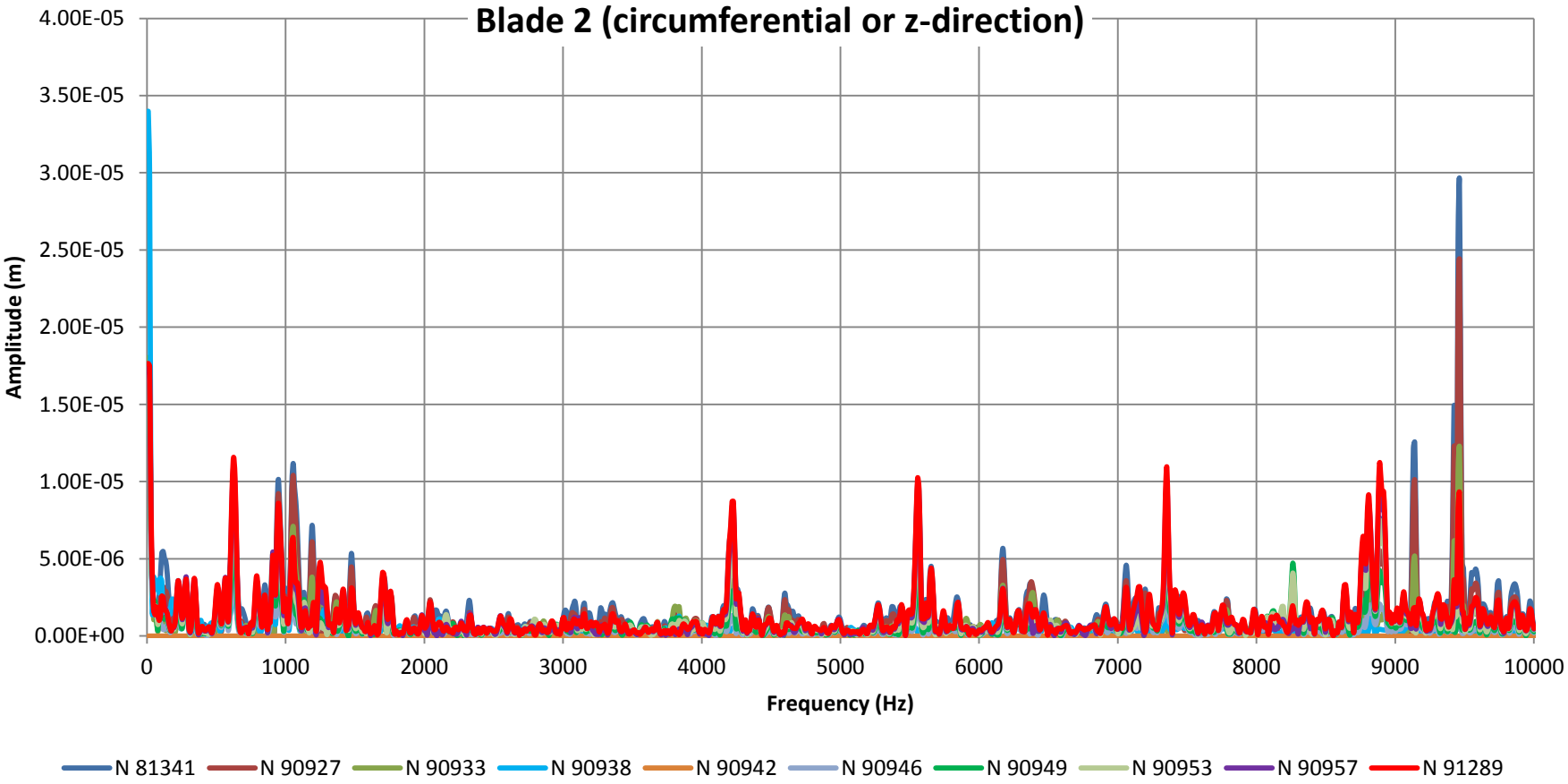

Fig. 0.8 – Frequency response curves in circumferential direction for Blade 2

Appendix F – Engine Orders for IP Compressor

Table 0.1 – Engine orders for IP compressor at engine speeds between 0 and 10000 rpm

	ENGINE ORDERS (Hz)									
ENGINE SPEED (RPM)	1	2	3	4	5	6	7	8	9	10
0	0.00	0.00	0.00	0.00	0.00	0.00	0.00	0.00	0.00	0.00
1000	16.67	33.33	50.00	66.67	83.33	100.00	116.67	133.33	150.00	166.67
2000	33.33	66.67	100.00	133.33	166.67	200.00	233.33	266.67	300.00	333.33
3000	50.00	100.00	150.00	200.00	250.00	300.00	350.00	400.00	450.00	500.00
4000	66.67	133.33	200.00	266.67	333.33	400.00	466.67	533.33	600.00	666.67
5000	83.33	166.67	250.00	333.33	416.67	500.00	583.33	666.67	750.00	833.33
6000	100.00	200.00	300.00	400.00	500.00	600.00	700.00	800.00	900.00	1000.00
7000	116.67	233.33	350.00	466.67	583.33	700.00	816.67	933.33	1050.00	1166.67
8000	133.33	266.67	400.00	533.33	666.67	800.00	933.33	1066.67	1200.00	1333.33
9000	150.00	300.00	450.00	600.00	750.00	900.00	1050.00	1200.00	1350.00	1500.00
10000	166.67	333.33	500.00	666.67	833.33	1000.00	1166.67	1333.33	1500.00	1666.67